2d and 3d Periodic Templates through Holographic Interference Lithography: Photonic and Phononic Crystals and Biomimetic Microlens Arrays

by

Chaitanya K Ullal
Bachelor of Technology
Metallurgical Engineering and Materials Science
Indian Institute of Technology Bombay, 1999

Submitted to the Department of Materials Science and Engineering
in partial fulfillment of the requirements for the degree of

Doctor of Philosophy in Materials Science and Engineering

at the

MASSACHUSETTS INSTITUTE OF TECHNOLOGY

June 2005

Author .....
Department of Materials Science and Engineering
April 29th, 2005

Certified by .....
Edwin Lorimer Thomas
Director, Inst for Soldier Nanotech and Morris Cohen Professor of
Materials Science and Engineering
Thesis Supervisor

Accepted by .....
Gerbrand Ceder
Chair, Department Committee on Graduate Students

2d and 3d Periodic Templates through Holographic Interference Lithography: Photonic and Phononic Crystals and Biomimetic Microlens Arrays

by

Chaitanya K Ullal

Bachelor of Technology

Metallurgical Engineering and Materials Science

Indian Institute of Technology Bombay, 1999

Submitted to the Department of Materials Science and Engineering
on April 29th, 2005, in partial fulfillment of the
requirements for the degree of
Doctor of Philosophy in Materials Science and Engineering

Abstract

In this thesis a simple technique for controlling structure via holographic interference lithography was established and implemented.

Access to various space groups including such important structures as the level set approximations to the Diamond, the Schwartz P structure, the FCC, and the non centrosymmetric Gyroid structures were demonstrated. The ability to make 3D structures over a large area, with low defect densities and periodicities on the subμ scale opens a whole range of opportunities including such diverse areas as photonic crystals, phononic crystals, drug delivery, microtrusses, tissue scaffolds, microfluidics and colloidal crystallization.

A correlation between structure and photonic band gap properties was established by systematically exploring the 11 FCC space groups. This resulted in a technique to search for photonic band gap structures. It was found that a fundamental connectivity caused by simple Fourier elements tended to support gaps. 2-3, 5-6 and 8-9 gaps were opened in the f.c.c lattices. The F-RD and 216 structures were newly shown to have complete band gaps.

Two of the three previously established champion photonic crystal structures, viz. the Diamond and the Gyroid presented practical fabrication challenges, approximations to these structures were proposed. A scalable P structure and the 3-FCC structure were fabricated by single and multiple exposure techniques. Both negative and positive tone photoresist systems were demonstrated. Line defects were written into the negative tone system using two-photon lithography.

The single crystalline, porous nature of the structures was exploited to examine the possibility for their use as hypersonic phononic crystals and microfluidic microlenses. Two dimensional single crystalline patterns were created using interference lithography. Their phononic band structure was probed by Brillioun light scattering to yield a phononic band diagram, which clearly demonstrates the effect of periodicity on the phononic density of states. The ability to control the density of states at these length scales holds the potential for control over thermal properties. The two dimensional structures fabricated in negative photoresist were also tested as microlenses with the integrated pores acting as microfluidic channels. This combination resulted in a structure reminiscent to that of the biological species ophiocoma wendtii.

Thesis Supervisor: Edwin Lorimer Thomas
Title: Director, Inst for Soldier Nanotech and Morris Cohen Professor of Materials Science and Engineering

Acknowledgments

The truth is that this document is incidental. During the course of the time spent that has counted towards my PhD i have learned and changed tremendously. The people included in the incomplete list here were instrumental in those changes. For that i am indebted.

Foremost, i would like to thank Prof Ned Thomas, advisor, par excellence, for just the right combination of freedom, inspiration, exhortation, support and guidance.

I am particularly indebted to Martin Maldovan, colleague and friend, for teaching me almost all that i know about photonic crystals, companionship in the lab at 3:00 AM, and an endless supply of rerun jokes.

I am beholden to a number of people at Bell Labs. Prof. Shu Yang took me under her wing and gave me numerous opportunities and unstinting support. Ronen Rapaport taught me that research is fun. Most of all, Gang Chen showed me by example that knowledge belongs to everyone and that there is joy in every aspect of scientific work, not the least in 'dinky' optics. I am also thankful to Dr Joanna Aizenberg for insights into both science and how to perform it. Drs Yong-Jin Han, Vikram Sundar and Oleg Mitrofanov helped me with underground electron microscopy time when bureaucracy threated to throw a spanner in the works.

It was a delight to work with Taras "Tak" Gorishnyy, whose cheer, honesty and strong fundamentals make him a valuable co-worker. Dr. JiHyun Jang, with her infinite capacity for work and vast reserves of patience, made research life decidedly cushy for me.

Drs. Chris White, Lalgudi Natarajan, Tim Bunning, Peter Mach and Meinhard Wohlgemuth were generous with their knowledge and time. In particular Vincent Tondiglia unselfishly and patiently helped me take my first steps in the land of interference lithography.

I am grateful to Prof G Fytas, and Dr. G Tommasseo with relation to the Brilloiun Light Scattering results, Dr. Tae-woo Lee with the two photon writing, and Dr Renu Tripathi with the initial laser setup.

This thesis would probably have been in a completely different field if Augustine Urbas had not decided that a laser destined for the dumpster deserved a second chance in our lab.

I would like to also to thank self-christened super-UROP Rene Chen for her enthusiasm and willingness to learn.

I got the chance to cut my teeth on a research project first due to the generosity of Dr Manish Deopura, Burak Temelkuran and Prof Yoel Fink

Finally i am grateful to all members of the Thomas lab for their friendship, help and support. In particular, Joseph Walish, who lent me his vast array of skills on the slightest request, and Jean DeAngelis who cheerfully and deftly dealt with all forms of administrative mayhem that i pushed in her direction.

I have not mentioned all the people whose friendship and support have sustained me during my PhD. They have taught me truly invaluable lessons and impacted my life in ways that i will never be able to express. I am secure in this act of ommission. For they know who they are.

Contents

List of Figures

List of Tables

Chapter 1

Introduction

This thesis is the subject of two simple fascinations: structure and light. At the scale of a micron this fascination is frequently accompanied by interest fueled by application. The fabrication of three dimensional structures on this scale is not just a challenge but an opportunity. Any technique utilised for such a purpose is frequently measured against such metrics as its ability to yield structures rapidly and cheaply, while covering large areas and simultaneously affording the controlled introduction of purposeful defects. The bulk of this thesis deals primarily with one such technique viz. holographic interference lithography. In this chapter we briefly outline the potential applications for single crystalline periodic structures with lengthscales on the order of a micron. Various alternate fabrication techniques that can potentially acheive such structures are then described. Since, applicationwise, the primary interest of this thesis is related to the area of 3D photonic crystals, this aspect is emphasized.

1.1 Applications of Porous Single Crystalline Periodic Structures

1.1.1 Photonic Crystals

Photonic crystals can be described as being dielectric composites with periodically varying refractive indices which allow for the control of the interaction of light and

matter. This functionality depends both on the materials parameters as well as the geometry of the system employed. The idea, first proposed by Yablonovitch [1], centers around the concept that full three dimensional spatical periodicity of $\lambda/2$ in the refractive index can result in a range of frequencies in the electromagnetic spectrum near the wavelength λ not being able to propagate, irrespective of direction. This is an extension of the principle behind Fabry-Perot resonators into three dimensions. The use of such photonic crystals holds the promise of numerous application in integrated optical circuits such as the control of the spontaneous emission of light [1], bending of light around sharp corners for waveguides [2], and all on-chip optical transistors [3].

1.1.2 Optimised Composites

It was recently demonstrated that certain, "minimal" three dimensional structures, viz. the bicontinuous simple cubic primitive Schwartz (P), and diamond (D) are optimal for the simultaneous transport of heat and electricity [4]. A minimal surface is one which is locally area minimizing. More specifically, from an application perspective, these are the optimal structures when a weighted sum of the effective thermal and electrical conductivities are maximised for the case in which one component is a good thermal conductor and a poor electrical conductor and the second component is a poor thermal conductor but a good electrical conductor. The demand that this sum is maximised sets up a competition between the two effective transport properties. Importantly the optimality of these composites applies to any pair of the following scalar effective properties: electrical conductivity, thermal conductivity, dielectric constant, magnetic permeability and diffusion coefficient.

1.1.3 Microtrusses

The study of structures which are load sustaining while also being lightweight and compact has lead to the study of truss like structures[5]. In addition to being load bearing, these structures impart functionalities such as cooling due to the presence

of open spaces. The reduction of such structures to the micron scale could result in interesting mechanical properties since at these size scales some materials undergo transformations such as ductile to brittle transitions [6].

1.1.4 Phononic Crystals

Phononic crystals are the acoustic analogue of photonic crystals. In this case, for an appropriate periodic arrangement of elastic moduli gaps can appear in the phononic band structure [7]. Phononic band gaps have their origin in the destructive interference of multiply scattered phonons in periodic structures. As in materials with photonic band gaps, this gives rise to potential applications as novel acoustic devices, such as refractive devices with low relectivity despite high solid content such as lenses and Fabry-Perot interferometers[8], as well as a platform to study the physics governing elastic and acoustic wave propagation in periodic media.[9, 10, 11, 12, 13]

1.1.5 Biomimetic Structures

Single Crystalline Exoskeletons

Naturally occurring bicontinuous structures can be found in the skeletons of sea urchins (frequently termed stereoms) [14]. In any one skeletal element, which may be centimeters in length, the calcite behaves optically as a single crystal. It has been suggested that the single crystalline nature probably owes its origin to the micropatterned framework of the stereom [15, 16]. The exact purposes of these structures are not well established, they were earlier believed to to have evolved to provide excellent nutrient access and to prevent crack propagation through the calcite plates, although this notion has been recently challenged [17].

Tissue scaffolds

The field of tissue engineering exploits living cells in a variety of ways to restore, maintain, or enhance tissues and organs. To engineer living tissues, cultured cells are grown on bioactive degradable scaffolds that provide the physical and chemical

signals to guide their assembly into 3-D tissue. [18] A frequent requirement of these scaffolds is that they be porous and possess a three dimensional construct. In certain cases there is a need for a well characterised, reproducible, in-vitro system or device that can replicate the in-vivo behaviour of the corresponding tissue. For example, in the use of engineered liver tissue in the testing of the disposition and toxicity of drugs [19]. A case could thus be made for the utility of ordered, porous, three-dimensional structures as superior tissue engineering scaffolds.

1.2 Fabrication Techniques

Methods of achieving structures that allow for the fabrication of three dimensional periodic structures on the submicron scale can be broadly classified into "construction-based" assembly and self assembly based techniques. Self assembly relies on the use of thermodynamic forces to spontaneously pattern components into stable structures whereas construction based techniques require the piece by piece placement of the various components of the appropriate structure.

1.2.1 Construction-based Assembled Structures

Layer by Layer Conventional Semiconductor Fabrication

The use of conventional semiconductor fabrication techniques is currently the most advanced technique available in the fabrication of three dimensional structures. Since the method is inherently a two dimensional patterning technique, the desired structure is approximated by a sum of thin slices. The slices are fabricated sequentially to yield the final 3D structure. In order to fabricate subsequent layers it is necessary to ensure alignment between layers and to undertake laborious procedures of planarization via back filling followed by CMP (chemical mechanical polishing) [20] or wafer bonding [21].

Two-Photon Lithography

Two-photon lithography allows for the creation of 3D structures on a sub-micron scale by focusing a pulsed, typically near-infrared, laser beam point by point into a photoactive resin, such that the higher light intensity chemically activates the photoactive resin at those points leading to the formation of solid structures.[22, 23, 24, 25] A schematic of the setup is shown in Figure 1-1(a). The ability to create changes within the volume of the photoresist is possible since it is based on the concept that under sufficient illumination intensity, electronic transitions that would normally require absorption of one high energy photon for excitation can be accomplished by simultaneous absorption of two low energy IR (infra-red) photons, such that their total energy is equivalent to that required for the transition. Femtosecond laser pulses to whose wavelength the photoresist is transparent are tightly focused inside the resin. The pulse intensity is adjusted so that the light power density at the focal spot of the laser beam exceeds the threshold of the two-photon absorption (TPA) and strong absorption takes place. The rate of TPA can be defined as:

$$\text{TPA} = \delta \times \text{I}^2$$

where δ is the TPA cross-section of photoactive molecule (10-50 cm^4s/photon) and I is the photon intensity (photon/cm^2s). The quadratic dependence of two-photon absorption on the incident intensity ensures confinement of the absorption to very small volumes or voxels near the focal region while the incoming and exit beam intensity is insufficient to cause absorption along its path. By high-speed scanning of the focal spot of the laser beam, virtually any predesigned 3D structure can be fabricated even acheiving resolutions which are below the diffraction limit. The best resolution to date is approximately 120nm[23]. A concern with any serial writing technique such as two-photon writing or the direct writing technique discussed in the next subsection is the time taken to write such patterns, a parameter which is, unfortunately, usually not revealed in this regard, since such serial writing processes are inherently very slow.

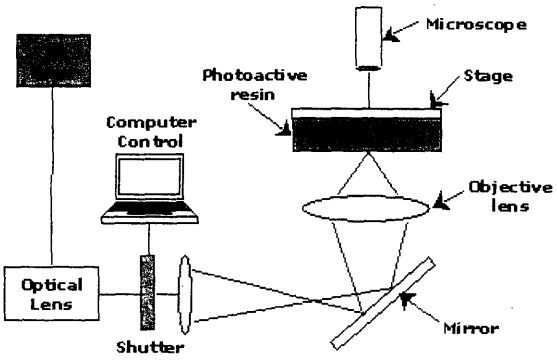

(a) Two-Photon Lithography Setup

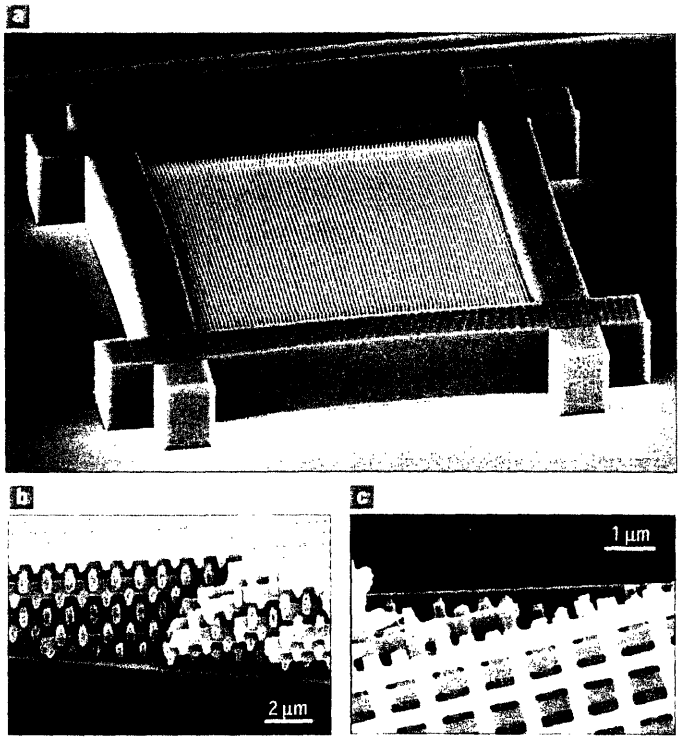

(b) Woodpile structure fabricated via two photon lithography [25]

Figure 1-1: 3D structures throughTwo Photon Lithography

3D Printing and Direct Writing with Polyelectrolytes

Three Dimensional Printing is a solid free form process used in the manufacture of functional prototype parts directly from computer models. It functions by the deposition of polymer powder in layers and the selective binding of the powder by "ink-jet" printing of a binder material. Following the sequential application of layers, the unbound powder is removed resulting in a complex three dimensional part [26]. The resolution achieved in this technique is on the order of 200 μ. An alternative to 3D printing that is based on very similar methodology that is more viable for the length scales in consideration in this thesis is the technique of direct writing [27]. This technique uses fluid inks that are made up of concentrated polyelectrolyte complexes that consist of non-stoichiometric mixtures of polyanions - polyacrylic acid and polycations - polyethylenimine or polyallylamine hydrochloride. By regulating the ratio of anionic to cationic groups and combining these species under solution conditions they are able to get the solutions to have viscosities that are suitable for deposition through nozzles of 05.-5.0μ in diameter. The patterns are written by deposition into an alcohol-water reservoir, in which the polyelectrolyte inks coagulate to form self supporting filaments or rods. The write times for structure with the area shown in Fig.1-2 are typically on the order of 5 minutes.

Micromanipulation and Robotic Assembly

The concept of building a structure through micromanipulation is the most intuitive of the "construction-based" assembly approaches. At the size scale of interest, though, this can be a serious technological challenge and involves the use of either optical tweezers [28], an AFM tip [29] or the use of a micromanipulator [30] to manipulate the requisite building blocks. The ability to integrate the micromanipulator with an imaging system such as an SEM has made this technique the most facile of the three approaches. Here a probe is used to pick up and position objects larger than 100 nm with an accuracy of a few nanometers. This happens because electrostatic and Van derWaals forces dominate the dynamics of micro-objects.

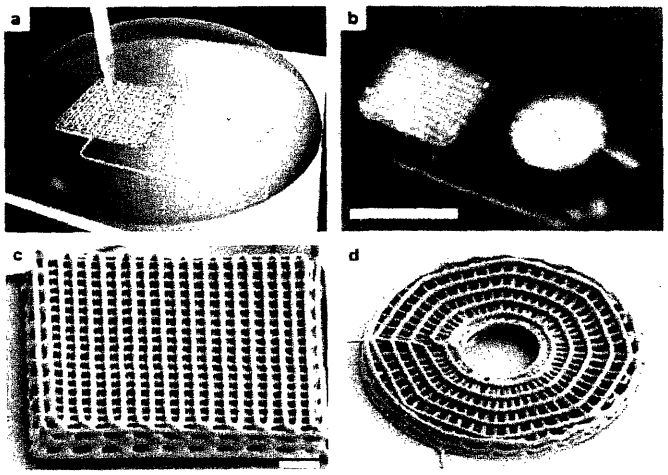

Figure 1-2: Direct writing technique via polyelectrolytes. a) The ink-deposition process (not drawn to scale). A concentrated polyelectrolyte ink is housed in a syringe (yellow) immersed in a coagulation reservoir (grey hemispherical drop) and deposited on to a glass substrate (light grey). b, Optical image acquired in situ during deposition reveals the features drawn in a, including the deposition nozzle that is patterning a three-dimensional lattice, as well as a completed radial array. This image is blurred by the reservoir (scale bar: 100 μm). c, Three-dimensional periodic structure with a face-centred tetragonal geometry (filament diameter: 1 μm; 10 layers; scale bar: 10 μm). d, Three-dimensional radial array (filament diameter: 1 μm; 5 layers; scale bar: 10 μm) [27].

Two approaches have been successfully demonstrated in the attempt to build three-dimensional structures using this technique. In the first, latex and silica microspheres were used as the building blocks to form a self supporting mixed BCC structure [31, 32]. This lattice consisted of two interpenetrating silica and latex sphere diamond lattices respectively. After assembly, the latex lattice was removed by plasma etching to yield a diamond lattice of silica spheres as shown in Fig.1-3. The second approach uses a combination of the layer by layer conventional semiconductor fabrication technique and micromanipulation to build up the three-dimensional structure [33]. First all the layers are fabricated simultaneously, in a large 2D array and micromanipulation is used to cut sections apart and place them one on top of the other. Registration between subsequent layers is ensured by creating circular fiducial holes on each layer and inserting a polystyrene microsphere into the aligned holes of successive layers.

1.2.2 Self Assembly

Block Polymers and Surfactant Based Self Assembly

Block polymer structures are an example of chemically directed self-assembly [34]. The simplest block polymer is a linear A/B diblock consisting of chemically distinct A and B polymer chains covalently linked to form a single molecule. The driving force behind the patterns that are formed by block polymer self assembly lies in the thermodynamic balance resulting from energy minimization. The main competing forces in this minimization are the enthalpy associated with the mutual repulsion of dissimilar blocks and the entropy associated with the number of conformational states available to the polymer chain in a given configuration. Various factors that affect these two forces, such as molecular weight, composition, temperature, A-B interaction parameter etc. determine the nature of the patterns formed. Under certain conditions three dimensional bicontinuous patterns can be formed. [35].

At the length scales of concern, however the use of block polymers is not so straightforward. This is related to the fact that in order to realize structures with

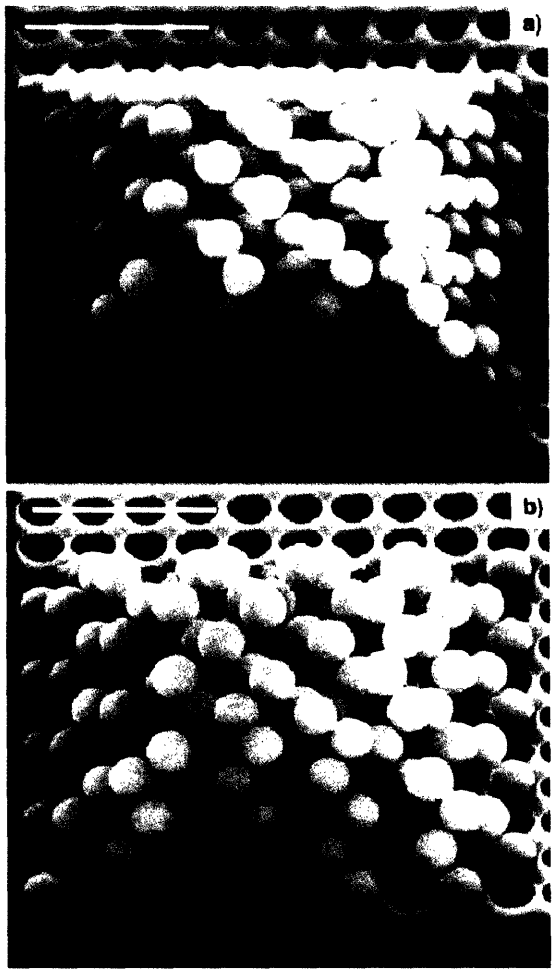

Figure 1-3: Six-layer diamond structure grown in the {001} direction. a) mixed BCC structure made of 165 latex and 177 silica spheres. b) the same sample after plasma etching resulting in a diamond lattice. Sphere diameter is 1.18μm. The pitch of the silicon template is 1.35μm. Hole depths are 450 nm and 1.08μm, respectively. Layer-to-layer distance is 680 nm. Scale bars are 5.0μm [32]

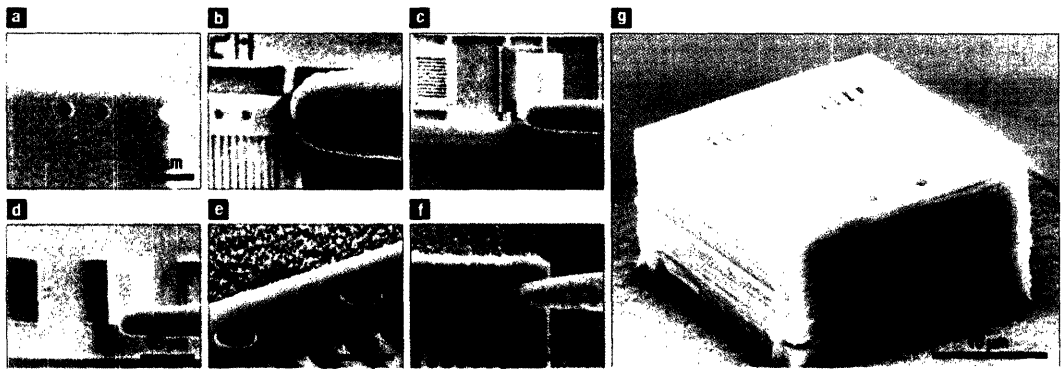

Figure 1-4: Assembly of 3D structures through micromanipulation. a) Two microspheres are inserted into pore openings of a substructure. b) A bridge of a plate is broken by pushing it with a probe tip. c) A photonic plate separated from a substrate is picked up with a probe. d) The separated plate is transferred to the substructure in a. e) The tops of microspheres inserted into the substructure guide the photonic plate into alignment by catching the holes of the plate. f) The 2D photonic plate is fixed on the substructure by inserting a microsphere into residual pore opening and two more microspheres are inserted into holes of the plate for stacking of the next layer. Pressure was applied to the plate with the probe to promote self-bonding of plates. g) Side view of a 20-layer woodpile structure. The periods of rods, rod width and layer thickness are 1.4 μm, 0.37 μm and 0.5 μm, respectively. The size of the structure is 25 x 25 x 10 μm^3 and that of patterned region is 15 x 15 x 10 μm^3 [33]

appropriate length scales, the size (molecular weight) of the blocks must increase and the associated kinetics involved with pattern formation get more difficult to overcome, resulting in the formation of grains and various types of uncontrolled defects, if structures are formed from cooling above the order disorder temperature. A variety of biases, including mechanical flow fields, electric fields, temperature gradients and surface interactions have been utilized to create large area single crystalline patterns on smaller length scales. Successful attempts at larger length scales have been limited [36].

Chemically directed self assembly can also be acheived through surfactant based self-assembly of binary systems, such as surfactant-water, or surfactant-oil, or ternary systems comprised of surfactant, oil and water. Block polymers can be thought of as large amphiphiles. Thus, surfactant based self assembly is very similar in nature, inasmuch that the basis of the formation of the patterns is thermodynamic energy minimization with similar competing forces. Self assembling surfactant systems usually involve two or more dissimilar phases which are partitioned into a periodic morphology by surfactant interfaces. As in the case of block copolymers, under certain conditions three dimensional bicontinuous structures can be formed [37]. The range of volume fractions occupied by a given structure for both surfactants and block polymers is limited. Further, this technique faces the usual problems that plague self assembly such as the presence of defects and grain formation. In addition ab-initio design of desirable structures is hard and the set of structures available is limited.

Colloidal Crystallisation

Colloids are small particles, in the range of nanometers to microns, that are suspended in a liquid or a gas. These particles can be made to self assemble, owing to their electrostatic or other interactions and give rise to crystalline structures. Owing to the easy availability of monodisperse silica and polymer colloids in the appropriate size range, a large number of workers have created colloidal photonic crystals[38]. The most common structure for monodispersed spheres is the close packed face centered cubic structure. This tends to limit both the volume fraction and the symmetries

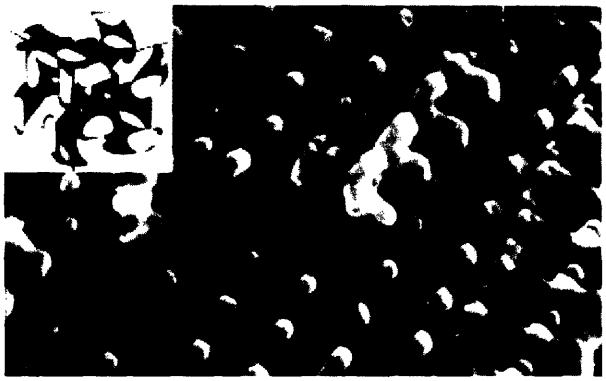

Figure 1-5: SEM image of the UV-etched styrene/isoprense block copolymer with double gyroid structure. UV exposure along with ozonolysis removes the isoprene component leaving behind the two polystyrene networks. The inset is the level set approximation to the double gyroid structure with $\phi = 0.34$ [36].

accessible via this technique, although a number of work-arounds have been suggested, such as the use of binary colloids [39], use of non spherical particles etc. [40]. The primary challenge while dealing with colloidal crystals is in the creation of large size samples with low defect densities (Fig.1-6). A variety of guiding fields have been applied in this endeavour including sedimentation via gravity [41], electric fields [42], grapho-epitaxy [43] and capillary forces [44] to name a few.

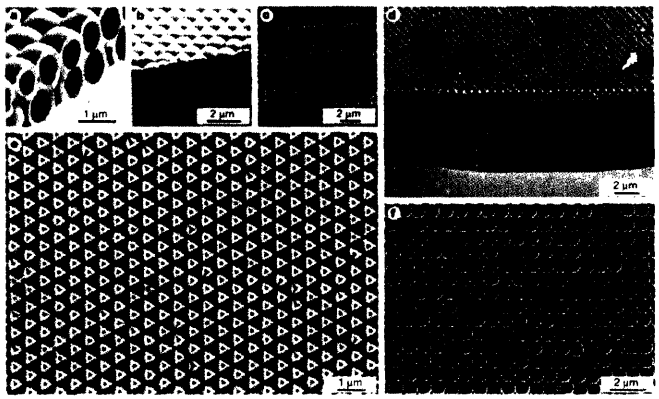

Figure 1-6: SEM image of FCC close packed silica colloidal particles [44]

1.3 Holographic Interference Lithography: Background

Holographic interference lithography is a technique that allows one to create 1D, 2D and 3D patterns very simply using coherent beams of light. Light is an electromagnetic wave and it is the inherent periodicity present in the light that we exploit while creating structures using holographic lithography. Essentially holographic lithography involves the formation of a time independent spatial variation of intensity created by the interference of two or more beams of light. These periodic variations of intensity can then be transferred into a light sensitive medium to yield structures.

The idea of using light to create 1D gratings and 2D patterns as a sequence of exposures had been around for some time. The first suggestion that a 2D pattern could be made in a single exposure came from Cowan and Slafer [45]. The idea of using light to create 3D patterns comes from the field of condensed matter physics and laser cooling [46]. Standing waves are created by multiple beams of light resulting in a periodic field. A process called laser cooling causes atoms moving through such optical lattices to lose enough energy so that they become trapped at the points of minima of the periodic field. The interest in this area is to do with the dynamics of these trapped atoms and to examine such issues as Bose-Einstein condensates. To date the main areas of interest from the perspective of 3D patterns created by holographic interference lithography has been in the areas of laser cooling via optical lattices [46], photonic crystals [47] and holographic-polymer dispersed liquid crystals [48].

The first suggestion that holographic interference lithography could be used to create 3D photonic crystals came from Mei *et* al.[49]. They were able to show optical images of slices of some larger spacing 3D structures created by visible light. Berger *et* al.took the idea of using 3D patterns formed by holographic lithography for photonic crystals a step further. They observed that while an FCC pattern could be simply created, a diamond pattern would be accessible through a multiple exposure routine. Their technique relied on phase shifts to ensure the requisite registered translation

of the pattern since a diamond lattice is a sum of two FCC lattices shifted in space from one another by $1/4^{th}$ of the body diagonal of the unit cell. They demonstrated via a 2D hexagonal lattice case the multiple exposure routine based on phase shifts.

Turberfield and co-workers were the first to actually demonstrate the transfer of a 3D holographic interference pattern into a photoresist with an eye towards its photonic band gap properties [47]. The structure that they created was one with an FCC translational periodicity with a motif that was reminiscent of an interconnected diamond network. The polarisations that they used were presumably designed to maximise contrast in the resist and thus, although the photonic band gap properties had been emphasised, it resulted in a structure whose inverse[1] has a maximum gap of only ~2%, even at a dielectric contrast of 13:1. Nevertheless, this work served to create a great deal of interest in this area. It was the first convincing experimental demonstration that large area photonic crystals with low defect densities could be fabricated rapidly. Further the photoresist system employed by Turberfield, SU8, has become the standard for transferring interference patterns into polymer. Independently, and almost simultaneously Shoji and Kawata [50] demonstrated a 3D structure transfered into a photoresist. This structure however is not bicontinuous, making its use as a template dubious. Further, although its photonic crystal properties were touted, calculations by Maldovan have shown that it does not possess a band gap.

Subsequent work of note has tended to be engineering in nature based on the 'diamond-like' structure proposed in [47]. Yang *et* al.[51] demonstrated a modified SU8 photoresist platform that could be employed at visible wavelengths, and included a contrast enhancer, in the form of a base. Miklyaev *et* al.[52] noted the need for a prism in order to access the correct angles within the high index photoresist. They however did not index match the prism resulting in shifts in polarisation. Divliansky *et* al.[53] suggested the use of a set of gratings in order to split the beams and generate the requisite angles, thereby simplifying the optical setup. Their setup however does not consider control of polarisations.

[1]The inverse structure is defined as one in which the regions of high and low dieletrics are switched.

Although example beam directions giving rise to the 14 translational periodicities have been listed [54], prior to this work limited attention has been paid to the control of structures that are available through the technique of interference lithography. Bunning and co-workers [48, 55] have applied the concepts of 3D structures via holographic interference lithography to their holographic-polymer dispersed liquid crystal (h-PDLC) sytems. They wrote a variety of patterns including an orthorhombic P structure [48] and some Orthorhombic F structures [55] in their acrylate based liquid crystal system. Escuti *et* al.wrote an FCC pattern into a similar h-PDLC system [56]. From a structure perspective, an interesting area is that of quasicrystals. Quasicrystals via interference lithography was demonstrated by Burns *et* al.[57]. The effort in this area, though, have been mainly based on 2D structures [58, 59].

1.4 Objective

It is amply evident from this summary of construction and self-assembly based approaches to 3D structures, holographic interference lithography is a versatile and promising technique. Clearly, given the strong impact that a technique for fabricating three dimensional structures on the submicron scale can potentially have, there is an opportunity and a need to understand the control over the range of structures available via holographic interference lithography. The objective of this thesis is thus both scientific as well as engineering in nature. We seek to understand and exploit the opportunities that the technique of holographic lithography affords in the fabrication of structures. In order to do this we first establish an understanding of the structures that can be created using the interference of light with just a few beams. Having identified the general set of structures that are accessible using this technique we then identify what structural parameters are of interest from the perspective of photonic band gap properties. Some of the structures are then experimentally realised. Finally we examine some of these structures as templates for phononic band gap structures and μlenses.

Chapter 2

Correlating Structural Symmetries and Beam Parameters in Holographic Lithography

In this chapter we examine the technique of interference lithography. We then study the structures that are accessible using this technique [1]

2.1 The Intensity Equation

Light is an electromagnetic wave and it is this inherent periodicity that we exploit while creating structures using holographic lithography. Holographic lithography involves the formation of a spatial variation of intensity created by the inteference of two or more beams of coherent light. In order to understand the patterns that are formed it is thus instructive to look at the intensity equation. The electric field associated with a planar monochromatic beam of light can be described mathematically as

$$\overrightarrow{\mathbf{E}}_m(\overrightarrow{\mathbf{r}},t) = \overrightarrow{\mathbf{E}}_{o,m} e^{i(\overrightarrow{\mathbf{k}}_m \cdot \overrightarrow{\mathbf{r}} - \omega t + \phi_m)} \tag{2.1}$$

[1] The primary results of this chapter have been published by Ullal et al. [60]

where m is simply the index identifying the particular beam, $\vec{\mathbf{E}}_o$ is the polarisation, $\vec{\mathbf{k}}$ is the wave vector, ω is the angular frequency, and ϕ is the phase of the beam. If we have more than one coherent electromagnetic wave present, then the net electric field is simply the vector sum of the electric fields. The intensity variation created by these electric fields is proportional to the square of the magnitude of the resultant vector sum. Since the polarisation associated with an electromagnetic wave need not be linear, but can be circularly or elliptically polarised as well, the intensity is arrived at by the inner product of the electric field with its complex conjugate. From this equation we see that the interference pattern has only a spatial variation and no temporal variation.

$$\begin{aligned} I(\vec{\mathbf{r}}) &= (\vec{\mathbf{E}}_1 + \vec{\mathbf{E}}_2 + \vec{\mathbf{E}}_3 + \ldots) \cdot (\vec{\mathbf{E}}_1^* + \vec{\mathbf{E}}_2^* + \vec{\mathbf{E}}_3^* + \ldots) \\ &= (\ldots + \vec{\mathbf{E}}_{o,l} e^{i(\vec{\mathbf{k}}_l \cdot \vec{\mathbf{r}} - \omega t + \phi_l)} + \ldots) \cdot (\ldots + \vec{\mathbf{E}}_{o,m}^* e^{i(-\vec{\mathbf{k}}_m \cdot \vec{\mathbf{r}} + \omega t - \phi_m)} + \ldots) \\ &= (\ldots + \vec{\mathbf{E}}_{o,l} e^{i(\vec{\mathbf{k}}_l \cdot \vec{\mathbf{r}} + \phi_l)} + \ldots) \cdot (\ldots + \vec{\mathbf{E}}_{o,m}^* e^{i(-\vec{\mathbf{k}}_m \cdot \vec{\mathbf{r}} + \omega t - \phi_m)} + \ldots) \\ &= \sum_{m=1}^{n} \sum_{l=1}^{n} \vec{\mathbf{E}}_l \cdot \vec{\mathbf{E}}_m^* e^{(i(\vec{\mathbf{k}}_l - \vec{\mathbf{k}}_m) \cdot \vec{\mathbf{r}}) + \phi_l - \phi_m} \end{aligned} \tag{2.2}$$

For n=2, with linear polarisation the intensity equation reduces to a one dimensionally periodic pattern given by

$$I(\vec{\mathbf{r}}) = \vec{\mathbf{E}}_{o,0}^2 + \vec{\mathbf{E}}_{o,1}^2 + 2\vec{\mathbf{E}}_{o,0} \cdot \vec{\mathbf{E}}_{o,1} cos(\Delta \vec{\mathbf{k}} \cdot \vec{\mathbf{r}} + \phi_0 - \phi_1) \tag{2.3}$$

This is the equation for a grating with spatial period of $|\Delta \vec{\mathbf{k}}| = |\vec{\mathbf{k}}_0 - \vec{\mathbf{k}}_1|$. The use of three and four beams results in two dimensionally and three dimensionally periodic structures respectively. The addition of a fifth interfering beam would create a pattern with a translational periodicity in four dimensions. The resultant pattern that would be observed would thus be a three dimensional cut through four dimensional space, just as a particular plane is a two dimensional cut through three dimensional space. The magnitude of the relative phase amplitudes fixes the position of the origin. Thus for four beams, a change in phase causes a translation of the intensity pattern. In the

case of five beams the shift is in four dimensional space and the three dimensional cut that we observe will be completely changed as a result of this shift. This complication with phases makes it difficult to work with more than four beams. We thus primarily focus on the patterns formed by the interference of four coherent beams of light.

2.2 The Fourier analogy and achieving the translational periodicities of the Bravais Lattices

It is useful to view the intensity patterns created in holographic lithography as the sum of gratings. This is true because any structure can be expressed as a sum of Fourier terms. Each Fourier term would thus correspond to a grating arising from the interference of two beams and if one had the ability to easily and reproducibly control phase we would be able to make any arbitrary pattern that we wanted through multiple exposures. This phase problem of registration is not easily overcome and we are once again restricted to using four beams since the registration between the gratings in this case is guaranteed.

The interference of four beams of light with arbitrary directions, amplitudes and phases results in a maximum of thirteen terms (eqn. 2.2), of which there are six terms along distinct directions (some terms only differ from each other by $\pi/2$ in phase).The set of thirteen terms clearly places a restriction on the sort of structures one can form through a four beam approach. In order to get an understanding of the patterns created by these six gratings we go back to the analogy between the Fourier series of a periodic structure and the intensity equation. The Fourier series approximation to the function I($\vec{\mathbf{r}}$) is given for n terms by

$$I(\vec{\mathbf{r}}) = \sum_{m=1}^{n}\sum_{l=1}^{n} a_{lm} e^{i\vec{\mathbf{G}}_{lm}\cdot\vec{\mathbf{r}}} \tag{2.4}$$

If we compare eqns (2.2) and (2.4) we can see that the intensity equation has its translational periodicity determined by the difference between the wave vectors ($\vec{\mathbf{k}}_l - \vec{\mathbf{k}}_m$) of the interfering beams while the polarizations, represented by a set of

complex electric field vectors $\epsilon_l = \{\epsilon^l_{x,re} + i\epsilon^l_{x,im}, \epsilon^l_{y,re} + i\epsilon^l_{y,im}, \epsilon^l_{z,re} + i\epsilon^l_{z,im}\}$, determine the pattern or motif placed within the unit cell. The combination of the motif and the translational periodicity determines the full set of symmetries associated with, and hence the space group, of the resultant structure.

We first turn our attention to the translational periodicity associated with these structures. As with all translationally periodic structures the minimum set of vectors that we need to consider is the set of basis vectors, since the remaining vectors can be achieved by a linear combinations of this set. In two dimensions there are five lattice nets, while in three dimensions there are fourteen Bravais lattices. Thus in order to get a desired translational periodicity it is necessary to equate the difference between the wave vectors with basis vectors associated with that translational periodicity. One way to do this is to set the first wave vector, $\overrightarrow{\mathbf{k}}_0$ to the reciprocal lattice vector that is equidistant from the origin and the basis vectors $\{\overrightarrow{\mathbf{b}}_m\}$. The remaining wave vectors are then given simply given by $\overrightarrow{\mathbf{k}}_m = \overrightarrow{\mathbf{b}}_m + \overrightarrow{\mathbf{k}}_0$. Since there are an infinite number of choices of basis vectors for a particular type of translational symmetry, we can vary the size of the unit cell simply by changing the angle between the beams. Obviously the control of the lattice size is discrete and not continuous. A list of wave vectors for the translational periodicities associated with the fourteen Bravais lattices can be found in ref. [54]

2.3 Space Groups and Polarisations

It is important to remember that the construction of a Bravais lattice through the choice of a set of four noncoplanar $\overrightarrow{\mathbf{k}}$ vectors is only a necessary condition to get the translational symmetry of the Bravais lattice expressed in the holographic structure. When the polarisations are taken into account, the material pattern that emerges out of the interference of the beams will give rise to some overall symmetry that may or may not respect all the various site symmetries of the particular Bravais lattice. Indeed, it may not even correspond to any of the space groups of the originally specified Bravais lattice. Moreover, if, say, we chose to consider cubic lattices and we

choose beam parameters such that we always obey the site symmetries of the three cubic Bravais lattices, then we would have managed to get only three of the possible 36 space groups. Clearly to correctly establish the symmetries of the structures formed. one must pay attention to the resultant space groups. An excellent introduction to the theory of symmetries and space groups can be found in the text by Buerger [61]

To guarantee a particular space group, we thus need to make a suitable choice of not just the $\overrightarrow{\mathbf{k}}$ vectors but also the polarisation vectors. Although previous work has recognised the influence of the polarisation interactions on the resultant structure, no systematic investigation of the influence of the choice of polarisations on the structural symmetry has been developed [62, 46] One further restriction that we place on the beam parameters is that they all have the same wavelength. Choosing a particular value for the wavelength has the effect, in most but not all cases, of fixing the sizescale of the pattern that is formed. This is true, since, if we change the angle between the beams we may not be able to get all the elements that we want since all of the trigonometric terms that we need may no longer be available. Clearly all the patterns are still scalable from the point of view of the laser wavelength. Finally and importantly, from the perspective of targeting practical three dimensional structures an important property is that of bicontinuity. We define a structure as being bicontinuous if it consists of two distinct regions or phases each of which is self-supporting and completely connected within itself.

2.4 Achieving Space Groups via the Elimination of Terms

To ensure a particular space group, the minimum number of conditions that we need to impose is the number of generators for that space group as listed in the International Tables of Crystallography [63]. A first approach is thus to use the appropriate beam directions to achieve the required translational symmetries commensurate with the chosen space group. We then satisfy the remaining symmetries of the space group by

eliminating undesired terms and equating coefficients of others as required. This is done by adjusting the amplitudes and phases of the polarisation vectors so as to obtain zeroes in the coefficients of the undesired terms (or net zero sums of several unwanted terms) and the desired values in the remaining terms of the intensity equation.

A specific example is illustrative: consider a two dimensional pattern, which belongs to the plane group $p2mm$. The generators for this plane group are the translations [10], and [01], a two fold axis at the origin, and a mirror at x,0. We first choose three beams that yield a rectangular lattice net (e.g., $\vec{\mathbf{k}}_0 = [-\pi/a \ \ -\pi/b \ \ -\pi/c]$, $\vec{\mathbf{k}}_1 = [\pi/a \ \ -\pi/b \ \ -\pi/c]$, $\vec{\mathbf{k}}_2 = [-\pi/a \ \ \pi/b \ \ -\pi/c]$). We then ensure the two fold axis by using linearly polarised light, since structures without a center of inversion are achieved by use of elliptically polarized light.

The resultant intensity equation is given by

$$\begin{aligned} I(\vec{\mathbf{r}}) = & \vec{\mathbf{E}}_0 \cdot \vec{\mathbf{E}}_0 + \vec{\mathbf{E}}_1 \cdot \vec{\mathbf{E}}_1 + \vec{\mathbf{E}}_2 \cdot \vec{\mathbf{E}}_2 + 2\vec{\mathbf{E}}_0 \cdot \vec{\mathbf{E}}_1 \cos(2\pi x/a) \\ & + 2\vec{\mathbf{E}}_0 \cdot \vec{\mathbf{E}}_2 \cos(2\pi y/a) + 2\vec{\mathbf{E}}_1 \cdot \vec{\mathbf{E}}_1 \cos(2\pi(x-y)/a) \end{aligned} \tag{2.5}$$

The mirror is now introduced by enforcing the condition $I(x,y) = I(x,-y)$. The imposed condition results in the relation $\vec{\mathbf{E}}_1 \cdot \vec{\mathbf{E}}_2 = 0$. Care must be taken at this stage to ensure that no additional undesired symmetries have been introduced. For example in the case of the creating a two-dimensional structure with plane group pm by use of three beams and a single exposure. one always introduces a two fold axis along with the mirror. The resultant structure has $p2mm$ symmetry rather than the desired pm.

We could thus attempt to access a desired space group by choosing polarisation vectors that would leave us with an equation that possessed only symmetries compatible with the generators. However this can be an onerous task given the number of generators that each group can possess. This approach has been attempted by two other groups subsequent to our examination of the subject via the level set approach [64, 65].

2.5 Achieving Space Groups through Level Set Equations

A simpler, more efficient and sytematic alternative to guaranteeing that the interference structure has the desired space group is to adopt a level set approach [66]. The level-set technique can be utilized to rapidly find suitable candidate functions that are invariant under the space group symmetry operations. This technique is used to describe interface surfaces in microphase separated morphologies such as those typically found in block copolymer systems. The level surfaces are functions that are of the form F: $\mathbf{R}^3 \rightarrow \mathbf{R}$ of points $\{x, y, z\} \epsilon \mathbf{R}^3$ that satisfy the equation $F(x, y, z) = t$, where t is a constant. As specific detailed examples in this chapter we deal only with functions that are also triply periodic, bicontinuous with cubic symmetry. The level set equation is then compared with the intensity equation. The final step involves solving for an appropriate set of polarisations from the set of nonlinear simultaneous equations that are obtained by equating the coefficients of the linearly independent terms. The constant term present in the final intensity equation does not affect the symmetry of the structure but does have strong practical significance. In fact it affects the volume fraction of the final pattern and it can also affect the contrast of the pattern in the photoresist.

The level-set technique uses the structure factor of the chosen space group to generate the functions that possess the requisite symmetries. The structure factor describes the amplitudes and phases of the three-dimensional diffraction pattern that are due to the scattering of incident radiation off of planes (hkl) of atoms in the crystalline structure. Care must be taken, however since for special values for h,k and l, the particular factor $\mathbf{F}_{(hkl)}$ can have extra symmetries belonging to that of a supergroup. The simplicity of the level set approach can be seen by returning once again to the plane group *p2mm*.

The plane group *p2mm* has four Wyckoff sites: x, y; $\bar{x}, \bar{y}$; $\bar{x}, y$; $x, \bar{y}$. We introduce these into the structure factor and take the first terms of the allowed reflections given

by $F_{(10)}+F_{(01)}$. We obtain the equation:

$$F_{(10)} + F_{(01)} = \cos x + \cos y \tag{2.6}$$

which is the same as what we arrived at in the previous approach. Thus the structure factor already has the desired *p2mm* symmetry, and we are saved the trouble of building the equation. Next, we simply compare the structure factor equation with the intensity equation to give us the beam parameters that we desire. The constraint for the *p2mm* structure is as before, $\vec{\mathbf{E}}_1 \cdot \vec{\mathbf{E}}_2 = 0$ with the beam directions as listed in section 2.4. We now examine the level-set approach in detail and the approximations to four important triply periodic bicontinuous cubic structures.

2.5.1 Level Surface of $Pm\bar{3}m$ (No. 221): Approximation to the Schwarz P surface

Following the derivation of the level set equation given in Wohlgemuth et al [66] for space group $Pm\bar{3}m$ we see that the first nonzero $F_{(hkl)}$ *(h=1, k=0, l=1)* is given by

$$F_{(100)} = \cos 2\pi x + \cos 2\pi y + \cos 2\pi z \tag{2.7}$$

We first choose the beam directions and phase angles to give us the trigonometric terms that we desire. In this case the $\vec{\mathbf{k}}$ vectors need to satisfy the conditions

$$\begin{aligned} \vec{\mathbf{k}}_1 - \vec{\mathbf{k}}_0 &= 2\pi/a[100] \\ \vec{\mathbf{k}}_2 - \vec{\mathbf{k}}_0 &= 2\pi/a[010] \\ \vec{\mathbf{k}}_3 - \vec{\mathbf{k}}_0 &= 2\pi/a[001] \\ |\vec{\mathbf{k}}_i| &= 2\pi/\lambda \end{aligned} \tag{2.8}$$

A set of vectors that satisfy this condition is given by

$$\begin{aligned}
\vec{\mathbf{k}}_0 &= \pi/a[\bar{1}\bar{1}\bar{1}] \\
\vec{\mathbf{k}}_1 &= \pi/a[1\bar{1}\bar{1}] \\
\vec{\mathbf{k}}_2 &= \pi/a[\bar{1}1\bar{1}] \\
\vec{\mathbf{k}}_3 &= \pi/a[\bar{1}\bar{1}1]
\end{aligned} \tag{2.9}$$

Since $Pm\bar{3}m$ is a centrosymmetric group, we choose the polarisations to be linear[2]. In this case since a difference in phases causes only a translation in the pattern, we set $\phi_i = 0$. The intensity equation now becomes

$$\begin{aligned}
I(\vec{\mathbf{r}}) =& \vec{\mathbf{E}}_0 \cdot \vec{\mathbf{E}}_0 + \vec{\mathbf{E}}_1 \cdot \vec{\mathbf{E}}_1 + \vec{\mathbf{E}}_2 \cdot \vec{\mathbf{E}}_2 + \vec{\mathbf{E}}_3 \cdot \vec{\mathbf{E}}_3 \\
&+ 2\vec{\mathbf{E}}_0 \cdot \vec{\mathbf{E}}_1 \cos 2\pi x/a \\
&+ 2\vec{\mathbf{E}}_0 \cdot \vec{\mathbf{E}}_2 \cos 2\pi x/a \\
&+ 2\vec{\mathbf{E}}_0 \cdot \vec{\mathbf{E}}_3 \cos 2\pi x/a \\
&+ 2\vec{\mathbf{E}}_1 \cdot \vec{\mathbf{E}}_2 \cos 2\pi (x-y)/a \\
&+ 2\vec{\mathbf{E}}_1 \cdot \vec{\mathbf{E}}_3 \cos 2\pi (x-z)/a \\
&+ 2\vec{\mathbf{E}}_2 \cdot \vec{\mathbf{E}}_3 \cos 2\pi (y-z)/a
\end{aligned} \tag{2.10}$$

Now we compare coefficients with the terms in the equation $F_{(100)}$ and solve for the required polarisation magnitudes and directions. One solution to the resultant constraints is given by

$$\begin{aligned}
\vec{\mathbf{E}}_0 =& 1.000[0.0, 0.707, -0.707] \\
\vec{\mathbf{E}}_1 =& 0.632[-0.5, 0.309, -0.809] \\
\vec{\mathbf{E}}_2 =& 0.874[0.809, 0.5, -0.309] \\
\vec{\mathbf{E}}_3 =& 2.288[-0.309, 0.809, 0.5]
\end{aligned} \tag{2.11}$$

[2]This is an arbitrary choice since in this case we could allow elliptically polarised solutions as well. For noncentrosymmetric structures it is necessary that the light not be linearly polarised.

This gives us an intensity equation of

$$I(\vec{\mathbf{r}}) = 7.4 + \cos 2\pi x/a + \cos 2\pi y/a + \cos 2\pi z/a \tag{2.12}$$

which has the same symmetry as $F_{(100)}$, namely $Pm\bar{3}m$. The plot for the 50:50 volume fraction of this isointensity surface is shown in figure 2-1

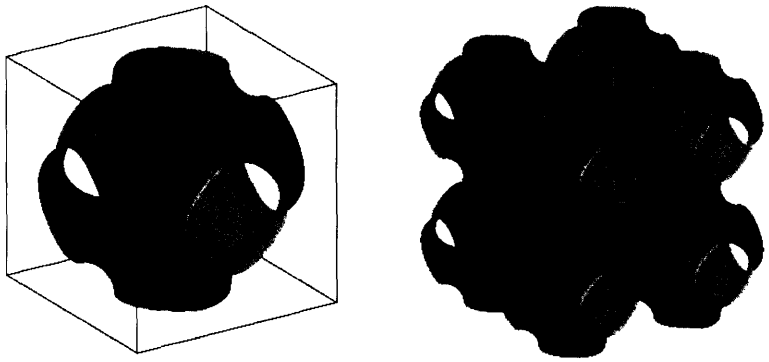

(a) Single Unit Cell (b) Multiple Unit Cells

Figure 2-1: Plot of the approximation to the P surface showing one and eight unit cells. The level set corresponds to space group $Pm\bar{3}m$ (No. 221) and provides a filling fraction of f=0.5

2.5.2 Level Surface of $Fd\bar{3}m$ (No. 227): Approximation to the D surface

Schwarz's D surface is a triply periodic minimal surface with the symmetries of space group $Fd\bar{3}m$ (No. 277). The level-set equation for the lowest order nonzero term for this space group is

$$\begin{aligned} F_{(111)} = &\cos 2\pi x \cos 2\pi y \cos 2\pi z + \sin 2\pi x \sin 2\pi y \cos 2\pi z \\ &+ \sin 2\pi x \cos 2\pi y \sin 2\pi z + \cos 2\pi x \sin 2\pi y \sin 2\pi z \end{aligned} \tag{2.13}$$

Using identities, we recast this equation in a form that allows us to readily compare it with the terms of the intensity equation:

$$\begin{aligned} F_{(111)} = &\sin 2\pi(x+y+z) + \sin 2\pi(x+y-z) \\ &+ \sin 2\pi(x-y+z) + \sin 2\pi(-x+y+z) \end{aligned} \tag{2.14}$$

where we have shifted the origin by $(\pi/2, \pi/2, \pi/2)$ and dropped the factor of 0.5. Once again we choose the $\overrightarrow{\mathbf{k}}$ vectors and phase angles to give us the trigonometric terms we desire. A choice of $\overrightarrow{\mathbf{k}}$ vectors and phase angles that satisfy the given conditions is

$$\begin{aligned} \overrightarrow{\mathbf{k}}_0 &= \pi/a[201]; & \phi_0 &= \pi/2 \\ \overrightarrow{\mathbf{k}}_1 &= \pi/a[\bar{2}01]; & \phi_1 &= \pi/2 \\ \overrightarrow{\mathbf{k}}_2 &= \pi/a[02\bar{1}]; & \phi_2 &= 0 \\ \overrightarrow{\mathbf{k}}_3 &= \pi/a[0\bar{2}\bar{1}]; & \phi_3 &= 0 \end{aligned} \tag{2.15}$$

As noted previously, the choice of phase angles in the case of four or fewer beams causes only an origin shift, leaving the symmetries unaffected. As in subsection 2.5.1 we obtain a set of constraints by comparing the coefficients of the linearly independent terms of the resultant intensity equation. One solution to this set of constraints is given is

$$\begin{aligned} \overrightarrow{\mathbf{E}}_0 &= 2.163[0.116, -0.966, -0.231] \\ \overrightarrow{\mathbf{E}}_1 &= 0.566[0.442, -0.158, 0.883] \\ \overrightarrow{\mathbf{E}}_2 &= 1.225[0.890, 0.204, 0.408] \\ \overrightarrow{\mathbf{E}}_3 &= 1.274[0.294, 0.427, -0.855] \end{aligned} \tag{2.16}$$

The resultant intensity equation is

$$I(\vec{\mathbf{r}}) = 8.125 + \sin 2\pi/a(x+y+z) + \sin 2\pi/a(-x+y+z) + \sin 2\pi/a(x-y+z) + \sin 2\pi/a(x+y-z) \quad (2.17)$$

By varying the value of the constant term, we can access a family of surfaces with different volume fractions as shown in Fig.2-2 . In an experimental setup, this would correspond to varying the time of exposure, intensity of light or the chemistry of the photoresist.

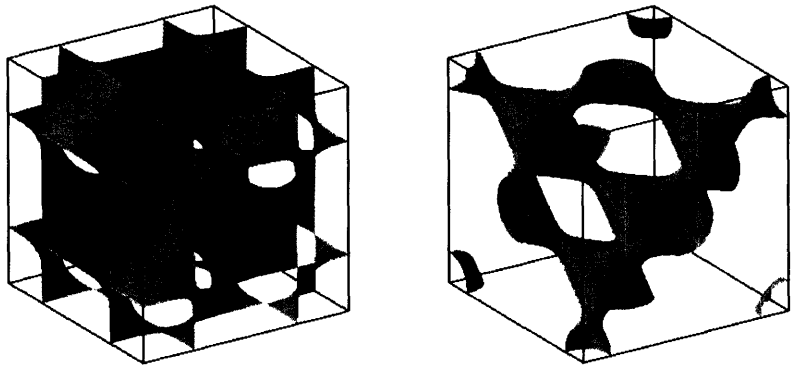

(a) f=0.5, t=0

(b) f=0.125, t=-1.8

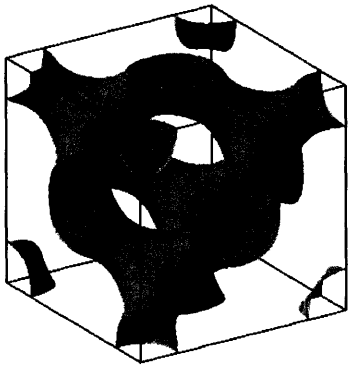

(c) f=0.252, t=-1.2

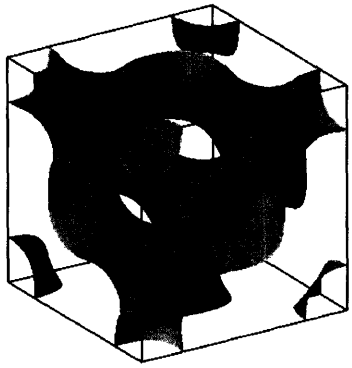

(d) f=0.664, t=-0.8

Figure 2-2: Plots of the level set approximation to the D surface for a range of filling fractions. The volume fraction can be changed by simply varying the constant term t in the level set equation, in this case equation 2.14. It is important to note that in figure d the surfaces are reversed from parts a, b and c, such that the components in the network and in the matrix are reversed.

2.5.3 Level Surface of $I4_132$ (No. 214): Approximation to the Noncentrosymmetric Gyroid surface

The lowest-order $F_{(hkl)}$ term for the space group $I4_132$, to which the chiral gyroid belongs, is the $\{110\}$ and is given by

$$\begin{aligned} F_{(110)} = &\sin 2\pi(x+y) + \sin 2\pi(x-y) \\ &+ \sin 2\pi(y+z) + \sin 2\pi(y-z) \\ &+ \sin 2\pi(x+z) + \sin 2\pi(z-x) \end{aligned} \tag{2.18}$$

The choice of $\vec{\mathbf{k}}$ vectors that yields the desired trigonometric arguments is given by

$$\begin{aligned} \vec{\mathbf{k}}_0 &= \pi/a[\bar{1}\bar{1}\bar{1}] \quad \vec{\mathbf{k}}_1 = \pi/a[11\bar{1}] \\ \vec{\mathbf{k}}_2 &= \pi/a[1\bar{1}1] \quad \vec{\mathbf{k}}_3 = \pi/a[\bar{1}11] \end{aligned} \tag{2.19}$$

The requirement for chirality stipulates the need for elliptically polarised light as represented by complex polarisations. Given this added level of difficulty, we look at the solution in more detail[3]. For ease of comparison between the intensity equation and the structure factor equation we rewrite equation 2.2 more explicitly as

$$\begin{aligned} I(\vec{\mathbf{r}}) = &\vec{\mathbf{E}}_0 \cdot \vec{\mathbf{E}}_0^* + \vec{\mathbf{E}}_1 \cdot \vec{\mathbf{E}}_1^* + \vec{\mathbf{E}}_2 \cdot \vec{\mathbf{E}}_2^* + \vec{\mathbf{E}}_3 \cdot \vec{\mathbf{E}}_3^* \\ &+ 2Re(\vec{\mathbf{E}}_0 \cdot \vec{\mathbf{E}}_1^* \cos((\vec{\mathbf{k}}_0 - \vec{\mathbf{k}}_1) \cdot \vec{\mathbf{r}})) - 2Im(\vec{\mathbf{E}}_0 \cdot \vec{\mathbf{E}}_1^* \sin((\vec{\mathbf{k}}_0 - \vec{\mathbf{k}}_1) \cdot \vec{\mathbf{r}})) \\ &+ 2Re(\vec{\mathbf{E}}_0 \cdot \vec{\mathbf{E}}_2^* \cos((\vec{\mathbf{k}}_0 - \vec{\mathbf{k}}_2) \cdot \vec{\mathbf{r}})) - 2Im(\vec{\mathbf{E}}_0 \cdot \vec{\mathbf{E}}_2^* \sin((\vec{\mathbf{k}}_0 - \vec{\mathbf{k}}_2) \cdot \vec{\mathbf{r}})) \\ &+ 2Re(\vec{\mathbf{E}}_0 \cdot \vec{\mathbf{E}}_3^* \cos((\vec{\mathbf{k}}_0 - \vec{\mathbf{k}}_3) \cdot \vec{\mathbf{r}})) - 2Im(\vec{\mathbf{E}}_0 \cdot \vec{\mathbf{E}}_3^* \sin((\vec{\mathbf{k}}_0 - \vec{\mathbf{k}}_3) \cdot \vec{\mathbf{r}})) \\ &+ 2Re(\vec{\mathbf{E}}_1 \cdot \vec{\mathbf{E}}_2^* \cos((\vec{\mathbf{k}}_1 - \vec{\mathbf{k}}_2) \cdot \vec{\mathbf{r}})) - 2Im(\vec{\mathbf{E}}_1 \cdot \vec{\mathbf{E}}_2^* \sin((\vec{\mathbf{k}}_0 - \vec{\mathbf{k}}_2) \cdot \vec{\mathbf{r}})) \\ &+ 2Re(\vec{\mathbf{E}}_1 \cdot \vec{\mathbf{E}}_3^* \cos((\vec{\mathbf{k}}_1 - \vec{\mathbf{k}}_3) \cdot \vec{\mathbf{r}})) - 2Im(\vec{\mathbf{E}}_1 \cdot \vec{\mathbf{E}}_3^* \sin((\vec{\mathbf{k}}_0 - \vec{\mathbf{k}}_3) \cdot \vec{\mathbf{r}})) \\ &+ 2Re(\vec{\mathbf{E}}_2 \cdot \vec{\mathbf{E}}_3^* \cos((\vec{\mathbf{k}}_2 - \vec{\mathbf{k}}_3) \cdot \vec{\mathbf{r}})) - 2Im(\vec{\mathbf{E}}_2 \cdot \vec{\mathbf{E}}_3^* \sin((\vec{\mathbf{k}}_0 - \vec{\mathbf{k}}_3) \cdot \vec{\mathbf{r}})) \end{aligned} \tag{2.20}$$

[3]The solution to this set of nonlinear equations was determined by Martin Maldovan.

The set of constraints can now clearly be written as

$$
\begin{aligned}
Re(\vec{\mathbf{E}}_0 \cdot \vec{\mathbf{E}}_1^*) = 0 \quad & Im(\vec{\mathbf{E}}_0 \cdot \vec{\mathbf{E}}_1^*) = c \\
Re(\vec{\mathbf{E}}_0 \cdot \vec{\mathbf{E}}_2^*) = 0 \quad & Im(\vec{\mathbf{E}}_0 \cdot \vec{\mathbf{E}}_2^*) = c \\
Re(\vec{\mathbf{E}}_0 \cdot \vec{\mathbf{E}}_3^*) = 0 \quad & Im(\vec{\mathbf{E}}_0 \cdot \vec{\mathbf{E}}_3^*) = c \\
Re(\vec{\mathbf{E}}_1 \cdot \vec{\mathbf{E}}_2^*) = 0 \quad & Im(\vec{\mathbf{E}}_1 \cdot \vec{\mathbf{E}}_2^*) = c \\
Re(\vec{\mathbf{E}}_1 \cdot \vec{\mathbf{E}}_3^*) = 0 \quad & Im(\vec{\mathbf{E}}_1 \cdot \vec{\mathbf{E}}_3^*) = c \\
Re(\vec{\mathbf{E}}_2 \cdot \vec{\mathbf{E}}_3^*) = 0 \quad & Im(\vec{\mathbf{E}}_2 \cdot \vec{\mathbf{E}}_3^*) = c \\
\vec{\mathbf{E}}_0 \cdot \vec{\mathbf{E}}_0^* = a_0 \quad \vec{\mathbf{E}}_1 \cdot \vec{\mathbf{E}}_1^* = a_1 \quad & \vec{\mathbf{E}}_2 \cdot \vec{\mathbf{E}}_2^* = a_2 \quad \vec{\mathbf{E}}_3 \cdot \vec{\mathbf{E}}_3^* = a_3 \\
\vec{\mathbf{k}}_0 \cdot \vec{\mathbf{E}}_0 = 0 \quad \vec{\mathbf{k}}_1 \cdot \vec{\mathbf{E}}_1 = 0 \quad & \vec{\mathbf{k}}_2 \cdot \vec{\mathbf{E}}_2 = 0 \quad \vec{\mathbf{k}}_3 \cdot \vec{\mathbf{E}}_3 = 0
\end{aligned}
\tag{2.21}
$$

This set of nonlinear constraints must now be solved. Since an overall phase does not affect the final intensity distribution, we can further simplify this by assigning the value of the imaginary z component of $\vec{\mathbf{E}}_3$ to be zero. At this point we have 23 unknowns. To have 23 equations, we release the constraint on the modulus of $\vec{\mathbf{E}}_3$. The ease of solution strongly depends on the the choice of c and the initial value guess for the variables. The values of $a_0 - a_3$ and c are not independent. A possible solution to this set of nonlinear constraints is given by the complex polarisation vectors:

$$
\begin{aligned}
\vec{\mathbf{E}}_0 &= \{-0.153 - i0.342, 0.520 - i0.470, -0.367 + i0.813\} \\
\vec{\mathbf{E}}_1 &= \{-0.520 - i0.725, 0.373 + i0.039, -0.147 - i0.686\} \\
\vec{\mathbf{E}}_2 &= \{0.667 + i0.215, 0.888 - i0.088, 0.220 - i0.303\} \\
\vec{\mathbf{E}}_3 &= \{-0.209 + i0.362, 0.209 + i0.362, 0.418\}
\end{aligned}
\tag{2.22}
$$

The resultant intensity equation, which has the same symmetries as the space group $I4_132$ is the approximation to the gyroid and is plotted in Fig. 2-3. The equation is

given by

$$I(\vec{\mathbf{r}}) = 4.811 - \sin(2\pi/a(y-x)) - \sin(2\pi/a(x+y)) - \sin(2\pi/a(x-z)) - \sin(2\pi/a(z-y)) - \sin(2\pi/a(x+z)) - \sin(2\pi/a(y+z)) \quad (2.23)$$

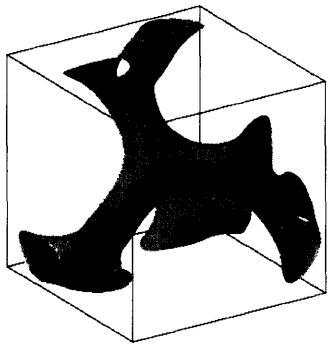

Figure 2-3: Plot of the level set approximation to the G surface, with a filling fraction of ϕ=0.17

2.6 Elimination and addition of Level Set Terms by Phase Shifts and Multiple Exposure

From a reductionist perspective an interference lithography pattern is simply a sum of registered gratings. The elimination of the problem of registration is what makes the formation of patterns via single exposure very practical. However from the perspective of achieving length scalable structures the idea of multiple exposure is very attractive. A further motivation behind this lies in the fact that for more complicated level set equations it might be possible that the constraint equations resulting from the comparison of the level set equation and the intensity equation are either difficult to solve, yield only trivial results, or require the utilization of polarisations that are challenging to achieve from an experimental perspective.

2.6.1 The scalable P structure

The P structure is a particular case of a cubic bicontinuous structure, in which the three terms that constitute the level set equation approximating this structure are all orthogonal to one another. This means that a shift in one of the gratings relative to the other two only produces a translation of the origin to the extent of the shift. The P structure can thus be viewed simply as a sum three perpendicular gratings, each of which can be written separately[4]. Since it is trivial to scale the size of a grating by changing the angle between the beams it is possible to make the P structure scalable without resorting to a change in wavelength. Tondiglia et al. [48] created an orthorhombic P structure in a Polymer Dispersed Liquid Crystal Matrix using a similar approach.

2.6.2 Diamond as two FCC lattices

Access to the bicontinuous diamond level set structure through a single exposure technique was outlined in secion 2.5.2 This particular diamond structure could potentially also be achieved via a multiple exposure route. This is instructive vis-a-vis constructing other structures which are the sum of two or more Bravais lattices. The diamond lattice can be viewed as two interpenetrating FCC lattices offset from one another by a translation of $\{\frac{1}{4}, \frac{1}{4}, \frac{1}{4}\}$. The first term level set equation for the FCC lattice is

$$\begin{aligned} F_{(111)} = &\cos 2\pi(x+y+z) + \cos 2\pi(x+y-z) \\ &+ \cos 2\pi(x-y+z) + \cos 2\pi(-x+y+z) \end{aligned} \tag{2.24}$$

[4]Clearly there is a consideration to be made from the perspective of the photoresist platform as it should support the linear addition of multiple exposures. This and other experimental considerations are examined in Chapter 4.

the beam parameters in this case are:

$$\begin{aligned} \overrightarrow{\mathbf{k}}_0 &= \pi/a[201] \quad & \overrightarrow{\mathbf{k}}_1 &= \pi/a[\bar{2}01] \\ \overrightarrow{\mathbf{k}}_2 &= \pi/a[0\bar{2}\bar{1}] \quad & \overrightarrow{\mathbf{k}}_3 &= \pi/a[02\bar{1}] \\ \overrightarrow{\mathbf{E}}_0 &= [0.183, -0.683, 0.707] \quad & \overrightarrow{\mathbf{E}}_1 &= [-0.183, 0.683, 0.707] \\ \overrightarrow{\mathbf{E}}_0 &= [-0.683, -0.183, 0.707] \quad & \overrightarrow{\mathbf{E}}_1 &= [0.683, 0.183, 0.707] \end{aligned} \tag{2.25}$$

The first exposure with these parameters fixes the origin. In the subsequent exposure, we introduce a phase shift in the beams so as to produce the $\{\frac{1}{4}, \frac{1}{4}, \frac{1}{4}\}$ translation. Since we do not shift the beams or the sample, registration is ensured. The phase shifts required to produce this particular translation are given by

$$\Delta\phi_0 = \pi/2 \quad \Delta\phi_1 = -\pi/2 \quad \Delta\phi_2 = -\pi \quad \Delta\phi_3 = 0 \tag{2.26}$$

If the second exposure is of the same time and intensity as the first then the sum of the two exposures gives us the bicontinuous diamond level set structure. Such a multiple exposure scheme based on phase shifts has been demonstrated in 2D and proposed for 3D by Chelnokov *et al.*[67]. In the case that the two exposures are unbalanced with respect to one another then the resultant structure will belong to the same space group as that of GaAs, viz. group 216. We can also envision accessing structures such as CaF_2 which is also made up by the sum of interpenetrating FCC lattices.

2.6.3 The Gyroid structure by elimination of terms

A multiple exposure technique allows us to reduce the number of constraints on the polarisation by eliminating the undesired terms via the superposition of multiple exposures. The procedure involves a first exposure with all the constituent beams. This ensures registration between subsequent exposures. A specific example is useful. Suppose we want to remove the term $\cos(2\pi z/a)$ from equation 2.10. We now expose the sample with all the beams blocked except $\overrightarrow{\mathbf{k}}_0$ and $\overrightarrow{\mathbf{k}}_3$. We also introduce a phase

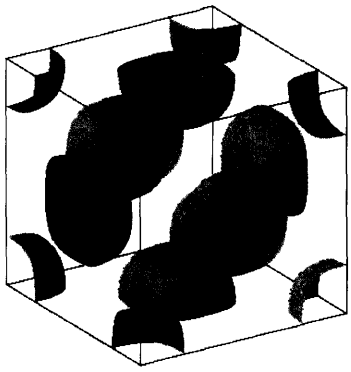

Figure 2-4: A level set structure having $Fm\bar{3}m$ symmetry. Note this structure is not bicontinuous for any volume fraction.

shift of π into beam 3. The reverses the sign of the coefficient for the cosine term, thereby eliminating its presence in the structure. A key side effect is the upward shift in the dc intensity offset of the pattern. We now show how to create the level set approximation to the noncentrosymmetric gyroid structure via this multiple exposure technique.

As before, since $I4_132$ is a noncentrosymmetric group it is necessary to use polarisations that are more general than linear polarisation. We achieve this by artificially breaking each wave into two waves that possess the same wave vector but different phases and linear polarisation vectors. Depending on the phase difference and the magnitudes of the polarisations of each set, the resultant wave will be linearly, circularly or elliptically polarised. In our case to achieve the trigonometric terms that we desire, we choose the difference between the phases to be $\pi/2$. The choice of $\overrightarrow{\mathbf{k}}$ vectors remains the same as in section 2.5.3. The choice of $\overrightarrow{\mathbf{k}}$ vectors and phases that we desire is thus given by

$$\begin{aligned}
\vec{\mathbf{k}}_0 = \vec{\mathbf{k}}_4 = \pi/a[\bar{1}\bar{1}\bar{1}] \quad \vec{\mathbf{k}}_1 = \vec{\mathbf{k}}_5 = \pi/a[11\bar{1}] \\
\vec{\mathbf{k}}_2 = \vec{\mathbf{k}}_6 = \pi/a[1\bar{1}1] \quad \vec{\mathbf{k}}_3 = \vec{\mathbf{k}}_7 = \pi/a[\bar{1}11] \\
\phi_0 = 0 \quad \phi_1 = 0 \quad \phi_2 = 0 \quad \phi_3 = 0 \\
\phi_4 = \pi/2 \quad \phi_5 = \pi/2 \quad \phi_6 = \pi/2 \quad \phi_7 = \pi/2
\end{aligned} \tag{2.27}$$

The resultant intensity has 13 terms and is given by

$$\begin{aligned}
I(\vec{\mathbf{r}}) = const &+ (\vec{\mathbf{E}}_0 \cdot \vec{\mathbf{E}}_1 + \vec{\mathbf{E}}_4 \cdot \vec{\mathbf{E}}_5) \cos(2\pi/a(x+y)) \\
&+ (\vec{\mathbf{E}}_0 \cdot \vec{\mathbf{E}}_2 + \vec{\mathbf{E}}_4 \cdot \vec{\mathbf{E}}_6) \cos(2\pi/a(x+z)) \\
&+ (\vec{\mathbf{E}}_5 \cdot \vec{\mathbf{E}}_6 + \vec{\mathbf{E}}_1 \cdot \vec{\mathbf{E}}_2) \cos(2\pi/a(y-z)) \\
&+ (\vec{\mathbf{E}}_0 \cdot \vec{\mathbf{E}}_3 + \vec{\mathbf{E}}_4 \cdot \vec{\mathbf{E}}_7) \cos(2\pi/a(y+z)) \\
&+ (\vec{\mathbf{E}}_1 \cdot \vec{\mathbf{E}}_3 + \vec{\mathbf{E}}_5 \cdot \vec{\mathbf{E}}_7) \cos(2\pi/a(x-z)) \\
&+ (\vec{\mathbf{E}}_6 \cdot \vec{\mathbf{E}}_7 + \vec{\mathbf{E}}_2 \cdot \vec{\mathbf{E}}_3) \cos(2\pi/a(x-y)) \\
&+ (\vec{\mathbf{E}}_1 \cdot \vec{\mathbf{E}}_4 + \vec{\mathbf{E}}_0 \cdot \vec{\mathbf{E}}_5) \sin(2\pi/a(x+y)) \\
&+ (\vec{\mathbf{E}}_2 \cdot \vec{\mathbf{E}}_4 + \vec{\mathbf{E}}_0 \cdot \vec{\mathbf{E}}_6) \sin(2\pi/a(x+z)) \\
&+ (\vec{\mathbf{E}}_1 \cdot \vec{\mathbf{E}}_6 + \vec{\mathbf{E}}_2 \cdot \vec{\mathbf{E}}_5) \sin(2\pi/a(y-z)) \\
&+ (\vec{\mathbf{E}}_3 \cdot \vec{\mathbf{E}}_4 + \vec{\mathbf{E}}_0 \cdot \vec{\mathbf{E}}_7) \sin(2\pi/a(y+z)) \\
&+ (\vec{\mathbf{E}}_3 \cdot \vec{\mathbf{E}}_5 + \vec{\mathbf{E}}_1 \cdot \vec{\mathbf{E}}_7) \sin(2\pi/a(x-z)) \\
&+ (\vec{\mathbf{E}}_2 \cdot \vec{\mathbf{E}}_7 + \vec{\mathbf{E}}_3 \cdot \vec{\mathbf{E}}_6) \sin(2\pi/a(x-y))
\end{aligned} \tag{2.28}$$

A multiple-exposure routine for the gyroid is thus as follows: The maximum number of exposures that we would need to retain the six sine terms and eliminate the six cosine terms is seven. The first exposure uses all the beams to ensure registration. Subsequent exposures involve the elimination of terms. For example, introducing a phase shift of ϕ into the beams 0,1,4 and 5 would eliminate the cosine term $cos[2\pi/a(x+y)]$ while retaining the corresponding sine term. The six term-eliminating exposures are as follows

Beams	Phase shift of π
0,1,4,5	1 and 4
0,2,4,6	2 and 4
5,6,1,2	1 and 6
0,3,4,7	3 and 4
1,3,5,7	3 and 5
6,7,2,3	2 and 7

In this manner we retain only terms that we desire in order to obtain a particular set of symmetries.

Chapter 3

Exploring for 3D photonic band gap structures in the 11 FCC space groups

In the previous chapter we established a technique that allowed us to target space groups and symmetry elements in structures created via the technique of interference lithography. The next important question that needs to be addressed is what symmetry elements do we wish to target? Clearly this is a very open ended question. In this chapter we attempt to answer this question for the particular case of photonic crystals. Towards this end we employ the level set technique to develop a method that allows us to systematically search for structures that possess photonic band gaps. We use this technique to explore the 11 FCC space groups and identify a new photonic band gap structure. This search gives us an important insight into the structural elements that help support gaps. [1]

3.1 Photonic Crystals

As described in section 1.1.1, photonic crystals are the three dimensional analogue of Fabry-Perot resonators. [1] A more complete mathematical description is obtained

[1]The primary conclusions of this chapter have been reported in Maldovan *et al.* [68]

by examining Maxwell's equations for such systems and viewing these structures as the optical analogues of semiconductors. In semiconductors the periodic potential of the atoms prevents the propagation of electrons with certain energies in particular directions, this range of energies is the energy or band gap. If the potential is large enough the gap extends in all directions, denoted by a complete band gap. The optical analogue in Maxwell's equations, of the lattice potential in the Schroedinger equation, is the dielectric constant. Thus if we consider a material with a periodic variation in the dielectric constant we could describe the dispersion relationship, $\omega(\overrightarrow{\mathbf{k}})$, of the photons propagating in these structures by a band structure, just as in the case of the electrons. Further, if the dielectric variation is large enough, and the absorption of light in the crystal sufficiently low, then a photonic band gap (PBG) can arise. A PBG is a range of frequencies for which light is forbidden to propagate within certain directions. As in semiconductors a complete PBG is said to exist when the gap extends in all directions. Typically when one talks about photonic crystals the target property is the PBG of the structure. A measure of the band gap for a particular structure is usually taken to be the gap to mid gap ratio.

$$\frac{\omega_h - \omega_l}{(\omega_h + \omega_l)/2} \tag{3.1}$$

where ω_h is the lowest frequency in the upper band and ω_l is the highest frequency of the lower band.

3.2 Searching for Band Gaps

3.2.1 Established Structures

Since the primary promise of photonic crystals and their potential applications [69, 70] is in dealing with wavelengths in the visible and near infra-red, this has meant creating complicated three dimensionally periodic structures with lengthscales on the order of a micron or less. This has meant that considerable attention has been drawn towards the establishment of periodic dielectric structures that in addition to possessing robust

complete bandgaps, can be easily fabricated by some of the techniques described in section 1.2. A number of theoretical structures that aim to create a happy compromise between both the requirements have been proposed [71, 72, 73, 74, 75, 76, 77, 78, 79, 80, 47]. To date, the best ("champion") complete photonic bandgap structure is that of diamond networks having Fd3m symmetry (2-3 gap) with a gap to mid gap ratio of 0.31 for a volume fraction of 0.19 and a dielectric contrast of 13:1 [81]. The only other known complete bandgap in a face-centred-cubic (FCC) lattice structure is that of air spheres in a dielectric matrix (8-9 gap); the so called 'inverse-opal' structure. This is a much less desirable gap with a gap to mid gap ratio of only 6% at f=0.26 and a dielectric contrast of 13:1 [71]. Importantly, to date, there is no systematic approach to discovering champion photonic crystal structures. Here we propose a level-set approach based on crystallography to systematically examine for photonic bandgap structures and illustrate this approach by applying it to the 11 FCC groups. This systematic approach gives us an insight into the effects of symmetry and connectivity. We classify the F-space groups into four fundamental geometries on the basis of the connectivity of high-symmetry Wyckoff sites. Three of the fundamental geometries studied display complete bandgaps, including two: the F-RD structure with $Fm\bar{3}m$ symmetry and a group 216 structure with $F\bar{4}3m$ symmetry that have not been reported previously. By using this systematic approach we were able to discover structures that open gaps between the 2-3, 5-6 and 8-9 bands in the FCC systems.

3.2.2 The Level Set approach to exploring for Photonic Band Gaps

The existence and characteristics of photonic bandgaps depend on such factors as the dielectric contrast and volume fractions, as well as the symmetry, connectivity and geometrical shape of the periodic dielectric structure. Although the nature of the dependencies is not clearly established, any attempt at a structured approach to find three-dimensional (3D) photonic crystal designs with complete bandgaps should incorporate these parameters.

The symmetries of a periodic structure are characterized by its space group. Our technique is to ensure a structure with a specified space group through the level-set approach based on structure factors [66] that was successfully employed in chapter 2. Candidate structures were modelled for each group using a 3D surface given by f(x,y,z) - t = 0, which defines the interface that separates regions of dissimilar dielectric properties obtained by equating f to an appropriate sum of structure factor terms. The band structure is then calculated as a function of the remaining parameters, such as volume fraction (determined by the parameter t), connectivity and so on. In particular the level-set approach allows us to easily map photonic crystals with different connectivities, within a chosen space group, as structure factor terms with greater hkl index fill and connect Wyckoff sites of greater multiplicity and decreasing symmetry; varying the hkl values affects the complexity of the connectivity.

The band structure calculations[2] were performed by solving Maxwell's equations numerically. The plane wave method was used in the full vectorial formulation [71]. The photonic structure is characterised by a real positive dielectric constant $\epsilon(\overrightarrow{\mathbf{r}})$. The magnetic permeability is taken assumed equal to one. By combining Maxwell's equations, the fundamental equation

$$\overrightarrow{\nabla} \times \overrightarrow{\nabla} \times \overrightarrow{\mathbf{E}} = \frac{\omega^2}{c^2} \epsilon(\overrightarrow{\mathbf{r}}) \overrightarrow{\mathbf{E}} \tag{3.2}$$

is obtained. Where ∇ is the curl operator, ω is the angular frequency and c is the speed of light. The dielectric constant and the electric field E are expanded in a sum of plane waves and substituted into the fundamental equation. A generalized eigenvalue problem, represented by a Hermitian matrix, is obtained. By using standard LAPACK subroutines, the eigenvalues (allowed propagating frequencies) are calculated. By mapping directions and wavelengths of the electromagnetic waves in the corresponding Brillouin zone, the complete range of allowed and prohibited frequencies (photonic bandgap) is obtained.

[2]The band structure calculations were performed by Martin Maldovan using code written by him.

In the present calculations we take

$$\begin{aligned} for \quad & f(x,y,z) - t < 0 \quad \epsilon_{network} = 13 \\ for \quad & f(x,y,z) - t > 0 \quad \epsilon_{matrix} = 1 \end{aligned} \tag{3.3}$$

where ϵ is the dielectric constant. The function f(x,y,z) is equated to a structure factor term $F_{(hkl)}$ from the chosen space group. The general structure factor term is obtained by incorporating all the equivalent positions of the most general point in the unit cell. This equation possesses all the symmetry elements of the chosen space group. Certain allowed terms with special hkl values may impart more symmetry than a general allowed term hkl. If the particular $F_{(hkl)}$ term contains more symmetry than desired, then another hkl term is included. This addition of terms ensures that the greatest common symmetries of the terms are passed to the function f(x,y,z). The bandgaps are determined below as a function of the volume fraction by varying the parameter t.

The 11 FCC space groups and their numbers are: $F23$ (196), $Fm\bar{3}$ (202), $Fd\bar{3}$ (203), $F432$ (209), $F4_132$ (210), $F\bar{4}3m$ (216), $F43\bar{c}$ (219), $Fm\bar{3}m$ (225), $Fm\bar{3}c$ (226), $Fd\bar{3}m$ (227), $Fd\bar{3}c$ (228). As an example derivation of an f(x,y,z) function, consider group 203 (origin choice 2). The general structure factor formula is given by:

$$F_{(hkl)}(x,y,z) = \sum_{i=1}^{n} \cos\left[2\pi(hx_i + ky_i + lz_i)\right] + i \sin\left[2\pi(hx_i + ky_i + lz_i)\right] \tag{3.4}$$

where the presence of only one type of scatterer is assumed (this corresponds to a two-component dielectric/air structure). For group 203, the general position has 96 equivalent positions, therefore n = 96 in equation 3.4. As there is an inversion centre at the origin, the structure factor is real. Equation 3.4 can be written for group 203

as

$$
\begin{aligned}
F_{(hkl)}(x,y,z) =& 8\cos^2[2\pi\frac{(h+k)}{4}]\cos^2[2\pi\frac{(k+l)}{4}]\{\cos[2\pi(hx+ky+lz)] \\
&+\cos[2\pi(hx+ky-lz-(h+k)/4)] \\
&+\cos[2\pi(hx-ky+lz-(l+h)/4)] \\
&+\cos[2\pi(-hx+ky+lz-(k+l)/4)]+\cos[2\pi(hy+kz+lx] \\
&+\cos[2\pi(hy+kz-lx-(h+k)/4)] \\
&+\cos[2\pi(hy-kz+lx-(l+h)/4)] \\
&+\cos[2\pi(-hy+kz+lx-(k+l)/4)] \\
&+\cos[2\pi(hz+kx+ly]+\cos[2\pi(hz+kx-ly-(h+k)/4)] \\
&+\cos[2\pi(hz-kx+ly-(l+h)/4)] \\
&+\cos[2\pi(-hz+kx+ly-(k+l)/4)]\} \qquad (3.5)
\end{aligned}
$$

Appropriate hkl values are chosen to guarantee the symmetries of the 203 group. In general, to keep the genus of the group low, smaller hkl values are used, as structures with complex topologies tend not to support bandgaps. If the first term with the desired symmetry has a large hkl value then a lower hkl value is added to diminish the complexity while retaining the desired space group. Only those combinations of hkl that are allowed reflections for the space group are examined. The first acceptable reflection for group 203 is (135) and a suitable lower hkl term is (111). The final surface defining the dielectric distribution is given by

$$f(x,y,z) - t = sF_{(111)}(x,y,z) + (1-s)F_{(135)}(x,y,z) - t = 0 \qquad (3.6)$$

where s can vary between 0 and 1. Varying the parameter s allows us to smoothly traverse the intermediate structures between different connectivities[66]. A full exploration of the s and t parameters could allow for possible optimization of a bandgap. Candidate equations for the remaining 10 FCC space groups can be generated in a similar manner. The space groups and the hkl terms that generate the bandgaps

calculated are listed in Table 3.1.

3.3 Gap Maps and Fundamental Geometries

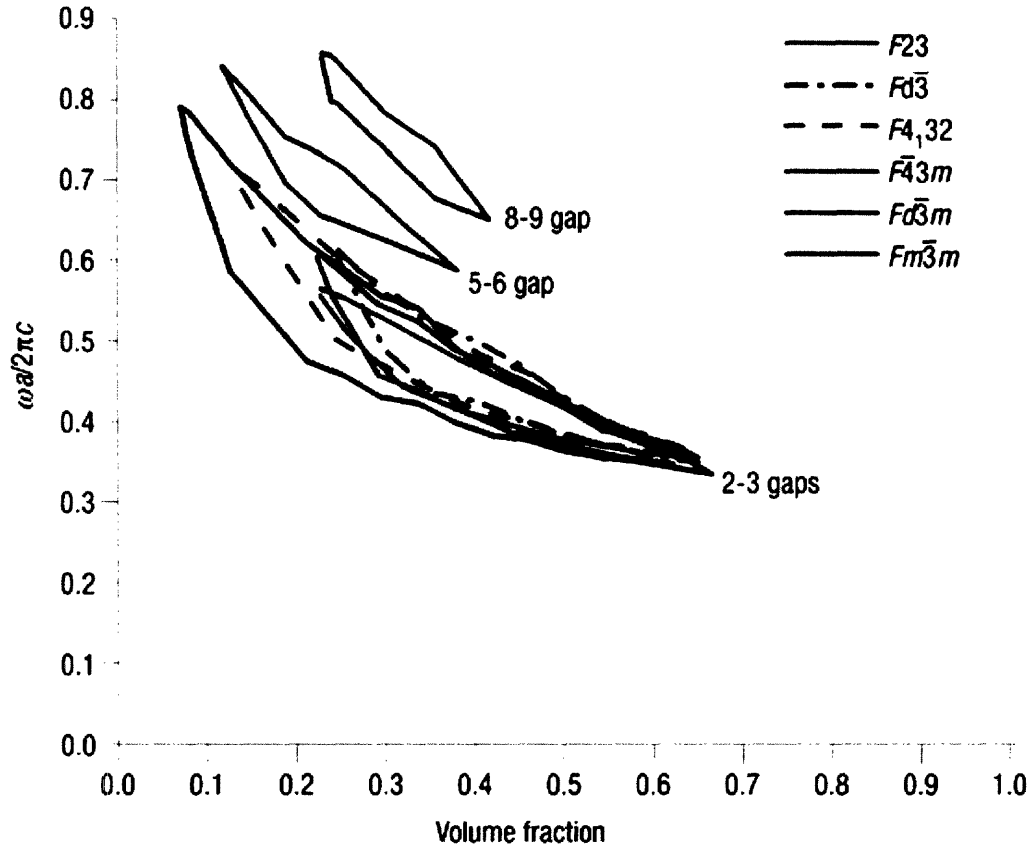

Figure 3-1: Bandgap maps for the FCC structures as a function of volume fraction. The dielectric contrast is 13:1. Structures that possess bandgaps and share the same fundamental geometry show gaps in the same region.

Figure 3-1 is a plot of bandgap versus volume fraction for the structures that were demonstrated to display a complete gap. It is apparent that the gap map has three regions: 2-3 gap, 5-6 gap and 8-9 gap. A basic set of symmetries defines the structural connectivity and the essential bandgap. The remaining symmetry elements modify the bandgap. An examination of the corresponding photonic structures shows that they possess one of three 'basic' geometries, Figure 3-2. The structural differences

Space Group	Structure Factor Term (hkl)	$Fm\bar{3}m$ occupancy (basic geometry)	Gap
196 ($F23$)	$0.25(F^A_{(111)} + F^B_{(111)} + F^A_{(024)} + F^B_{(024)})$	4a + half tetrahedral sites 8c (diamond)	Yes
202 ($Fm\bar{3}$)	$0.5(F_{(111)} + F_{(024)})$	4a + all tetrahedral sites (F-RD)	No
203 ($Fd\bar{3}$)	$0.5(F_{(111)} + F_{(135)})$	4a + half tetrahedral sites 8c (diamond)	Yes
209 ($F432$)	$0.25(F^A_{(111)} + F^B_{(111)} + F^A_{(135)} + F^B_{(135)}))$	4a (FCC)	No
210 ($F4_132$)	$0.5(F_{(111)} + F_{(024)})$	4a + half tetrahedral sites 8c (diamond)	Yes
216 ($F\bar{4}3m$)	$0.75F_{(111)} + 0.25F_{(024)}$	4a (FCC)if f<0.17 4a + half tetrahedral sites (diamond)	Yes Yes
219 ($F\bar{4}3c$)	$0.25(F^A_{(002)} + F^B_{(002)} + F^A_{(135)} + F^B_{(135)}))$	4a + all tetrahedral sites 4b (NaCl)	No
225 ($Fm\bar{3}m$)	$F_{(111)}$	4a (FCC)	No
	$0.5(F_{(111)}+F_{(022)})$	4a + all tetrahedral sites 8c (F-RD)	Yes
226 ($Fm\bar{3}c$)	$0.5(F_{(002)} + F_{(135)})$	4a + all octahedral sites 4b (NaCl)	No
227 ($Fd\bar{3}m$)	$F_{(111)}$	4a + half tetrahedral sites 8c (diamond)	Yes
228 ($Fd\bar{3}c$)	$0.5(F_{(022)} + F_{(135)})$	4a + all octahedral sites 4b (NaCl)	No

Table 3.1: Summary of complete bandgaps and fundamental geometries for the level-set structures possessing a FCC lattice. The basic geometry of all 11 FCC space groups is given with reference to occupancy of Wyckoff sites specified by group 225. f = volume fraction.

can be visualized by placing spheres at the nodes of the networks as shown on the left structures of Fig. 3-2. The three basic geometries with bandgaps can be described with reference to space group 225 and the connectivity of the various types of Wyckoff sites. These are $Fm\bar{3}m$ with Wyckoff sites 4a ($m\bar{3}m$ symmetry) occupied (for example, simple FCC in Fig. 3-2(b).), $Fm\bar{3}m$ with sites 4a plus half of the tetrahedral sites 8c ($\bar{4}3m$ symmetry) occupied (for example, diamond, Fig. 3-2a,c), and $Fm\bar{3}m$ with sites 4a plus all of the tetrahedral sites 8c ($\bar{4}3m$ symmetry) occupied (for example, F-RD, Fig. 3-2d). Those structures with diamond-like geometry have their 2-3 bandgaps clustered around the region defined by the bandgap of group 227 (Fig. 3-1.), whereas the F-RD structure (group 225) has its 8-9 gap in a separate region. The 216 structure shows both 2-3 and 5-6 gaps and, for certain volume fractions, the coexistence of both. Below pinch-off ($f < 0.17$) the 216 structure shows a weak 5-6 gap and resembles a simple FCC structure. Above pinch-off ($f > 0.17$) this structure shows strong 2-3 and 5-6 gaps and resembles the diamond (although it does not possess diamond symmetry). This is the first prediction that F-RD and 216 possess a complete bandgap. None of the structures examined that display the NaCl basic geometries ($Fm\bar{3}m$ with sites 4a plus all of the octahedral sites 4b ($m\bar{3}m$ symmetry) occupied) have bandgaps. This suggests that a basic connectivity determines the existence of a photonic gap. Additional structural complexity modifies the bandgap – sometimes even closing it. With incorporation of higher hkl terms, the level-set approach creates a surface that connects Wyckoff sites of lower point symmetry. Surfaces generated with higher hkl values are less likely to have gaps because at higher hkl values the network topology becomes too complex.

This can be cast in different words by saying that structures that are described by low order Fourier terms tend to support band gaps. This is true since the structure factor terms that are used to define particular structures are nothing but Fourier terms belonging to their respective space groups. The addition of higher hkl terms implies the addition of higher order Fourier terms. This result has been shown to give a strong physical insight by viewing the low order Fourier terms as sinusoidal modulations in the dielectric constant along principal directions in high symmetric

real-space lattices [82]. Here it is argued that the sinusoidal modulations function as Bragg gratings, each of which has a band gap associated with it. Thus, if the overlap between the gaps of the various gratings is sufficient the resultant structure possesses a complete photonic band gap, barring any closures due to symmetry considerations. Shorter wavelength dielectric modulations, i.e. along the principal directions of the reciprocal lattice, of equal modulus were found to support larger gaps.

It is interesting to note that a large number of the already established complete bandgap structures (for example, spheres on a diamond lattice[72], rods connecting nearest neighbour sites in a diamond lattice[81], the woodpile structures[83], Yablonovite[73], the MIT structure[78], ABC-type hexagonal structure[79], the D structure found in self-assembled polymeric structures[80] and the diamond-like structure made by interference lithography [47]) possess the connectivity of the diamond network. Their bandgaps are therefore clustered around the region defined by the gap of group 227. Thus, although the level-set technique will not directly yield specific structures that are particularly suited for fabrication by specific techniques (for example, the woodpile structure by layer-by-layer conventional semiconductor fabrication), nevertheless, it is important to note that this technique can be used to establish less specific structures and the important connectivities that support gaps. Once a particular connectivity has been established to support a gap, specific structures can be modified using other considerations such as ease of fabrication.

For example, a simplification of the diamond network structure (group 227) results in a modified version[84] of the woodpile structure[83]. Furthermore, structures suggested by the sphere model might be accessible by colloidal self-assembly, whereas structures defined by level-set equations could be accessed through interference lithography[60] or block-copolymer self-assembly[36]. Because the body-centred-cubic (b.c.c.)-based gyroid network structure has been demonstrated to have a complete gap almost as wide as that of diamond[80], other structures with b.c.c. symmetries provide an interesting set for further study by this level-set technique.

In summary, the level-set approach allows exploration of space groups to find structures with complete bandgaps. By using this systematic technique 2-3, 5-6 and

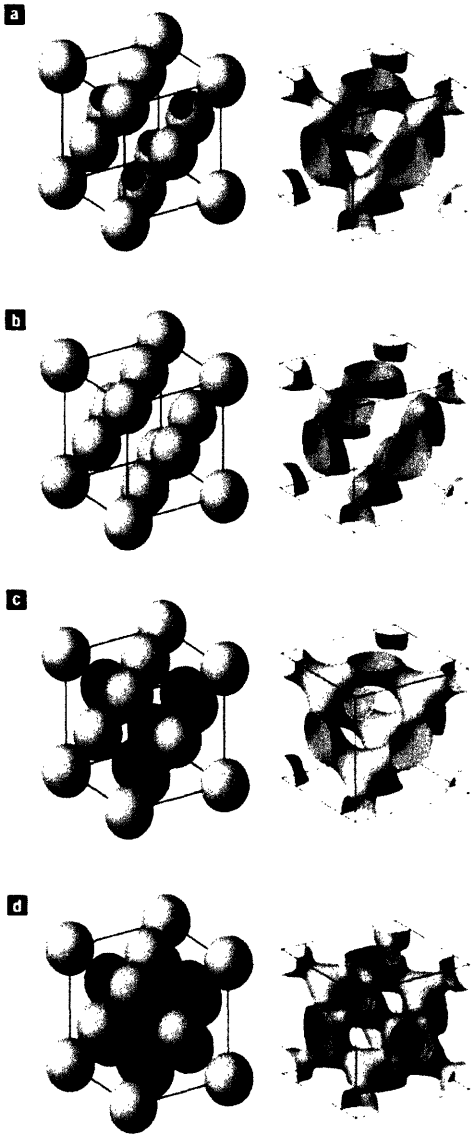

Figure 3-2: Three-dimensional representations of the sphere and level-set models for the basic FCC lattice geometries. a.) the connected $F\bar{4}3m$ (group 216) structure (volume fractions greater than 0.17). The structure displays the 2-3 and 5-6 gap. Note the inequality of the two set of sites (large versus small spheres). b.) The disconnected $F\bar{4}3m$ (group 216) structure (volume fractions lower than 0.17) This structure displays a weak 5-6 gap by virtue of being in the low volume fraction limit of a. It resembles a simple FCC geometry but the objects occupying the normal FCC $4a$ positions have point symmetry $\bar{4}3m$ so the space group is $F\bar{4}3m$ (group 216) not $Fm3m$ (group 225). c.) Diamond geometry (group 227) illustrated with a volume of 0.27. d.) *F-RD* geometry having $Fm3m$ (group 225) symmetry with a volume fraction of 0.35. The geometry of the *F-RD* resembles that of the inverse-opal

8-9 gaps were opened in the FCC lattices and we discovered the F-RD and 216 structures have complete bandgaps.

Chapter 4

Photonic Crystal Templates through Holographic Lithography

From the previous chapters we have gained insight into the structures that are accessible through the technique of interference lithography and the nature of the elements that we wish to incorporate into our structures. In this chapter we examine the fabrication of some structures that are promising particularly from the point of view of their photonic band gap properties.[1]

4.1 Photonic Crystal Templates: Approximations to the P, G and D

From the perspective of photonic crystals, the target property is clearly the band gap associated with the structure. Of the various photonic crystal families, the diamond-based structures have received the most attention due to their outstanding band gap properties. As was discussed in chapter 3, in order to arrive at structures that support band gaps we target those that have sinusoidal modulations in real space that are along reciprocal lattice vectors that are the closest to the origin. Symmetric and short modulations give rise to large photonic band gap structures [82]. If we apply this idea

[1]The primary results of this chapter have been reported in [85]

to the simple cubic, face centered cubic and body centered cubic lattices then we end up with the level set approximations to the Schwartz P, Diamond and Gyroid surface families. The reciprocal lattice vectors that are used are the $< 100 >, < 111 >$ and $< 110 >$ families respectively. The equations describing the structures are, as before,

$$F_P(x,y,z) = \cos 2\pi x + \cos 2\pi y + \cos 2\pi z + t \tag{4.1}$$

$$\begin{aligned} F_D(x,y,z) = &\sin 2\pi(x+y+z) + \sin 2\pi(x+y-z) \\ &+ \sin 2\pi(x-y+z) + \sin 2\pi(-x+y+z) + t \end{aligned} \tag{4.2}$$

$$\begin{aligned} F_G(x,y,z) = &\sin 2\pi(x+y) + \sin 2\pi(x-y) \\ &+ \sin 2\pi(y+z) + \sin 2\pi(y-z) \\ &+ \sin 2\pi(x+z) + \sin 2\pi(z-x) + t \end{aligned} \tag{4.3}$$

where the parameter t is used to control the volume fraction of the structure. For $F(x,y,z) - t > 0$, $\epsilon =$ high and for $F(x,y,z) - t < 0$, $\epsilon = 1$. These structures display large and complete band gaps, as shown in Fig. 4-1, with a maximum gap to midgap ratio of 13%, 27% and 24 % respectively at a dielectric contrast of 13:1.

Despite displaying large band gaps that are robust with respect to volume fraction variations, from the point of view of fabrication via four-beam interference lithography, however, the diamond and the gyroid structures possess some unfavorable characteristics. The wavelength of the laser fixes the size of the unit cell. Second, inspection of the $\vec{\mathbf{k}}$ vectors indicates that the beams are not all launched from the same side of the substrate. This implies that in order to fabricate these structures, one would have to use a transparent substrate. This is an important consideration in the fabrication of photonic crystals given the fact that many of the promising applications of photonic crystals lie in integrated on chip optical circuits for which silicon is opaque to visible light.

The P structure, when fabricated by single exposure does not suffer from this problem. Still, in this scheme the P structure is not scalable. However, as was mentioned in section 2.6.1, the P structure can be viewed as a sum of three perpendicular gratings between which registration is not an issue. Through a careful choice of beams

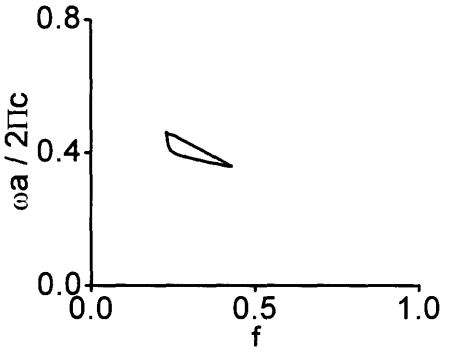

(a) Gap Map of the Single P level set structure

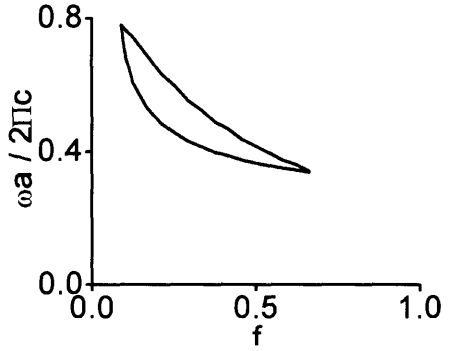

(b) Gap Map of the Single D level set structure

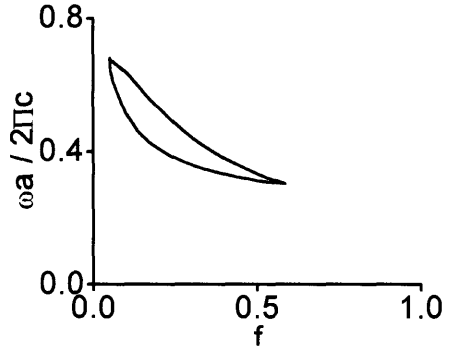

(c) Gap Map of the Single Gyroid level set structure

Figure 4-1: Gap Maps for the structures with the shortest and symmetrically distributed sinusoidal modulations in the principal directions for the simple cubic, FCC and BCC lattices. The dielectric contrast assumed is 13:1.

and directions we can ensure that that a scalable P is possible with all of the recording beams launched from the same half-space. In the case of the diamond and gyroid to negotiate this problem we go back to the idea of sinusoidal modulations along principal directions and relax the requirement that modulations occur in all the symmetric directions. This is the same as using fewer terms in the level set equation and results in structures that have all the recording beams launched from the same half space, while still retaining band gaps, albeit reduced.

In the case of both the FCC and BCC lattices the highest number of terms we can retain while still having all the beams launched from the same half space is three. The equations for these two structures, which we call the "3-FCC" ($F_{D'}$) and "3-BCC" ($F_{G'}$) are given by:

$$F_{D'}(x,y,z) = \sin 2\pi(x+y-z) + \sin 2\pi(x-y+z) + \sin 2\pi(-x+y+z) + t \quad (4.4)$$

$$F_{G'}(x,y,z) = \sin 2\pi(y+z) + \sin 2\pi(y-z) + \sin 2\pi(z-x) + t \quad (4.5)$$

The 3-FCC and 3-BCC structure are shown in Fig. 4-2. Example beam parameters for single exposure routines for the P, 3-FCC and 3-BCC structures are listed in table 4.1 It is important to note that despite the names and the nature of the approximation these structures are not FCC and BCC structures respectively but in fact belong to completely different space groups. They retain gaps because their fundamental geometries strongly related to the parent diamond and gyroid structures respectively. Their Gap Maps are shown in Fig 4-3. It is interesting to note that the structure with fcc translational symmetry possesses two complete band gaps. Structures that demonstrate multiple resonances could find application in multifrequency amplifiers and broad band reflectors.

Table 4.1: Beam parameters for the four beam setup of the three terms simple cubic P surface, diamond - like and two different beam parameter solutions for the gyroid-like structures. Note that all beams are launched into the photoresist from the same half space.

Structure	$\vec{\mathbf{k}}$ vectors	Example Polarizations
	$\vec{\mathbf{k}}_0 = \pi/a[111]$	$\vec{\mathbf{E}}_{00} = 1.00[0, 0.707, -0.707]$
Simple cubic	$\vec{\mathbf{k}}_1 = \pi/a[\bar{1}11]$	$\vec{\mathbf{E}}_{01} = 0.632[-0.5, 0.309, -0.809]$
P surface	$\vec{\mathbf{k}}_2 = \pi/a[1\bar{1}1]$	$\vec{\mathbf{E}}_{02} = 0.874[0.809, 0.5, -0.309]$
	$\vec{\mathbf{k}}_3 = \pi/a[11\bar{1}]$	$\vec{\mathbf{E}}_{03} = 2.288[-0.309, 0.809, 0.5]$
Three term	$\vec{\mathbf{k}}_0 = \pi/a[333]$	$\vec{\mathbf{E}}_{00} = 4.897[0.612, -0.774, 0.161]$
"Diamond-like"	$\vec{\mathbf{k}}_1 = \pi/a[511]$	$\vec{\mathbf{E}}_{01} = 4.000[0.25, -0.905, -0.346]$
structure	$\vec{\mathbf{k}}_2 = \pi/a[151]$	$\vec{\mathbf{E}}_{02} = 5.789[0.346, -0.25, 0.905]$
	$\vec{\mathbf{k}}_3 = \pi/a[115]$	$\vec{\mathbf{E}}_{03} = 12.94[0.905, 0.346, -0.25]$
Three term	$\vec{\mathbf{k}}_0 = \pi/a[111]$	$\vec{\mathbf{E}}_{00} = 1.414[0.707, -0.707, 0]$
"Gyroid-like"	$\vec{\mathbf{k}}_1 = \pi/a[\bar{1}11]$	$\vec{\mathbf{E}}_{01} = 1.414[0.707, 0.707, 0]$
'structure	$\vec{\mathbf{k}}_2 = \pi/a[1\bar{1}1]$	$\vec{\mathbf{E}}_{02} = 1.414[0.707, 0.707, 0]$
	$\vec{\mathbf{k}}_3 = \pi/a[11\bar{1}]$	$\vec{\mathbf{E}}_{03} = 2.449[0.408, 0.408, 0.816]$
Three term	$\vec{\mathbf{k}}_0 = \pi/a[333]$	$\vec{\mathbf{E}}_{00} = 5.657[0.707, -0.707, 0]$
"Gyroid-like"	$\vec{\mathbf{k}}_1 = \pi/a[511]$	$\vec{\mathbf{E}}_{01} = 6.164[0.162, 0.162, -0.973]$
structure	$\vec{\mathbf{k}}_2 = \pi/a[151]$	$\vec{\mathbf{E}}_{02} = 6.164[0.162, 0.162, -0.973]$
	$\vec{\mathbf{k}}_3 = \pi/a[115]$	$\vec{\mathbf{E}}_{03} = 12.693[0.680, 0.680, -0.272]$

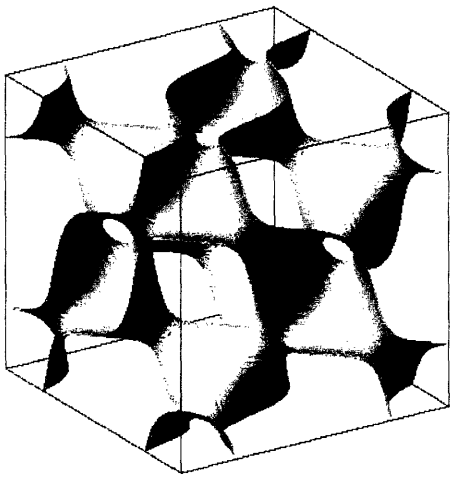

(a) The 3-FCC structure. Each node has a connectivity of four.

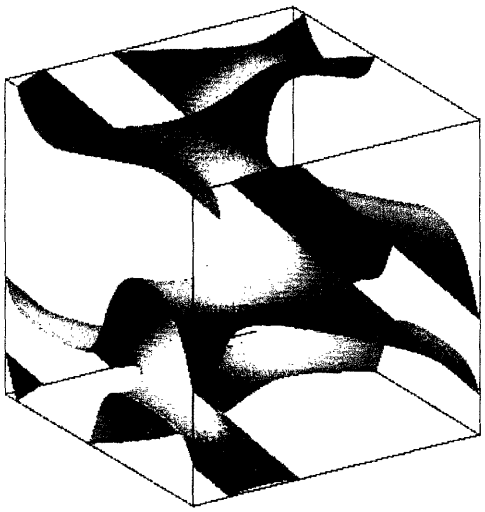

(b) The 3-BCC structure. Each node has a connectivity of three.

Figure 4-2: Fabricable 3 term approximations to the diamond and gyroid level set structures that retain complete band gaps, although of significantly reduced widths.

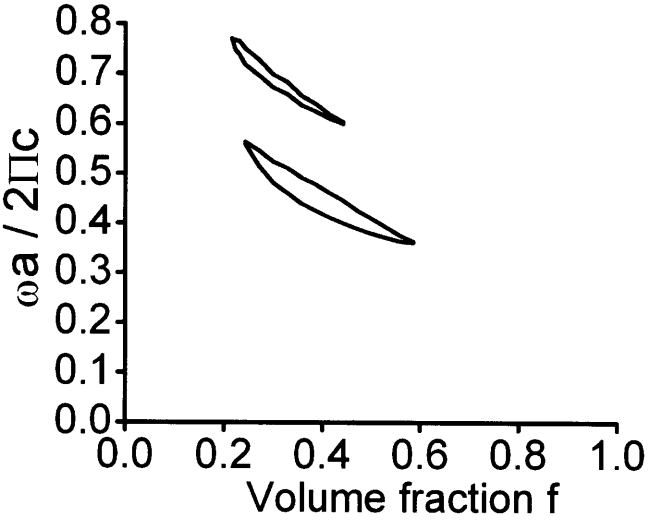

(a) 3-FCC

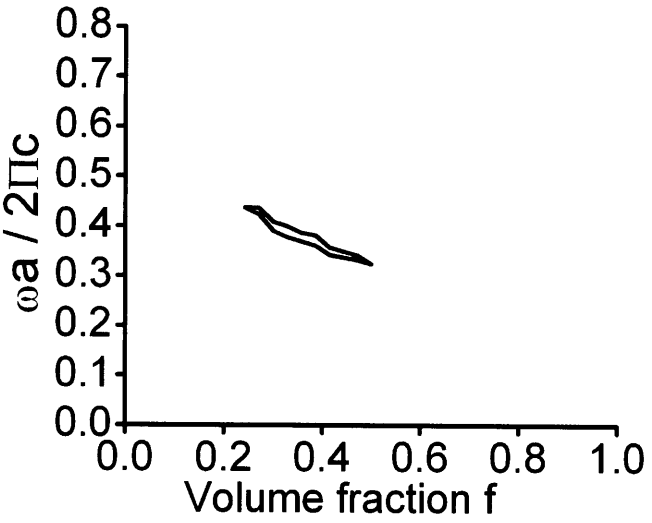

(b) 3-BCC

Figure 4-3: Gap maps associated with the 3-FCC and 3-BCC structures. The dielectric contrast assumed is 13:1

4.2 Transferring Interference Patterns into Templates

The P structure and the 3-FCC pattern were transferred into an epoxy based photoresist platform. The patterns were created using the stable, Gaussian TEM_{00} output beam from a frequency doubled $Nd:YVO_4$ laser. The profile of the beam was not modified any further and the $1/e^2$ beam diameter was measured to be 3.4mm. In the beam setup, intensities were controlled by using a combination of a half wave plate followed by a polarizing beam splitter. The half wave plate allows us to control the incoming polarization and hence the relative intensities of the two perpendicularly polarized output arms of the beam splitter. Appropriate beam directions were ensured by adjusting the position of the mirrors with respect to the sample. The final polarization of each of the beams was controlled by placing a half wave plate in the path of the concerned beam. This was always the last optic. Care was also taken to ensure that the reflection from the surface of the mirrors did not introduce any ellipticity into the linearly polarized light.

A further practical consideration is the preservation of polarisations and beam directions once the light enters the photoresist. In order to ensure this, a coupling prism was used whose shape was such that any of the interfering beams would always enter normal to the prism surface. Prisms were fabricated by filling and sealing hollow glass prisms with a refractive index fluid (Cargille series A refractive index liquid) matching that of the photoresist. The final surface was always an index matched glass (F7 Schott Glass). Optical contact between the photoresist surface and the final prism surface was ensured by using a random block copolymer silicone oil (Dow-Corning) with a refractive index matched to the photoresist.

The P structure was fabricated in two orientations - (1) with the [100] direction perpendicular to the substrate as shown in fig 4-4; this was necessarily a multiple exposure route, and (2) with the [111] direction perpendicular to the substrate, as shown in Fig. 4-5. In this case, all the beams were from the same half space and this routine could be done either by multiple exposure or a single exposure. In both cases

the structure is scalable.

The 3-FCC structure was achieved by a single exposure. The prism configuration for this setup is shown in fig. 4-6.

Several photoresist platforms were examined[2]. The most robust platform was found to be a modified SU-8 platform [51]. Epon SU-8 is a multifunctional (8-functional) epoxy derivative of a bisphenol-A Novolac®, which forms glassy films at room temperature. The formulation includes a photosensitizer, a photoacid generator or PAG, the epoxy and a contrast enhancing additive, all dissolved in a solvent. The photosensitizer serves to absorb the incident light. The photoacid generator combines with the photosensitizer to form a charge transfer complex which results in the formation of an acid. Exposure to the interference pattern thus results in a spatial variation of acid in the photoresist. Upon heating the photoresist above its glass transition temperature, the photoacids initiate ring-opening polymerization reactions of the epoxy groups and the acids are regenerated in the subsequent steps. This results in the formation of crosslinked polymer in the areas of high intensity of light. The uncrosslinked monomer is then washed away in an appropriate solvent. One advantage of using an acid catalysed photoresist platform as opposed to one based on free radical polymerisation lies in the fact that there is no refractive index change during the exposure step. Such a situation would limit the thickness of the film that could be patterned due to the fact that in thicker films the beams would diffract off the structure as it was being written. A workaround for this might be to use a very fast pulsed laser, whose writing times are shorter than the time scale on which the polymerisation takes place. This can however complicate the optical setup since overlapping very short pulses, while maintaining the required angles is not an easy task.

In our experiments one of three photosensitizers, listed in order of increasing quantum efficiency, were used - rubrene (Sigma-Aldrich), 2,4,5,7-tetraidoo-6-hydroxy-3-fluorone ($h\nu$ - 535 from Spectra Group), and irgacure - 261 (CIBA-Geigy). The

[2]This involved collaborative work with several skilled chemists - Dr. Shu Yang, Dr. Ji-Hyun Jang and Dr. Lalgudi Natarajan

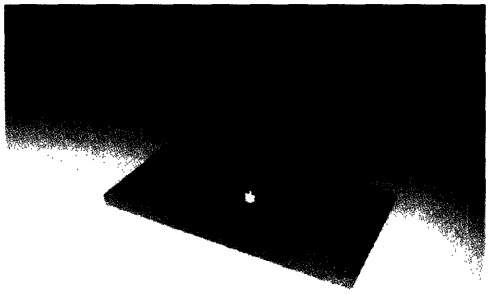

(a) Exposure 1

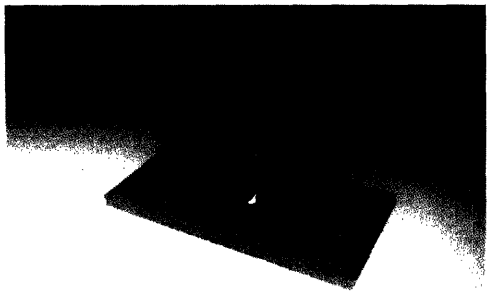

(b) Exposure 2

(c) Exposure 3

Figure 4-4: Prism setup and multiple exposure routine for the [100] configuration of the P structure. This routine implies the use of a transparent substrate. Beam directions are indicated by large arrows and electric field vectors by the small side arrows.

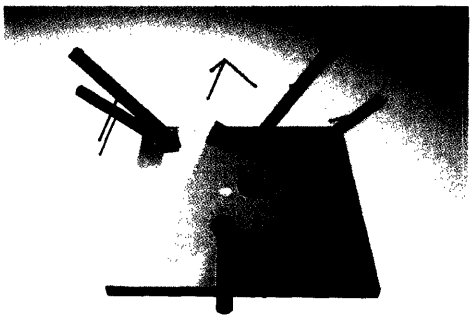

Figure 4-5: Prism setup for [111] configuration of the P structure.Beam directions are indicated by large arrows and electric field vectors by the small side arrows.

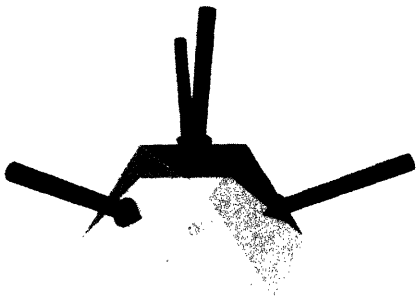

Figure 4-6: Prism setup for the fabrication of the 3-FCC structure. Beam directiong are indicated by the large arrows. The polarisation directions are listed in table 4.1

rubrene was found to dissolve well in the epoxy and did not suffer from inhomogeniety that was sometimes observed with the hν-535. However thicker films were more difficult to access using rubrene because of its higher absorption. This resulted in thinner samples (usually 5μm thick) and some chirp across the sample. While the irgacure gave thicker films it was more difficult to get good structures for patterns with periodicities under a micron. Furthermore it was used sparingly due to its limited availability. The photoacid generator used in the case of hν-535 and rubrene was diaryliodonium hexafluoroantimonate (UVACure 1600 from UCB Radcure). Irgacure did not require a separate photoacid generator.

The need for a contrast agent[3] varied depending on the structure being exposed. The contrast for a set of beam parameters depends on the extent of overlap of the polarisations and the variation in the magnitude of the electric fields of the interfering beams. These factors affect the magnitude of the constant (or d.c. offset) term with respect to the coefficients of the sinusoidal terms in the intensity equation. Since the polymerisation reaction is acid catalysed, a base was added to scavenge some of the acid generated in order to reduce the effect of the d.c offset as per [51]. Depending on the boiling point of the solvent used for the photoresist either Triethylamine (TEA - b.p. 85^{o}C) or Tributylamine was used (TBA - b.p.215^{o}C).

The P structure and the 3-FCC structure were transfered into the epoxy based photoresist. Films spun cast resulting in a final thickness of 30μm. The samples were prebaked at 95^{o}C to remove the solvent. A hot plate was used to prevent skinning[4]. After exposure the samples were postbaked at 65^{o}C for 5 minutes. The samples were then developed in propylene glycol methyl ether acetate (PGMEA) overnight. In order to prevent the collapse of the structure, due to surface tension forces associated with the process of drying, supercritical drying was performed. The developer solution was exchanged with liquid CO_2. The liquid CO_2 was then converted into its supercritical state by heating and pressurizing it above the supercritical point (1070

[3]For an intensity profile I we define contrast as being $C = \frac{\Delta I}{I_{avg}}$

[4]While baking photoresists convection ovens are typically preferred due to the uniformity of temperature. However in the case of the convection oven the sample gets dried from the top. This can result in a phenomena called skinning in which the top portion dries while some solvent remains trapped at the bottom of the film.

psi and 31°C). The pressure was then gradually released while maintaining the temperature, in order to convert the supercritical CO_2 directly into gaseous CO_2, thereby leaving a dry sample, while also ensuring that the sample did not collapse during the drying process. The samples were then analysed using an SEM. The results for the 3-FCC structure and the P are shown in figure 4-7 and figure 4-8 respectively.

Although the SU-8 platform was found to be the easiest to work with while creating templates, it presents a problem from the perspective of further processing. Since SU-8 is a negative photoresist the final template is a highly crosslinked polymer. Removal of the polymer after backfilling thus involves such extreme processing conditions as burning away the polymer or plasma etching. This can result in damage to the template and also limits the materials that can be used for backfilling. An alternative to this is to simply use a positive photoresist platform. Towards this end a commercial photoresist AZ5214 (Clariant Corp.) was employed. However the thickness of the samples that can be made is limited due to two reasons. First, at the wavelength used (532 nm) the photoresist is quite absorptive. Second, during the exposure the beams were found to begin to diffract off the structure that was being written. For thin samples this does not interfere with the writing process but is an issue for thicker samples. The resultant structures are shown in Fig. 4-9

4.3 Purposefully Introduced Defects

The fact that the SU-8 platform supports multiple exposure suggests that additional writing can be done in the same resist. Intentional defects can thus be introduced by the use of two-photon lithography [86]. Fig. 4-10 shows an SEM of a grid of line defects written into the 3-FCC pattern. The "defect" pattern was written into the surface of a film already exposed with the 3-FCC pattern prior to its post-exposure bake. Each line was written by focussing the beam of the writing laser onto the surface of the sample and then translating the sample, thereby resulting in a line of 200μm. The two-photon exposure was done using a femtosecond laser (MIRA - Coherent) with a wavelength of λ =760nm at a power of 9mW and a frequency of

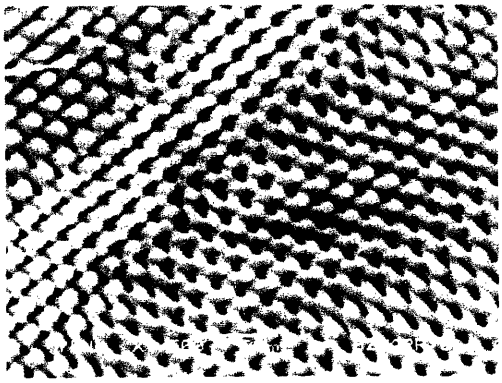

(a) View off the 3 fold axis

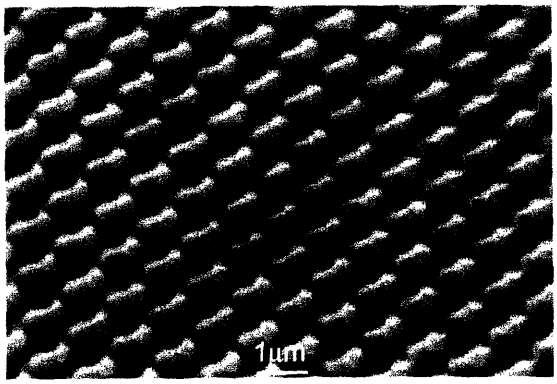

(b) Along the 2 fold axis

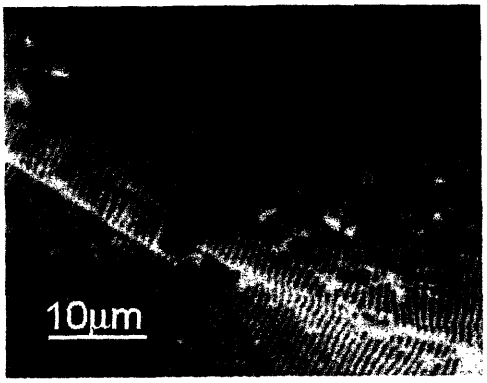

(c) Cross Sectional View

Figure 4-7: SEM of the three term diamond-like structure fabricated by the exposure of the four beam interference pattern in SU-8. Three views are shown.

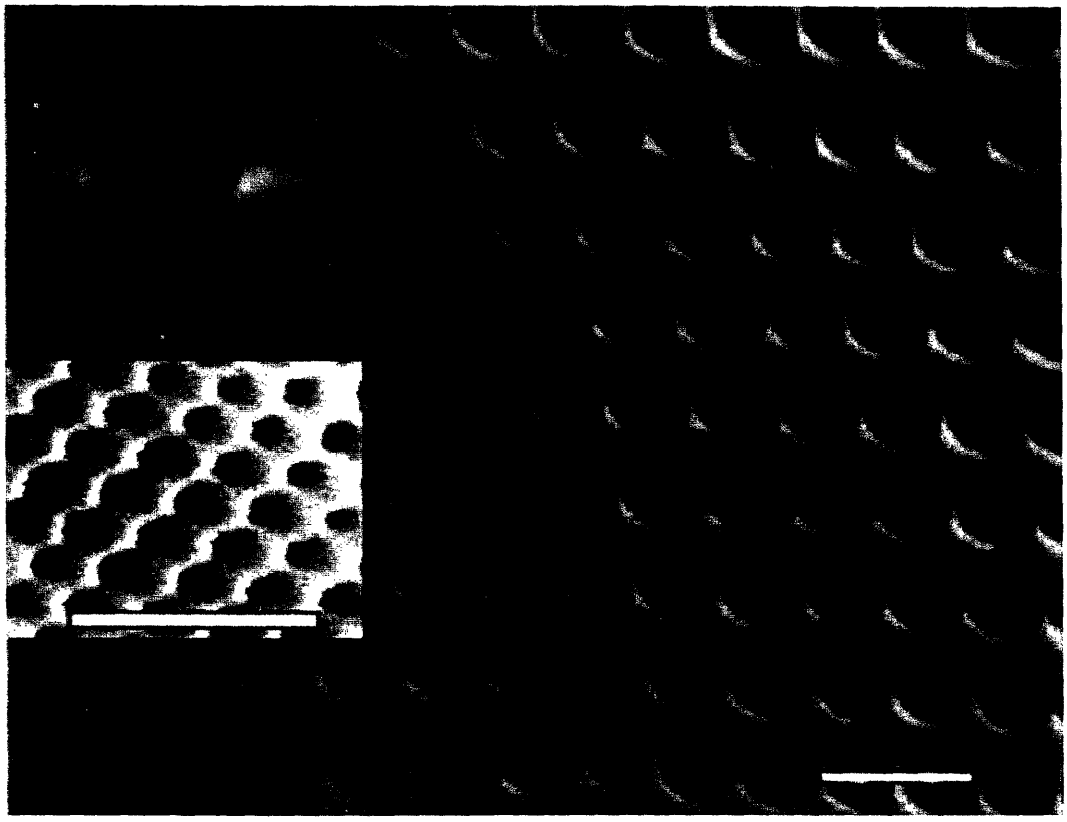

Figure 4-8: SEM micrograph of the (100) surface of a P surface structure having a periodicty of 1.1μ. The inset shows an SEM image of a different sample with the P surface structure having a periodicity of 0.5μ demonstrating the size scalability of the technique. The inset diffraction pattern is from another P surface structure showing the (111) orientation. Both scale bars shown are 2μ.

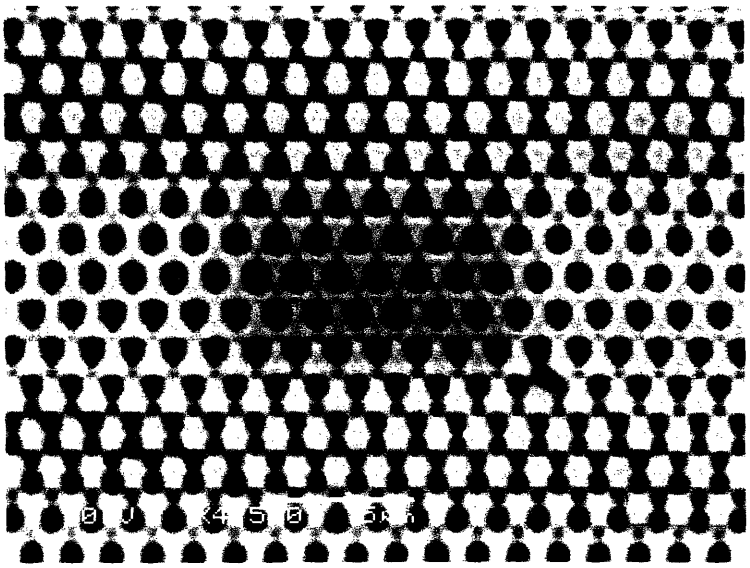

(a)

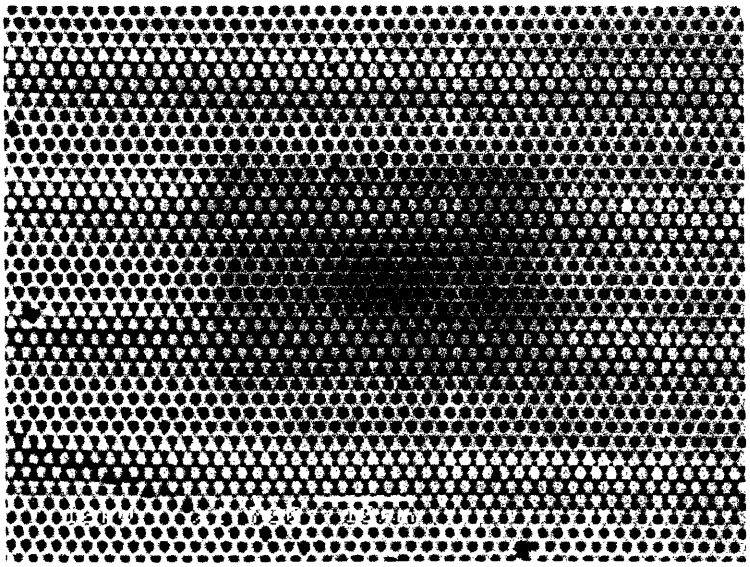

(b)

Figure 4-9: 3-FCC pattern transfered into a positive photoresist - AZ5214. The terracing present in the structure is caused by the substrate being at a slight angle to the [111] plane created by the incoming beams. Each terrace represents a different cut through the unit cell.

0.3khz.

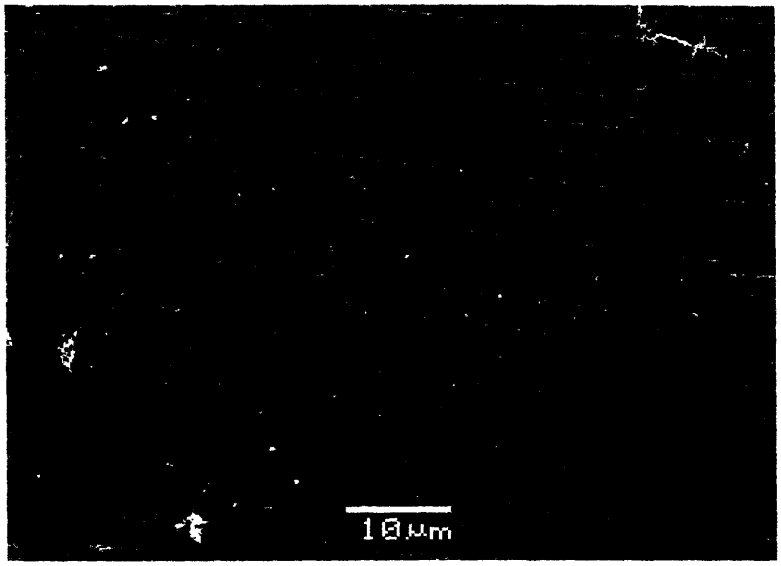

(a)

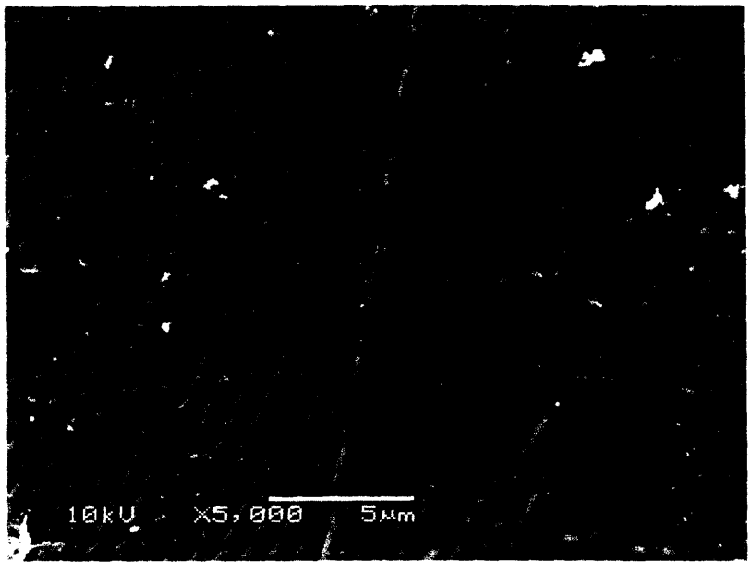

(b)

Figure 4-10: Introduction of a square grid defect pattern into a 3-FCC structure via two-photon lithography

Chapter 5

2-D Interference Lithography Patterns as Hypersonic Phononic Crystals

The technique of holographic interference lithography essentially uses the wave nature of light to create periodic patterns. While clearly the primary interest is in their potential use as photonic crystals it should be obvious that these structures should lend themselves to studies of other wave based phenomena. One such class of wave based phenomena are phonons. As described in section 1.1.4, the fundamental property of phononic crystals is the existence of special frequency regions, so called phononic band gaps, where no mechanical wave can propagate. From the point of view of phononic crystals, the size scale and the large area of the single crystalline samples produced by interference lithography is of interest. In this chapter we examine the use of hypersonic phononic crystals to control the propagation of high frequency phonons. We fabricate high quality, single crystalline hypersonic crystals using interference lithography and show that direct measurement of their phononic band structure is possible with Brillouin light scattering.[1]

[1]The primary results of this chapter have been reported in [87]

5.1 Hypersonic Phononic Crystals

Much of the attention since the first suggestion of the existence of phononic band gaps[7] has been focussed on longer wavelength regimes such as the sonic (10^2-10^3 Hz) and ultrasonic (10^4-10^6 Hz) regimes [88, 89, 90, 91]. The interest in these regimes has been partially due to the promise of applications in acoustics, remote sensing and medical diagnostics, but also because of experimental convenience. Fabricating such phononic crystals is easier given the lengthscales that are involved - elements of these crystals are macroscopic objects that can be manually assembled into the relevant structures [89]. Further, characterizing the band gaps presented by these structures can be done by simple ultrasonic transmittivity measurements.

Hypersonic crystals (10^9-10^{12} Hz) are more difficult to fabricate and characterize because of their inherently smaller length scale. In the past, there have been very few investigations of hypersonic crystals. However, such materials influence high energy phonons in a novel and powerful way, which opens a pathway for exploration of entirely new phenomena. First, the presence of phononic band gaps perturbs the phononic density of states, which impacts physical quantities such as thermal conductivity and heat capacity [92]. Second, since the lattice spacing of hypersonic crystals is comparable to the wavelength of light, they exhibit both phononic and photonic band gaps. Acousto-optical interactions result in intriguing effects, such as optical cooling [93], and shock-wave-mediated light frequency shifts [94].

5.2 Fabrication of 2D Hypersonic Phononic Crystals

2D hypersonic phononic crystals were fabricated using interference lithography and it was demonstrated that the propagation of high frequency hypersonic phonons can be controlled by this technique. This was done by the direct measurement of the phononic band structure via Brillouin light scattering (BLS)[2]. Numerical calculations

[2]BLS measurements were made by Taras Gorishnyy

were employed to explain the nature of the observed propagation modes[3].

Samples were fabricated using the modified SU-8 platform described in chapter 4. Hν-535 was used as the photosensitizer. 0.25g of hν-535, 0.625g of CD1012, 2.5g of SU-8 and 1.35μl of TEA were dissolved in 10g of THF. The solution was spun cast on pre-cleaned glass at 500 rpm, which after polymerisation gave films that were 6μm thick. The samples were prebaked at 65°C for 30 minutes. The beam setup consisted of three equal intensity beams which were distributed symmetrically around, and made an equal angle with, the normal to the substrate. The polarisations were such that each electric field was perpendicular to the difference of the wave vectors between the remaining beams. The samples were exposed to a total power of 1.5W for approximately 1.8s. The samples were then postbaked in a convective oven at 65°C for half an hour. They were developed overnight in PGMEA. Unlike the submicron structures described in chapter 4, supercritical CO_2 drying was found to be unnecessary for this size scale. The resultant samples consisted of triangular arrays of cylindrical holes in an epoxy matrix. The finished sample radius was approximately 2 mm. Two samples were analyzed: s1 with a cylinder radius to lattice constant ratio of r/a=0.1 (4% porosity), and s2 with r/a=0.33 (39% porosity). The lattice constant for both samples is a=1360 nm. The SEM images are shown in Figs. 5-1(a) and 5-1(b), respectively. The normal incidence transmission light diffraction pattern shown in fig. 5-1(c) confirms single crystallinity and the hexagonal symmetry of the structure.

5.3 Probing Phononic Modes with Brillouin Light Scattering

In order to characterize the propagation modes in the two dimensional structures the technique of Brillouin Light Scattering was used. This technique has been used to study the acoustic properties of inhomogeneous polycrystalline bulk materials, such as systems of colloidal particles [95], concentrated ordered solutions of high molecular

[3]FEM calculations were done by Martin Maldovan

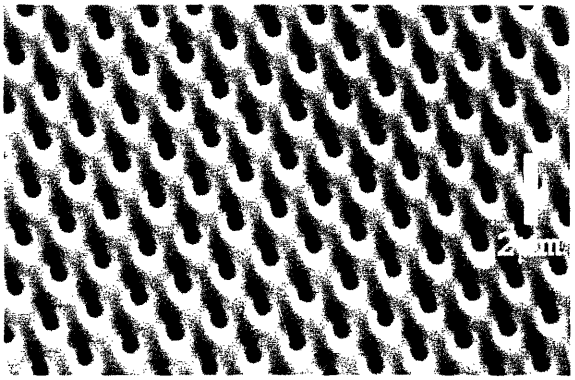

(a)

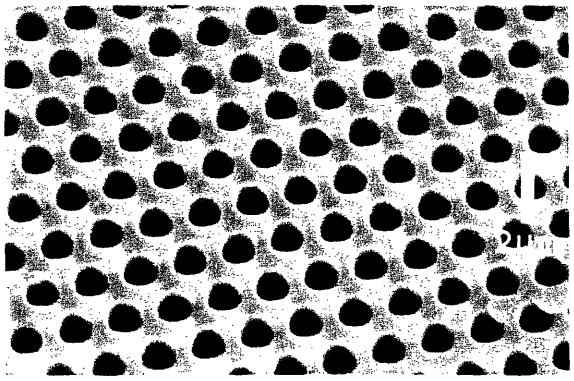

(b)

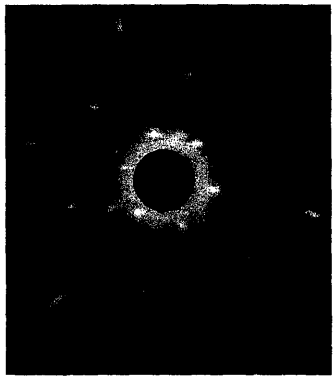

(c)

Figure 5-1: SEM images of interference lithography patterned samples. (a) s1 with r/a=0.1. (b) s2 with r/a=0.33. (c) laser light diffraction pattern.

weight block copolymers [96, 97] and lithographically patterned polymer nanostructures [98]. BLS provides a way to characterize elastic waves by measuring the direction and shift in frequency of inelastically scattered light. The setup employed was a high resolution, angle-resolved, polarized Brillouin light scattering (BLS) system, whose measurement geometry is depicted in Fig. 5-2(a). Photons with the wave vector $\overrightarrow{\mathbf{q_i}}$ enter the sample, where they are scattered inelastically by thermal phonons, such that their wave vector becomes $\overrightarrow{\mathbf{q_s}}$. A typical intensity profile consists of a very strong elastic Rayleigh peak at $\omega = 0$ and a series of symmetric Brillouin doublets at $\pm\omega$ that correspond to Stokes and anti-Stokes scattering, depending on whether a phonon is absorbed or emitted by the scattered light. The polarization of the incident and scattered light was maintained perpendicular to the scattering plane (s-polarized) by a pair of polarizers. The orientation of the sample was adjusted in such a way that the phonon wave vector $\overrightarrow{\mathbf{k}}$ always lay in the sample plane, [Fig.5-2(a)]. Increasing values of $\overrightarrow{\mathbf{k}}$ were probed by scanning along increasing values of the scattering angle θ. Further, the sample was scanned in only one direction, i.e. the $\Gamma - M$ direction, first by aligning the sample by diffraction and then keeping the orientation angle ϕ, shown in fig. 5-2(b), constant . The light frequency shift (equal to the phonon frequency) was measured using a tandem Fabry-Perot interferometer as a spectrum analyzer. The smallest detectable frequency shift is determined by the wings of the Rayleigh peak and by the intensity of the Brillouin doublet. In our case, it was roughly 1 GHz for the stronger glass substrate peaks and 1.5 GHz for the weaker epoxy film peaks. An example spectrum is shown in fig.5-3(b).

The effect of periodicity on the phonon propagation can be seen by comparing spectra of the s1 sample with that of the unpatterned photoresist film, for the same value of $\overrightarrow{\mathbf{k}}$ (in this case $\overrightarrow{\mathbf{k}}$=0.0051nm^{-1}). Both spectra are shown in fig5-3. Two peaks are present in the spectrum of the unpatterned sample: a high intensity peak (1) at $\omega = 4.74$ GHz coming from the glass substrate, and a less intense peak (2) at $\omega = 2.34$ GHz that corresponds to the longitudinal phonon of the polymer film. The spectrum of s1 is more complex. In addition to the most intense glass peak (1) at the same frequency, we see three less intense peaks, labeled (2), (3) and (4), coming

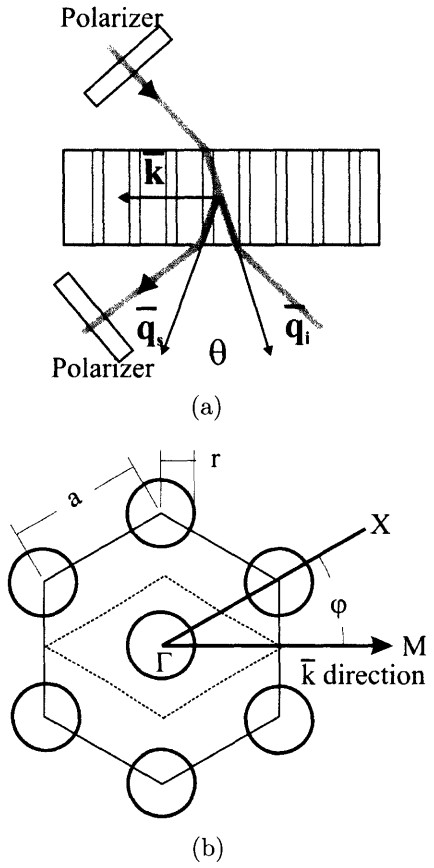

Figure 5-2: BLS measurement geometry. (a) scattering plane, side view. (b) sample plane, top view. Only phonons with k vectors essentially in the sample plane are probed. The dotted line is the Weigner-Seitz cell

from various bands of the phononic crystal. The frequency of the lowest frequency longitudinal phonon peak (2) is shifted slightly from $\omega = 2.34$ GHz to $\omega = 2.39$ GHz, in comparison with the corresponding peak (2) of the unpatterned film. This shift can be attributed to the decrease in the effective sound velocity in the porous polymer structure of sample s1 (4% porosity). The two new peaks (3) and (4) correspond to the propagation states in the higher bands of the phononic crystal. A band diagram along the $\Gamma - M$ direction is obtained by repeating the measurements for $|\overrightarrow{\mathbf{k}}|$ from 0.0005 nm^{-1} to 0.009 nm^{-1}.

5.4 Theoretical Analysis and modeling via the Finite Element Method

Before we examine the experimental $\omega(\overrightarrow{\mathbf{k}})$ relations it is useful to understand what we expect to see. To provide an interpretation of the observed modes we calculate the theoretical band diagrams and and subsequently compare them with the experimental data. The finite element method (FEM), based on the weighted residual formulation [99], is employed to model the properties of the elastic structures. The FEM transforms the elastic wave equation

$$\rho\frac{\partial^2 u_i}{\partial t^2} = \nabla\cdot(\rho c_t^2\nabla u_i) + \nabla\cdot(\rho c_t^2\frac{\partial\overrightarrow{u}}{\partial x_i}) + \frac{\partial}{\partial x_i}[(\rho c_l^2 - 2\rho c_t^2)\nabla\cdot\overrightarrow{u}] \tag{5.1}$$

into a discrete generalized eigenvalue problem, where $\overrightarrow{\mathbf{u}}$ is the displacement vector field, ρ is the density, and c_t, c_l are the transverse and longitudinal velocities respectively. Due to the periodicity of the structure, the displacement field $\overrightarrow{\mathbf{u}}$ satisfies Bloch's theorem. The discrete wave equation together with the enforcement of appropriate boundary conditions, allow the use of numerical algorithms to calculate the fundamental dispersion relation $\omega(\overrightarrow{k})$ for each wave vector $\overrightarrow{\mathbf{k}}$. This finite element approach has also recently been used successfully in the modeling of the electromagnetic wave equation [99]. The interior air region is modeled using zero-traction boundary conditions at the air-material interface [100]. The background was taken to be epoxy

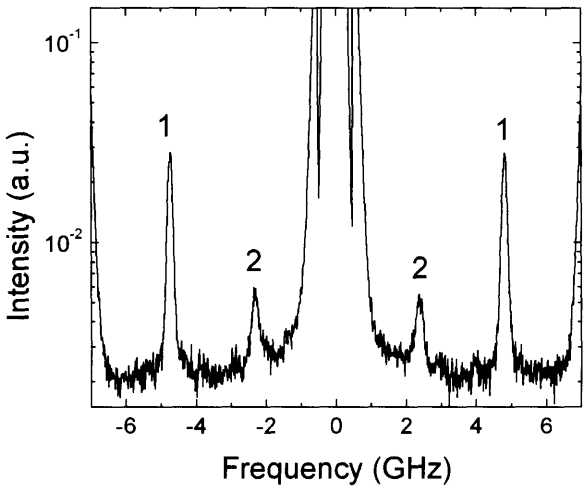

(a)

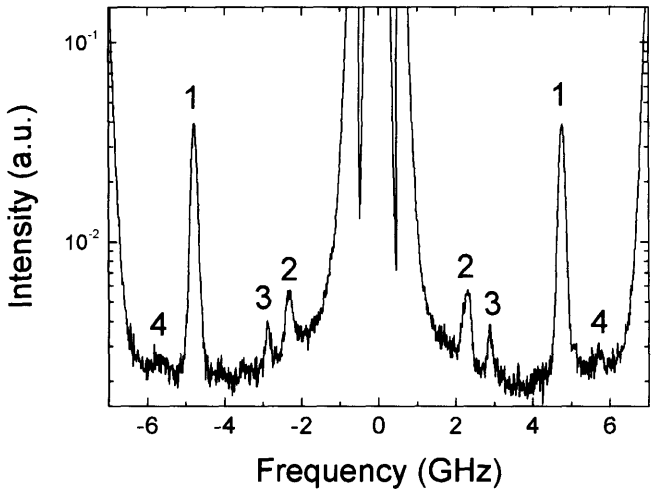

(b)

Figure 5-3: BLS spectrum of the samples at k=0.0051nm^{-1}. (a) unpatterned epoxy film on glass substrate. (b) s1 film on glass substrate.

with ρ=1.19 g/cm^3, c_t=1.8 km/s, and c_l=3.1 km/s. The values of the sound velocity were obtained experimentally from the BLS measurement of the unpatterned film. Figures 5-4(a) and 5-4(b) show the calculated dispersion relationship for in-plane propagation, where the displacement field $\vec{\mathbf{u}}$ is normal to the axis of the cylinders for sample s1 and s2, respectively.

In order to be able to analyze the scattering data it is important to understand the nature of the propagation modes in periodic structures. In homogeneous, isotropic media there are three independent propagation modes: longitudinal (P) waves with $\vec{\mathbf{u}} \parallel \vec{\mathbf{k}}$ and two polarizations (SV (in-plane) and SH (out-of-plane)) of transverse waves with $\vec{\mathbf{u}} \perp \vec{\mathbf{k}}$. Longitudinal and transverse waves are completely independent of each other and propagate at different velocities c_l and c_t. In contrast, in phononic crystals longitudinal and transverse waves are coupled together, such that the propagation modes are generally mixed waves with $\vec{\mathbf{u}}$ neither completely parallel nor perpendicular to $\vec{\mathbf{k}}$.

To visualize the differences among various propagation modes we compute and compare their displacement fields [Figs.5-5(a) and 5-5(b)]. For lower-lying modes, the modes tend to be more "pure", that is $\vec{\mathbf{u}}$ is essentially either parallel or perpendicular to $\vec{\mathbf{k}}$. We, therefore, use the terms "quasi longitudinal waves" and "quasi transverse waves" to describe these modes and represent these modes in the theoretical band diagrams (fig. 5-4) as solid and dashed lines respectively. In contrast, higher band propagation modes are typically strongly mixed and cannot be approximated as either longitudinal or transverse waves. These bands are plotted as dotted lines. It can also be seen that the same band can have a predominantly longitudinal displacement field for one range of $\vec{\mathbf{k}}$ and a strongly mixed displacement field for another range of $\vec{\mathbf{k}}$. This can be understood as an effect of the introduction of periodicity. When there is no pattern present the modes are straight lines and cross each other, one going say up from left to right, and the other going up from right to left. As a periodicity is introduced diffraction starts occurring at these points of intersection, similar to what one expects to see in semiconductor band diagrams, and the bands bend away from the crossing point. The upper band is now made up of two portions with different

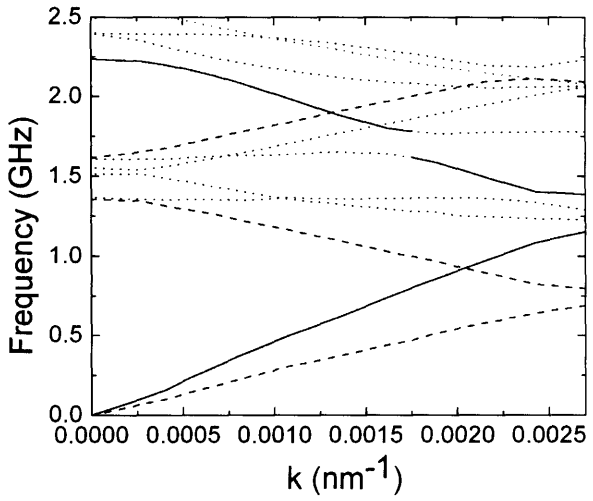

(a)

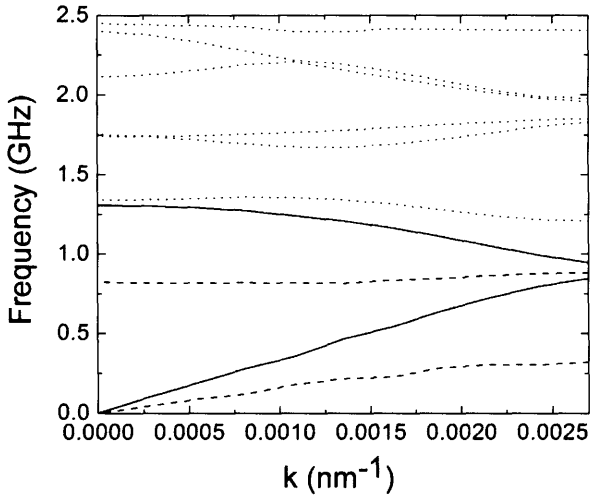

(b)

Figure 5-4: Theoretical band diagrams for s1 and s2 samples. Solid lines represent quasi longitudinal modes, dashed line quasi transverse modes, dotted lines mixed modes.

fundamental origins. If one portion has a fundamentally mixed mode and the other is a "quasi-mode" then there will be an abrupt change in the nature of the mode for that band for the reason just explained.

In order to be able to correlate the scattering data with the band diagrams it is necessary to identify which of the calculated modes are actually measured experimentally. In order to do this the intensities of the light scattered by different modes are computed. When an elastic wave passes through a material it creates changes in the electrical permittivity due to elastic deformation. Following the treatment by Landau [101],

$$\vec{\mathbf{E}}_s \propto (\vec{\mathbf{n}} \times (\vec{\mathbf{n}} \times \vec{\mathbf{G}})) \tag{5.2}$$

where $\vec{\mathbf{E}}_s$ is the electric field in the scattered wave, $\vec{\mathbf{n}}$ is a unit vector in the scattering direction, and the components of the vector $\vec{\mathbf{G}}$ are given by

$$G_i = \int \delta\epsilon_{ik} e^{-\imath \vec{\mathbf{k}} \cdot \vec{\mathbf{r}}} dV \cdot \vec{\mathbf{e}} \tag{5.3}$$

Here $\vec{\mathbf{e}}$ is a unit vector parallel to the incident electric field vector $\vec{\mathbf{E}}_i$, which is represented by

$$\vec{\mathbf{E}}_i = \vec{\mathbf{e}} E_0 e^{(\imath \vec{\mathbf{q}} \cdot \vec{\mathbf{r}})} \tag{5.4}$$

$\delta\epsilon_{ik}$ is the change in the electrical permittivity due to elastic deformation and is determined by the equation

$$\delta\epsilon_{ik} = a_1 u_{ik} + a_2 u_{ll} \delta_{ik} \tag{5.5}$$

where a_1 and a_2 are the photoelastic constants of the medium and u_{ik} is a strain tensor specified by

$$u_{ik} = \frac{\partial u_i}{\partial x_k} + \frac{\partial u_k}{\partial x_i} \tag{5.6}$$

The integration for Eqn.5.3 is done over the scattering volume. In case of a

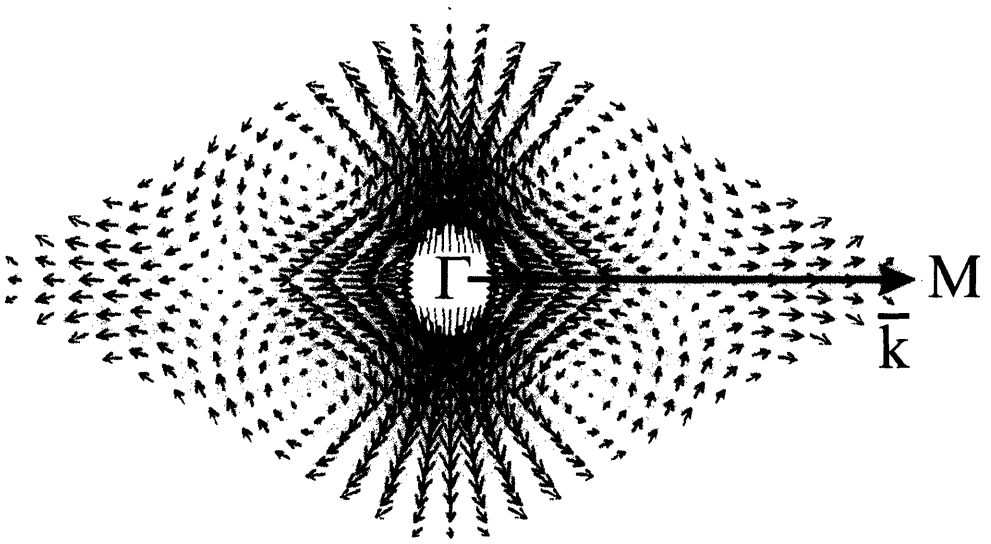

(a)

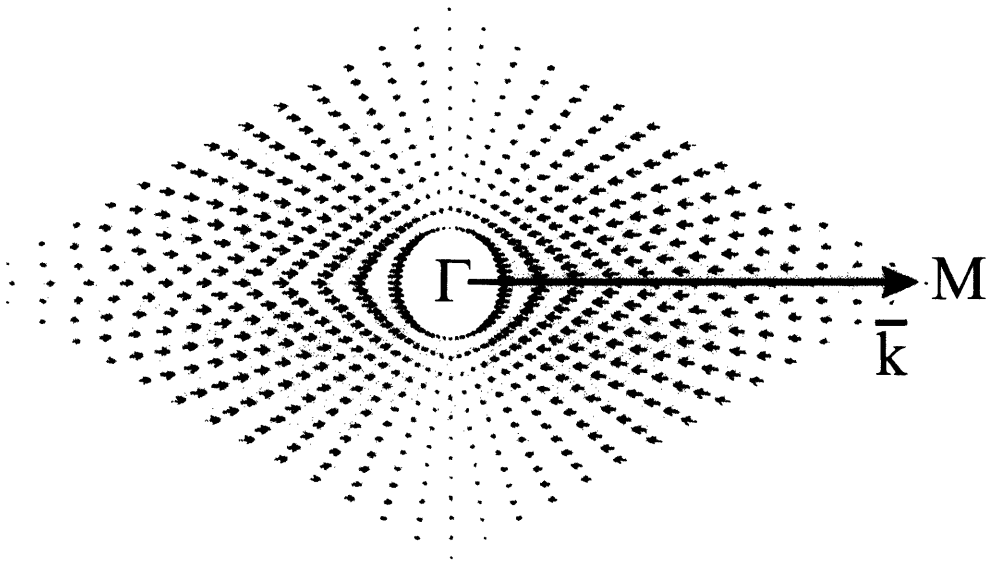

(b)

Figure 5-5: Displacement field for mixed (k = 0.0027 nm^{-1}, ω =1.16 GHz) and quasi-longitudinal (k =0.0027 nm^{-1}, ω=1.79 GHz) modes for s1 sample.

plane wave propagating in a homogeneous medium, the integral can be evaluated analytically. Thus, assuming a homogeneous sample with the scattering geometry depicted in Fig.5-2(a) it can be noted that: (1) SV modes do not scatter light; (2) light scattered by SH modes are p-polarized; (3) light scattered by P modes are s-polarized. Therefore, only the signal from longitudinal phonons will be measured.

In the case of phononic crystals, the displacement fields cannot be represented by plane waves and the integral for $\vec{\mathbf{G}}$ must be evaluated numerically. However, the conclusions above still provide useful guidelines for the interpretation of the measured spectra. In particular, in the present experimental configuration, it is clear that quasi longitudinal phonons will scatter light significantly, while contributions from the quasi transverse modes will not be detected. The intensity of the mixed modes peaks will depend on their field distributions and must be evaluated separately for each mode. However, their strength will be less than the quasi longitudinal phonons peaks. For this reason, the low frequency peak (2) in the s1 spectrum of fig. 5-3(b) is more intense than peaks (3) and, especially, (4).

5.5 Phononic Band Diagrams

Figures 5-6(a) and 5-6(b) superpose experimental data points and the theoretical lines on the same graphs. Only quasi longitudinal modes (solid lines) and strongly scattering mixed modes (dotted lines) are plotted. The spectrum of sample s1 has contributions from the second quasi longitudinal mode, while the first quasi longitudinal mode is at frequencies too low to be detected. In addition, the signature of the strongly scattering mixed modes can be seen at higher frequencies. The spectrum from sample s2 is very different. Due to the higher porosity, the effective sound velocity decrease is so prominent that both the first and second quasi longitudinal modes are below the detection threshold. All the higher modes are mixed. Experimental data points follow the calculated lines well, but in some places along the theoretical lines expected experimental data points appear missing. This behavior is not surprising. The scattering from the mixed modes is $\vec{\mathbf{k}}$ dependent and relatively

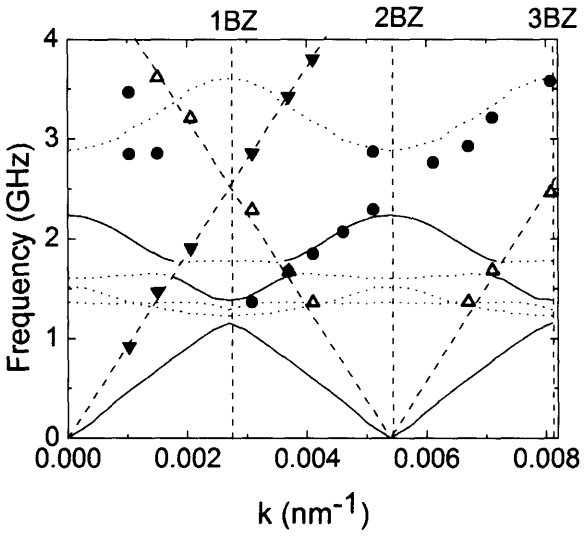

(a)

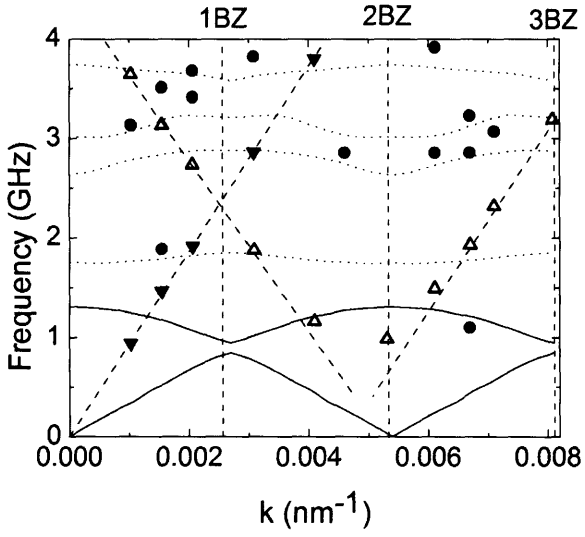

(b)

Figure 5-6: Experimental and theoretical phononic band diagrams for s1 and s2 samples respectively. Closed triangles glass mode, open triangles Bragg mode, closed circles phononic crystal modes, solid lines theoretical quasi longitudinal modes, dotted lines theoretical mixed modes.

weak. Therefore, for some values of $\overrightarrow{\mathbf{k}}$ it may be impossible to detect peaks even after long accumulation times. Finally, there is one mode in both s1 and s2 spectra that does not follow any theoretical line. It is labeled as a "Bragg mode" [97, 96] and is plotted with open triangles. To speculate on the nature of this mode, it is worth noting that its velocity is nearly equal to the glass sound velocity, while its negative dispersion is a characteristic of crystalline samples [97]. In fact, the two crossing points of these three branches hit the k of the first and the second BZ. These observations strongly suggest that this mode represents a wave propagating at the epoxy film-glass substrate interface.

It was thus demonstrated that a combination of interference lithography and Brillouin light scattering constitutes a complete experimental tool set for fabrication and characterization of hypersonic phononic crystals. A variety of single crystalline, defect free structures were created and their phononic band diagrams measured directly. FE modelling was employed to perform theoretical band structure calculations to obtain a very good agreement with the experimental results using no fitting parameters. Thus interference lithography could be used in the experimental study of hypersonic phononic crystals and opens a new pathway towards achieving control over phononic properties of materials.

Chapter 6

Biomimetic Microlens Arrays through Interference Lithography

So far we have primarily exploited the interaction of periodic materials patterned by interference lithography patterns with wave based phenomena such as light and mechanical waves. Here we utilize another aspect of the patterns that result from holographic interference lithography. The structures that are created are porous and thus could lend themselves to mass transport. In addition, the light interference field created is spatially varying which can be translated into a spatial variation in density or height of a material. It has been demonstrated that 2D interference patterns could be used as lens arrays albeit on the scale of 50-200μm[102]. Inspired by a biological prototype, a highly efficient optical element formed by brittlestars[103], the concepts of porous structures and lens arrays were combined to create bio-inspired microlens arrays with integrated pores on the submicron scale[1]. The lenses are shown to have strong focussing abilities and the ability to have light-absorbing liquids transported in and out of the pores. The light field from the lenses is also modelled by treating them as simple diffraction limited lenses.

[1]The primary results of this chapter have been reported in [104]. The bulk of this collaborative work was done by S. Yang and J. Aizenberg at Bell Labs

6.1 Biological Microlens Arrays

Natural optical systems, whose hierarchical architecture and hybrid character offer outstanding optical properties and enable multi-faceted roles [105, 106, 107, 103, 108, 109, 110]. Of specific interest is an example of a biologically produced adaptive optical system comprised of a close-set, nearly hexagonal array of uniform microlenses. This device occurs in a light-sensitive brittlestar, Ophiocoma wendtii, shown in Fig. 6-1 [103]. The lenses were shown to be involved in photoreception as optical elements that guide and concentrate light onto photosensitive tissue and offer remarkable focusing ability, angular selectivity and signal enhancement. An interesting design feature of this bio-optical structure is the presence of a pore network surrounding the lenses, which is essential to the diurnal migration of pigment-filled chromatophore cells [111] i.e. these chromatophores regulate the amount of light reaching the lenses by extending their pigment filled processes to cover the lens during the day and retracting them into a lateral position during the night. Due to the presence of the pore network, the brittlestar microlenses can be considered as an adaptive optical device that exhibits a wide-range transmission tunability achieved by controlled transport of radiation-absorbing intracellular particles. Other functions of the chromatocyte pigment include diaphragm action, numerical aperture tunability, wavelength selectivity, minimization of the cross-talk between the lenses, and improved angular selectivity.

6.2 Fabrication of Microlens Arrays with Integrated Pores via Holographic Interference Lithography

The creation of complex and small photonic devices that can mimic the unusual design of the brittlestar optical elements and their consequent outstanding optical properties, would require the creation of a structure that combines microlens arrays with the porous surrounding microfluidic system. The fabrication of such a structure using

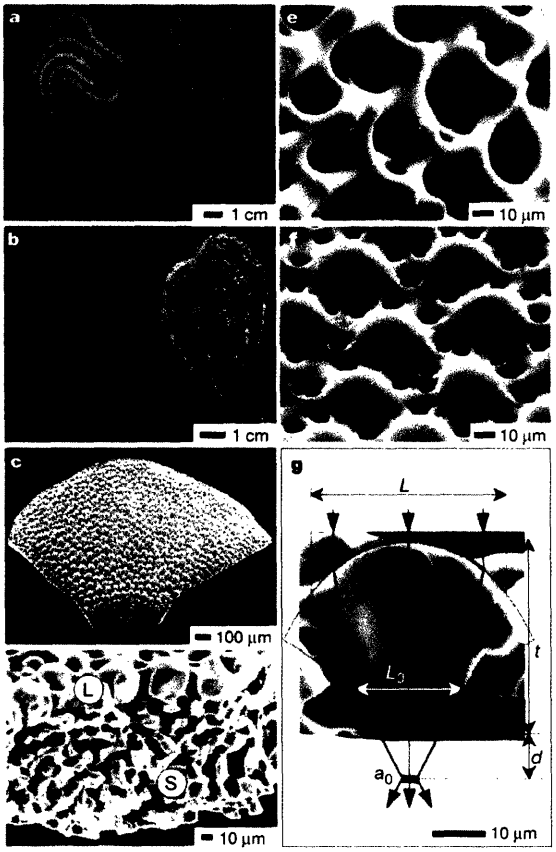

Figure 6-1: Appearance and skeletal structure of ophiocomid brittlestars. a, Light-indifferent species Ophiocoma pumila shows no colour change from day (left) to night (right). b, Light-sensitive species O. wendtii changes colour markedly from day (left) to night (right). c, Scanning electron micrograph (SEM) of a dorsal arm plate (DAP) of O. wendtii cleansed of organic tissue. d, SEM of the cross-section of a fractured DAP from O. wendtii showing the typical calcitic stereom (S) and the enlarged lens structures (L) that constitute the peripheral layer. e, SEM of the peripheral layer of a DAP of O. pumila showing that it lacks the enlarged lens structures. f, SEM of the peripheral layer of a DAP from O. wendtii with the enlarged lens structures. g, High-magnification SEM of the cross-section of an individual lens in O. wendtii. Red lines represent the calculated profile of a lens compensated for spherical aberration. The operational part of the calcitic lens (L0) closely matches the profile of the compensated lens (bold red lines). The light paths are shown in blue. Figure is reproduced from [103].

existing techniques such as inkjet printing[112], melting of patterned photoresists [113], reactive ion etching of silica and silicon [114], soft-lithography [115], or self-assembly of monodispersed polymer beads [116] is, however, not straightforward. Most of these techniques only create lenses without pore structures and their optical properties are not tunable. Here the marked similarity between 2d structures created via interference lithography and the lens structures of O. wendtii.[2] are demonstrated. The lens like action of the interference patterns is demonstrated and also the presence of the pores present in these structures is exploited to move fluids in a manner similar to the movement of pigment in the brittle star stereom. Moreover, as discussed in chapter 2, the symmetry of the resulting structures can be conveniently controlled by the wavevectors and polarizations of the interfering beams. Prior to this work Hutley et al. [102] created microlens arrays using interference beams. In their approach, a pattern with spherical concave depression regions and "chicken-wire focus" (a quasi-cylindrical lens) was first generated from interference of laser beams through three optical lenses. The "chicken-wire focus" was then pattern transferred to a second surface coated with photoresist. This was followed by resist reflow to create hexagonal packed microlens arrays, with lens sizes in the range of 50-200μm, resulting in high fill factors. While this data has demonstrated the feasibility and versatility of using multi-beam interference to create lenses, however, attention has not been paid to the integration of both lenses and pores into a more complex photonic device, nor has the tunablity of lens optical properties been demonstrated.

The 2d biomimetic lens patterns were created in a manner similar to the procedure described in chapter 4. The wave vectors were arranged as: $\vec{\mathbf{k}}_1 = 2\pi/a$ [0.035,0,0.999], $\vec{\mathbf{k}}_2 = 2\pi/a$ [-0.017,0.03,0.999], $\vec{\mathbf{k}}_2 = 2\pi/a$ [-0.017,-0.03,0.999]. The resist was formulated by dissolving 2 wt% of Irgacure 261 (Ciba Specialty Chemicals) and SU8 in cyclopentanone (30-50 wt%). In this case, for the size scale of the pattern created, there was no need for a contrast enhancing agent. The solution was then spin coated on a precleaned glass substrate followed by a soft bake at 90°C to completely remove the solvent. The film thickness was in the range of 5-15 μm depending on the spin

[2]Characterisation of the lens like properties were done by S. Yang at Bell Labs

speed and resist concentration. Exposure was done at 2W for times between 1-6s followed by a postexposure bake at 65°C for half an hour. The film was developed in PGMEA for two hours. It was found to be unnecessary to dry the solvent using supercritical drying.

6.3 Lens Action of 2D Interference Lithography Patterns

The resultant structures were tested for lens-like properties. As before, the wave vectors determine the translational symmetry of the structure, while the polarization vectors are the key to the lens formation and its connectivity. Three polarization configurations were examined. First, the polarizations of each wave were made "parallel" to each other, i.e. their components were minimized in the direction perpendicular to $\vec{\mathbf{k}}_2$-$\vec{\mathbf{k}}_3$ as shown in 6-2d. A periodic variation of light intensity is generated with hexagonal symmetry, and the simulated intensity profile 6-2b resembles the shape of the biological lens array 6-2a. In the other two configurations, shown in fig. 6-3 the polarization of each wave was set to be perpendicular or parallel to the difference between the remaining two wave vectors as shown. In this case we obtained a three-fold connectivity with a very small area of highest intensity, which resulted in lens areas with very small collection areas. The first configuration was thus seen to have the most effective lens effect of the three. Within a particular configuration it was found that when the intensity difference between strongly exposed and adjacent weakly exposed regions is above the threshold, formation of a contour of a lens is introduced. The lens contour may be amplified by factors, such as the quantum efficiency of photosensitive molecules (i.e., sensitizers and photoacid generators), the strong nonlinear relationship between the dose, polymerizability and solubility change of the photoresists, as well as the shrinkage of resist film during drying. The lens size (diameter of 1.5 to 4.5 μm, height of 200 nm to 1.0 μm), shape, symmetry and connectivity can be controlled by adjusting the beam wave vectors and their polarizations, while

the pore size and porosity are determined by the laser intensity and exposure time (porosity of about 10 % to 80 %).

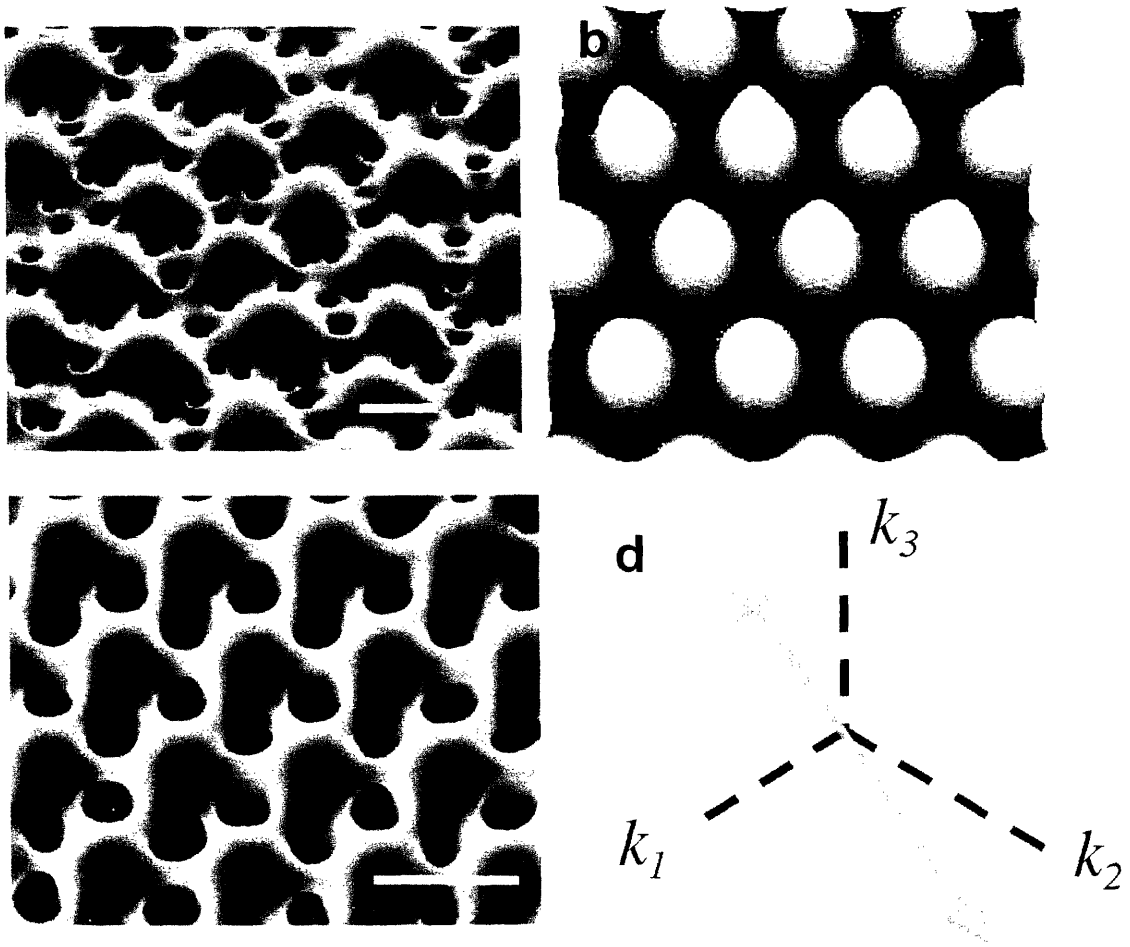

Figure 6-2: Structure of a biological and biomimetic porous microlens arrays. a) Scanning electron micrograph (SEM) of a brittlestar lens design. Scale bar, 50μ. b) Calculated light intensity profile from three-beam interference lithography. Beam wavevectors and polarizations are described in Experimental. c) Corresponding SEM of a synthetic, biomimetic microlens array with integrated pores. Scale bar, 5μ. d). Schematic drawing of the used beam polarizations (shown in double-headed arrows) viewed from direction to realize the biomimetic lens seen in (c).

The ability of the lens-like structures to focus light was studied by lithographic experiments, in which a film of a positive-tone photoresist, AZ5209 (from Clariant Ltd.), was illuminated through a synthetic lens array. A schematic of the experimental setup is shown in fig. 6-4a. Approximately 1μm thick AZ5209 was spun on a glass

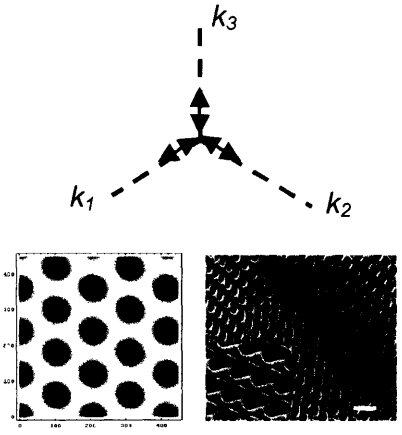

(a)

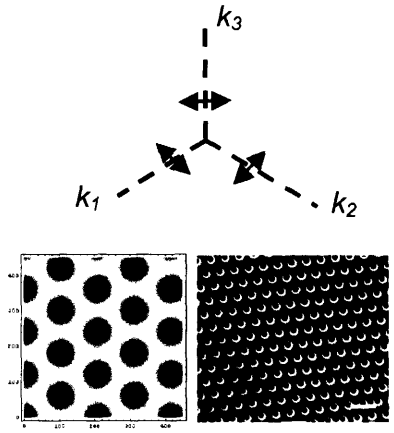

(b)

Figure 6-3: Formation of 2D structures in three-beam interference lithography using another two different configurations of beam polarizations (shown in double-headed arrows) viewed from direction. In each panel, the left image shows the calculated total intensity distribution using the consequent beam polarizations. The brightest region corresponds to the highest intensity of light. When calculating the intensity distribution in different beam polarizations, the change in polarization caused by reflection at the air/photoresist (SU8) interface is taken into account. The right image is the corresponding scanning electron micrograph (SEM) in experiment. An enlarged SEM image is inserted in Figure 2a to better demonstrate a small lens. The scale bar is 5μ.

substrate, followed by casting polydimethylsiloxane (PDMS) with different thickness on top of the resist as a transparent spacer. The lenses attached to glass substrate were then placed directly on the PDMS spacer for conformal contact. When the illumination dose was fixed slightly below the sensitivity threshold of the photoresist (I_0) to avoid the exposure through the pores, the photoresist film appeared to be selectively exposed under each microlens due to their strong focusing activity, showing hexagonally packed holes 6-4b that closely matched the microlens arrays seen in Figure 6-2c. The size of the features in the resist layer, a, can be effectively controlled by placing transparent spacers with different thickness, h, between the lens structure and the resist film. For example, for the lens diameters of 4.1 μm, the feature sizes in the photoresist gradually changed from 3 μm to 700 nm near the focal point (Fig. 6-4c. When the illumination dose was set above the lithographic threshold intensity, under each lens we observed one hole surrounded by another six, which originated from the pores in the lens arrays.

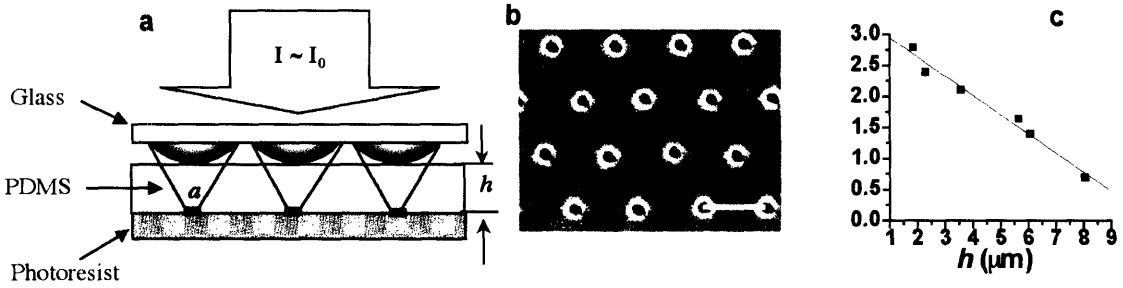

Figure 6-4: Focusing of light by the microlens array. a) Schematic presentation of the experiment. b) SEM of features in a positive-tone photoresist exposed through the lens array near the focal point. Scale bar, 5μ. c) Dependence of the sizes of the produced features, a, on the distance between the array and the photoresist film, h.

The light intensity distribution from the lenses was estimated using simple Fourier optics. The lens was assumed to be diffraction limited at its focus[3]. The light field is thus an Airy ring given by the equation:

$$I = I_0(\frac{2J_1(kaq/h)}{kaq/h})^2 \tag{6.1}$$

[3]this approach was taken on the basis of a useful discussion with J. Walish

where I_0 is the peak intensity at that plane, J_1 is the First Bessel function, commonly used in systems with cylindrical symmetry, k is the modulus of the wave vector of light, a is the radius of the lens, q is the radial distance from the optical axis, and h is the distance along the optical axis, which is the same as the distance between the lens array and the photoresist. Since the light falling on the lens has to be conserved, we normalized the value of I_0 against the intensity of light falling on the lens. Based on the experimental data, the focal length of the lens, f, was set at 8μm, and the diameters of the lens and pores were assumed to be 3 and 1.5μm, respectively. Fig.6-5a shows the calculated light field of the lens from h=f (8μ)m to h=2f (16μm). The light passing through the lens is focussed with the highest intensity at h=f and q=0. The peak intensity is I_0. The pores were assumed to generate a cylindrical light profile, whose peak intensity is determined by the illumination dose. The size of the feature at the focal point can be estimated. Assuming the threshold intensity from the pores in Fig.6-5b to be the cut off intensity for the recording photoresist, the radius of the feature resulting on the photoresist will be 0.4μm (0.8 μm in diameter). This is close to the experimental data of 0.7μm in diameter, considering that the possible inhomogeneities of the lens shape due to the bridges at the pores etc were not take into consideration. The calculated 3D profiles of the light field generated by the photomask for $I < I_{th}$ and $I > I_{th}$ and at different h are shown in Fig.6-5c,d and e.

Another application of the biomimetic microlens array is based on using the porous network as a microfluidic system that mimics the pigment movement in the brittlestar stereom. We studied the possibility of actuating photoactive liquids within the microlens array. The thin film containing the porous microlens arrays (3mm in diameter) was assembled between two copper grids (3.05 mm in diameter, 50 mesh) and sealed with instant epoxy. Two micropipette tips were carefully glued on both sides of the of copper grids and light-absorbing liquid was introduced from one side via a syringe. An adjustable transmission through the lenses (from 100 % to 0 %) was observed depending on the concentration of the dye solution 6-6. These results suggest that by using different liquids (e.g. with selective refractive index and/or including

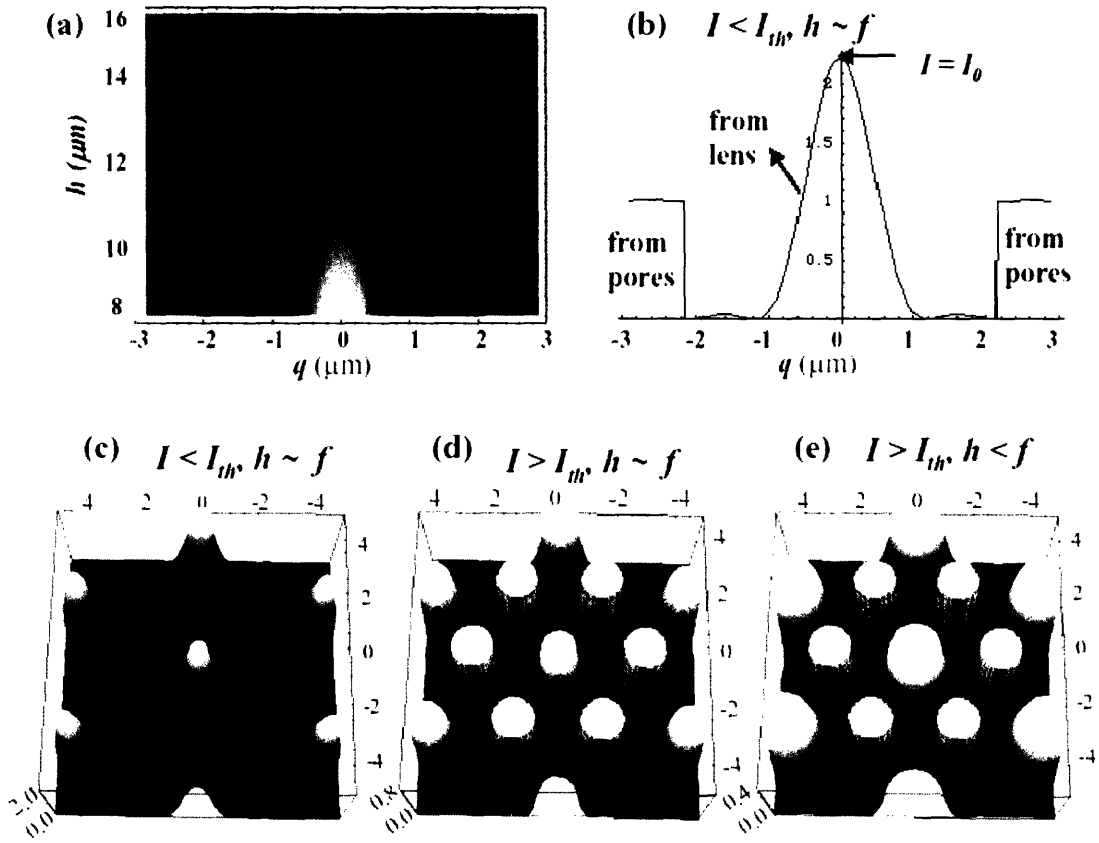

Figure 6-5: Calculated light field profiles generated by the porous microlens array in a lithographic experiment at different illumination doses and distances. a)Light field distribution from a single lens for h=f to h=2f b) Cross section of the field produced by the lens vs. that from the pores for an intensity less than the threshold intensity of the recording photoresist c)-e) 3D light intensity profiles generated for various intensities and positions

dyes that can absorb certain wavelength), a wide range of tunability of the lens optical properties, including varied transmission, numerical aperture and wavelength selectivity, can be achieved.

The fabrication of microlens arrays with integrated pores reported here is a first step towards creating and mimicking complex optical devices that are prominent in biology. The presented optical properties, tunability and application of the synthetic structures clearly demonstrate that the lessons learned from sophisticated microlens arrays evolved by brittlestars for successful survival and adaptation may improve our current capabilities to construct new, adaptive, micro-scale optical devices for a wide variety of technological applications, including tunable photonic packaging, miniature optical sensors, biosensors, photolithography, and military optical systems. The knowledge we gain from fabricating these complex structures will help us create novel hybrid structures with multi-functionalities.

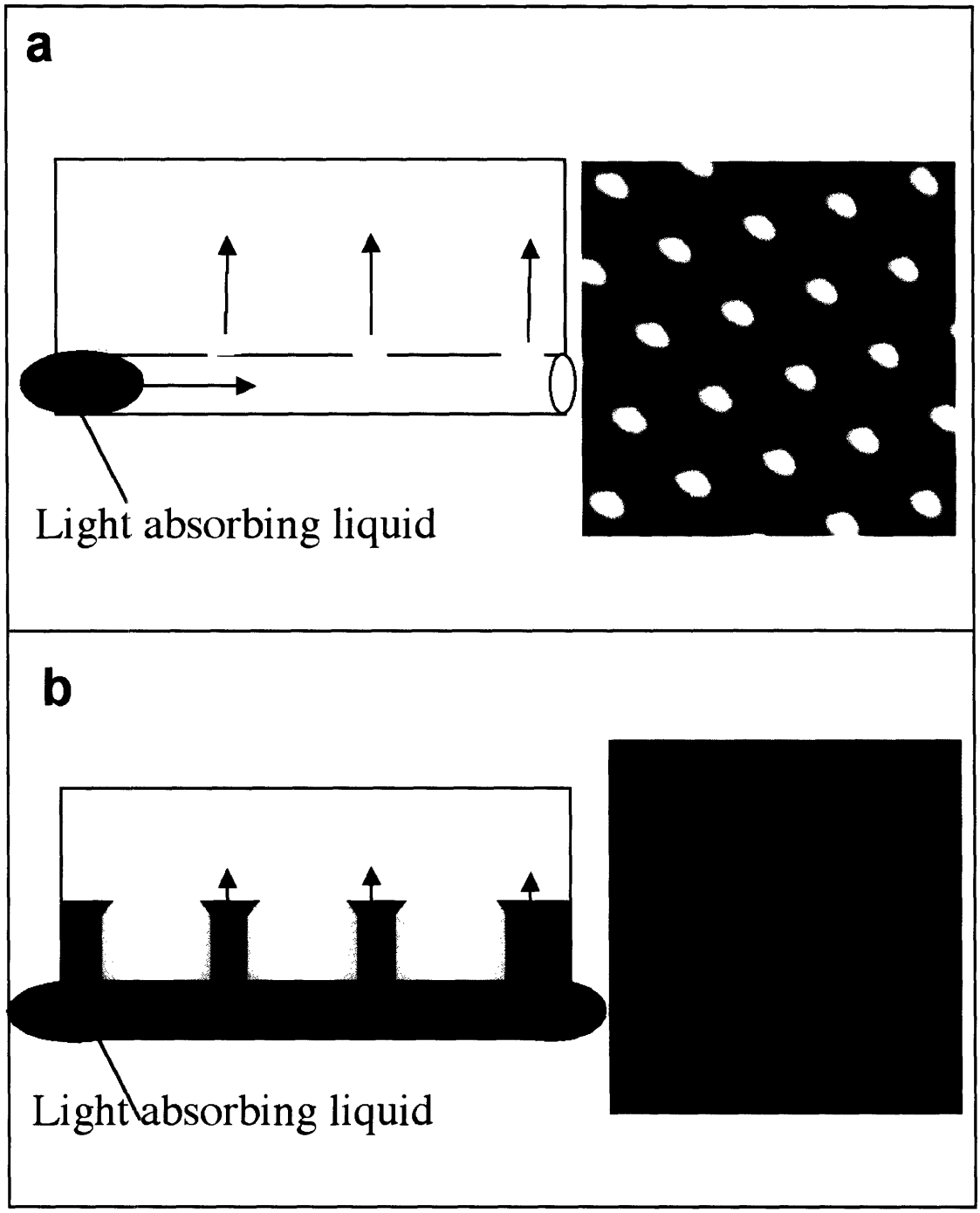

Figure 6-6: Illustration of the transmission tunability through the lens array, using controlled transport of light-absorbing liquid in the channels between the lenses. Light micrographs were recorded in a transmission mode near the focal point: a) without light-absorbing liquid, b) with the light-absorbing liquid between lenses.

Chapter 7

Summary and Future Work

7.1 Summary

In this thesis a simple technique for controlling structure via holographic interference lithography was established and implemented. It is strongly believed that this approach will serve as a powerful tool in a variety of applications, both scientific as well as technological. Photonic crystals, phononic crystals and microlenses in particular have been examined in this thesis.

The fundamental control over resultant structures stems from the application of symmetry principles to the technique of interference lithography. Here we have demonstrated access to various space groups including such important structures as the level set approximations to the Diamond, the Schwartz P structure, the FCC, the BCC-Wrapped Package and the non centrosymmetric Gyroid structures. The ability to make 3D structures over a large area, with low defect densities and periodicities on the subμ scale opens a whole range of opportunities including such diverse areas as photonic crystals, phononic crystals, drug delivery, microtrusses, tissue scaffolds, microfluidics and colloidal crystallization.

Given an ability to dial in a set of symmetries into a three dimensional structure the important question then becomes the choice of elements that will be targeted. We sought to establish a correlation between structure and photonic band gap properties by systematically exploring the 11 FCC space groups. This resulted in a technique to

search for photonic band gap structures. It was found that a fundamental connectivity caused by simple Fourier elements tended to support gaps. 2-3, 5-6 and 8-9 gaps were opened in the f.c.c lattices. The F-RD and 216 structures were newly shown to have complete band gaps.

Since two of the three previously established champion photonic crystal structures, viz. the Diamond and the Gyroid presented practical fabrication challenges, approximations to these structures were proposed. A scalable P structure and the 3-FCC structure were fabricated by single and multiple exposure techniques. Both negative and positive tone photoresist systems were demonstrated. Line defects were written into the negative tone system using two-photon lithography.

The single crystalline, porous nature of the structures was exploited to examine the possibility for their use as hypersonic phononic crystals and microfluidic microlenses. Two dimensional single crystalline patterns were created using interference lithography. Their phononic band structure was probed by Brillioun light scattering to yield a phononic band diagram, which clearly demonstrates the effect of periodicity on the phononic density of states. The ability to control the density of states at these length scales holds the potential for control over thermal properties. The two dimensional structures fabricated in negative photoresist were also tested as microlenses with the integrated pores acting as microfluidic channels. This combination resulted in a structure reminiscent to that of the biological species ophiocoma wendtii, which uses such microlenses and microfluidic channels to sense light and respond with color changes due to radiation absorbing particles.

7.2 Follow Up Work

The demonstration of these 2D and 3D interference structures is a small step in terms of the possibilities that are opened up by the technique of interference lithography. In terms of extending the technique itself an important challenge for the future is to develop an optical setup that will allow for arbitrary and repeatable control over the phase of the interfering beams. Such a development would allow us to write

arbitrary three dimensional structures. Even with the current single exposure four beam setup there are still several important structures which are worth pursuing. Examples are the diamond structure, still the holy grail of photonic crystals, the non centrosymmetric gyroid structure which could have implications, and the BCC-wrapped package, which has the property of suppporting all angle negative refraction at a sufficiently high dielectric contrast[117].

Another important front is that of the materials systems used in this method. Currently the epoxy based SU-8 material system is the most extensively used. It would be useful to have a material system that can be removed easily during the templating process while also displaying other properties such as mechanical robustness, the ability to form thick films, and to exhibit a low refractive index and low absorption profile. The development of a scheme to infiltrate these templates with an appropriate material is also an important near term goal from the perspective of several properties including photonic, phononic and mechanical. This could vary from simple backfilling with an appropriate polymeric material to CVD of high refractive index semiconductors.

7.3 New Ventures

The periodic structures described in this thesis possess several key properties: they are single crystalline over large areas, their symmetries can be controlled, and they are porous and bicontinuous. Each of these features can be exploited. Here a brief listing is presented of potential avenues of research interest, some of which have been touched upon in Chapter 1.

- Biological Scaffolds: This was discussed in section 1.1.5. A recurring theme in biological systems is the need for three dimensional constructs that possess both mechanical integrity as well as connected pores that would support mass transport. We could thus envision using these 3d structures as tissue scaffolds, or drug delivery scaffolds that demonstrate "bulk-erosion" like properties while still possessing constant release profiles. The single crystalline nature of these

constructs could also prove useful for basic studies in biology such as studies of changes in cell growth due to mechanical changes.

- MultiFunctional Microtrusses: The idea of using these 3d structures as microtrusses has been touched upon in section 1.1.3. Apart from their potentially intruiging mechanical properties an important additional aspect of these microtrusses is that they can support mass transport. We could thus potentially envision using these structures as microtrusses that also afford heat exchange or mass transport of chemical species across the mechanical barrier they provide.

- Optimised Composites: Examined in section 1.1.2

- Mixers and Sorting for Microfluidics: The motion of microscopic dielectric objects can be profoundly affected by the presence of an applied light field. It has been demonstrated that three dimensional light fields can act as microfluidic sorters both on the basis of size and refractive index [118]. The ability to control the symmtries of the applied light fields could have important implications for this sorting technique. Another potential avenue of interest from the perspective of microfluidics is that of mixers. The bicontinuous structures can perform the function of spoilers to promote mixing in microreactors or nanoporous filter elements[119]

- Templates for Colloidal Crystal Growth: It has been demonstrated that dielectric particles can be trapped and be induced to form colloidal crystals in the presence of spatially varying light intensities[57]. The results of this thesis could thus be applied to create symmetries that might otherwise be difficult to access via simple colloidal crystallisation technique.

- Nanoporous Structures: Most of the experimental work in this thesis dealt with the use of 532nm light to create the periodic patterns. The use of shorter wavelengths would result in structures with even smaller periodicities, resulting in feature sizes on the scale of tens of nanometers. The resultant nanoporous

structures could find application in such fields as catalyst supports and the study of biological species such as proteins in confined spaces.

Bibliography

[1] E. Yablonovitch. Inhibited spontaneous emission in in solid-state physics and electronics. *Physical Review Letters*, 58(20):2059–2062, May 1987.

[2] J.D. Joannopoulos, P.R. Villeneuve, and S.H. Fan. Photonic crystals: Putting a new twist on light. *Nature*, 386(6621):143, March 1997.

[3] M. Soljacic, C. Luo, and J.D. Joannopoulos. Nonlinear photonic crystal microdevices for optical integration. *Optics Letters*, 28(8):637–639, 2003.

[4] S. Torquato, S. Hyun, and A. Donev. Multifunctional composites: Optimizing microstructures for simultaneous transport of heat and electricity. *Physical Review Letters*, 89(26):266601, Dec 2002.

[5] A.G. Evans. Lightweight materials and structures. *MRS Bulletin*, October:790, 2001.

[6] M. Deopura. PhD thesis, Massachusetts Institute of Technology, 2005.

[7] M.S. Kushwaha, P. Halevi, L. Dobrzynski, and B. Djafari-Rouhani. Acoustic band structure of periodic elastic composites. *Physical Review Letters*, 71(13):2022–2025, September 1993.

[8] F. Cervera, L. Sanchis, J.V. Sanchez-Perez, R. Martinez-Sala, C. Rubio, and F. Meseguer. Refractive acoustive devices for airborne sound. *Physical Review Letters*, 88(2), 2002.

[9] S. Yang, J.H. Page, Z. Liu, M.L. Cowan, C.T. Chan, and P. Sheng. Focusing of sound in a 3d phononic crystal. *Physical Review Letters*, 93(2):024301–1, July 2004.

[10] A. Akjouj, H. Al-Wahsh, B. Sylla, B. Djafari-Rouhani, and L. Dobrzynski. Stopping and filtering waves in phononic circuits. *J. Phys.-Condes. Matter*, 16(1):37–44, January 2004.

[11] A.A. Krokhin, J. Arriaga, and L.N. Gumen. Speed of sound in periodic elastic composites. *Phys. Rev. Lett.*, 91(26), 2003.

[12] A. Khelif, A. Choujaa, S. Benchabane, B. Djafari-Rouhani, and V. Laude. Guiding and bending of acoustic waves in highly confined phononic crystal waveguides. *Appl. Phys. Lett.*, 84(22):4400–4402, May 2004.

[13] Y. Pennec, B. Djafari-Rouhani, J.O. Vasseur, A. Khelif, and P.A. Deymier. Tunable filtering and demultiplexing in phononic crystals with hollow cylinders. *Phys. Rev. E*, 69(4), April 2004.

[14] H.-U. Nissen. Crystal orientation and plate structure in echinoid skeletal units. *Science*, 166(3909):1150–1152, November 1969.

[15] J.A. Aizenberg, D.A. Muller, J.L. Grazul, and D.R. Hamann. Direct fabrication of large micropatterned single crystals. *Science*, 299(5610):1205–1208, February 2003.

[16] R.J. Park and F.C. Meldrum. Synthesis of single crystals of calcite with complex morphologies. *Adv. Mater.*, 14:1167–1169, 2002.

[17] J.D. Curry. The design of mineralised hard tissue for their mechanical function. *Journal of Experimental Biology*, 202(23):3285–3294, November 1999.

[18] L.G. Griffith and G. Naughton. Tissue engineering - current challenges and expanding opportunities. *Science*, 295(5557):1009–+, February 2002.

[19] A. Sivaraman. *A 3-D perfused Liver on a Chip: High Information Content Assays for Drug Metabolism Studies.* PhD thesis, Massachusetts Institute of Technology, August 2004.

[20] S.Y. Lin, J.G. Fleming, D.L. Hetherington, B.K. Smith, R. Biswas, K.M. Ho, M.M. Sigalas, W. Zubrzycki, S.R. Kurtz, and J. Bur. A three-dimensional photonic crystal operating at infrared wavelengths. *Nature*, 394(6990):251–253, May 1998.

[21] S. Noda, K. Tomoda, N. Yamamoto, and A. Chutinan. Full three-dimensional photonic bandgap crystals at near-infrared wavelengths. *Science*, 289(5479):604–606, July 2000.

[22] B.H. Cumpston, S.P. Ananthavel, S. Barlow, D.L. Dyer, J.E. Ehrlich, L.L. Erskine, A.A. Heikal, S.M. Kuebler, I.Y.S. Lee, D. McCord-Maughon, J.Q. Qin, H. Rockel, M. Rumi, X.L. Wu, S.R. Marder, and J.W. Perry. Two-photon polymerization initiators for three-dimensional optical data storage and microfabrication. *Nature*, 398:51–54, 1999.

[23] S. Kawata, H.B. Sun, T. Tanaka, and K. Takada. Finer features for functional microdevices - Micromachines can be created with higher resolution using two-photon absorption. *Nature*, 412:697–698, 2001.

[24] W.H. Zhou, S.M. Kuebler, K.L. Braun, T.Y. Yu, J.K. Cammack, C.K. Ober, J.W. Perry, and S.R. Marder. An efficient two-photon-generated photoacid applied to positive-tone 3D microfabrication. *Science*, 296:1106–1109, 2002.

[25] M. Deubel, G. Von Freymann, M. Wegener, S. Pereira, K. Busch, and C.M. Soukoulis. Direct laser writing of three-dimensional photonic-crystal templates for telecommunications. *Nature Materials*, 3(7):444–447, July 2004.

[26] E. Sachs, M. Cima, P. Williams, D. Brancazio, and J. Cornie. 3-dimensional printing - rapid tooling and prototypes directly from a cad model. *Journal for Engineering for Industry - Transaction of the ASME*, 114(4):481–488, 1992.

[27] G.M. Gratson, M.J. Xu, and J.A. Lewis. Microperiodic structures - direct writing of three-dimensional webs. *Nature*, 428(6981):386–386, March 2004.

[28] Ashkin A. Acceleration and trapping of particles by radiation pressure. *Physical Review Letters*, 24(4):156, January 1970.

[29] D.M. Schaefer, R. Reifenberger, A. Patil, and R.P. Andres. Fabrication of 2-dimensional arrays of nanometer-size clusters with the atomic-force microscope. *Applied Physics Letters*, 66(8):1012–1014, February 1995.

[30] H. Miyazaki and T. Sato. Mechanical assembly of three-dimensional microstructures from fine particles. *Advanced Robotics*, 11(2):169–185, 1997.

[31] F. Garcia-Santamaria, C. Lopez, F. Meseguer, F. Lopez-Tejeira, J. Sanchez-Dehesa, and H.T. Miyazaki. Opal-like photonic crystal with diamond lattice. *Applied Physics Letters*, 79(15):2309–2311, 2001.

[32] F. Garcia-Santamaria, H.T. Miyazaki, A. Urquia, M. Ibisate, M. Belmonte, N. Shinya, F. Meseguer, and C. Lopez. Nanorobotic manipulation of microspheres for on-chip diamond architectures. *Advanced Materials*, 14(16):1144–1147, August 2002.

[33] K. Aoki, H.T. Miyazaki, H. Hirayama, K. Inoshita, T. Baba, K. Sakoda, N. Shinya, and Y. Aoyagi. Microassembly of semiconductor three-dimensional photonic crystals. *Nature Materials*, 2(2):117–121, 2003.

[34] C.M. Park, J.-S. Yoon, and E.L. Thomas. Enabling nanotechnology with self assembled block copolymer patterns. *Polymer*, 44(22):6725–6760, October 2003.

[35] E.L. Thomas, D.B. Alward, D.J. Kinning, D.C. Martin, D.L. Handlin, and L.J. Fetters. Ordered bicontinuous double-diamond structure of star block copolymers - a new equilibrium microdomain morphology. *Macromolecules*, 19:2197–2202, 1986.

[36] A.M. Urbas, M. Maldovan, P. DeRege, and E.L. Thomas. Bicontinuous cubic block copolymer photonic crystals. *Advanced Materials*, 14:1850–1853, 2002.

[37] P. Alexandridis, U. Olsson, and B. Lindman. A record nine different phases (four cubic, two hexagonal, and one lamellar lyotropic liquid crystalline and two micellar solutions) in a ternary isothermal system of an amphiphilic block copolymer and selective solvents (water and oil). *Langmuir*, 14:2627–2638, 1998.

[38] Y.N. Xia, B. Gates, Y.D. Yin, and Y. Lu. Monodispersed colloidal spheres: old materials with new applications. *Advanced Materials*, 12(10):693–713, May 2000.

[39] A.D. Dinsmore, A.G Yodh, and D.J. Pine. Phase diagrams of nearly hard sphere binary colloids. *Physical Review E*, 52(4):4045–4057, October 1995.

[40] Y.N. Xia, Y.D. Yin, Y. Lu, and J. McLellan. Template-assisted self assembly of spherical colloids into complex and controllable structures. *Advanced Functional Materials*, 13(12):907–918, Dec 2003.

[41] R. Mayoral, J. Requena, J.S. Moya, C. Lopez, A. Cintas, H. Miguez, F. Meseguer, L. Vazquez, M. Holgado, and A. Blanco. 3d long-range ordering in an sio2 submicrometer-sphere sintered superstructure. *Advanced Materials*, 9(3):257, February 1997.

[42] M. Trau, D.A. Saville, and I.A. Aksay. Field-induced layering of colloidal crystals. *Science*, 272(5262):706–709, May 1996.

[43] A. Van-blaaderen, R. Ruel, and P. Wiltzius. Template-directed colloidal crystallization. *Nature*, 385(6614):321–324, January 1997.

[44] Y.A. Vlasov, X. Y. Bo, J.C. Sturm, and D.J. Norris. On-chip naturel assembly of silicon photonic bandgap crystals. *Nature*, 414(6861):289–293, November 2001.

[45] J.J. Cowan and W.D. Slafer. The recording and replication of holographic micropatterns for the ordering of photographic emulsion grains in film systems. *Journal of Imaging Science*, 31:100–107, 1987.

[46] K.I. Petsas, A.B. Coates, and G. Grynberg. Crystallography of optical lattices. *Phys. Rev. A*, 50:5173–5189, 1994.

[47] M. Campbell, D.N. Sharp, M.T. Harrison, R.G. Denning, and A.J. Turberfield. Fabrication of photonic crystals for the visible spectrum by holographic lithography. *Nature*, 404(6773):53–56, March 2000.

[48] Tondiglia V.P., Natarajan L.V., Sutherland R.L., Tomlin D., and Bunning T.J. Holographic formation of electro-optical polymer-liquid crystal photonic crystals. *Advanced Materials*, 14(3):187+, February 2002.

[49] D. Mei, B. Cheng, W. Hu, Z. Li, and D. Zhang. Three dimensional ordered patterns by light interference. *Optics Letters*, 20(429), 1995.

[50] S. Shoji and S. Kawata. Photofabrication of three-dimensional photonic crystals by multibeam laser interference into a photopolymerizable resin. *Appl. Phys. Lett.*, 76:2668–2670, 2000.

[51] S. Yang, M. Megens, J. Aizenberg, P. Wiltzius, P.M. Chaikin, and W.B. Russel. Creating periodic three-dimensional structures by multibeam interference of visible laser. *Chem. Mat.*, 14:2831–+, 2002.

[52] Y.V. Miklyaev, D.C. Meisel, A. Blanco, G. von Freymann, K. Busch, W. Koch, C. Enkrich, M. Deubel, and M. Wegener. Three-dimensional face-centered-cubic photonic crystal templates by laser holography: fabrication, optical characterization, and band-structure calculations. *Appl. Phys. Lett.*, 82:1284–1286, 2003.

[53] I. Divliansky, T.S. Mayer, K.S. Holliday, and V.H. Crespi. Fabrication of three-dimensional polymer photonic crystal structures using single diffraction element interference lithography. *Appl. Phys. Lett.*, 82:1667–1669, 2003.

[54] L.Z. Cai, X.L. Yang, and Y.R. Wang. All fourteen Bravais lattices can be formed by interference of four noncoplanar beams. *Opt. Lett.*, 27:900–902, 2002.

[55] R.L. Sutherland, V.P. Tondiglia, L.V. Natarajan, S. Chandra, D. Tomlin, and T.J. Bunning. Switchable orthorhombic F photonic crystals formed by holographic polymerization-induced phase separation of liquid crystal. *Opt. Express*, 10:1074–1082, 2002.

[56] M.J. Escuti, J. Qi, and G.P. Crawford. Tunable face-centered-cubic photonic crystal formed in holographic polymer dispersed liquid crystals. *Optics Letters*, 28:522–524, 2003.

[57] M.M. Burns, J.M. Fournier, and J.A. Golovchenko. Optical matter - crystallization and binding in intense optical-fields. *Science*, 249(4970):749, August 1990.

[58] X. Wang, C.Y. Ng, W.Y. Tam, C.T. Chan, and P. Sheng. Large-area two-dimensional mesoscale quasi-crystals. *Adv. Mater.*, 15:1526–+, 2003.

[59] R.C. Gauthier and A. Ivanov. Production of quasi-crystal template patterns using a dual beam multiple exposure technique. *Opt. Express*, 12:990–1003, 2004.

[60] C.K. Ullal, M.M. Maldovan, M. Wohlgemuth, E.L. Thomas, C.A. White, and S Yang. Triply periodic bicontinuous structure through interference lithography: A level set approach. *Journal of the Optical Society of America A - Optics Image Science and Vision*, 20(5), 2003.

[61] M. Buerger. *Elementary Crystallography.* MIT Press, MIT, Cambridge, MA, 1978.

[62] A.J. Turberfield. Photonic crystals made by holographic lithography. *MRS Bull.*, 26:632–636, 2001.

[63] Shmueli U., editor. *International Tables for Crystallography*, volume B. Kluwer Academic, Dordrecht, 1996.

[64] D. Sharp, A.J. Turberfield, and R.G. Denning. Holographic photonic crystals with diamond symmetry. *Physical Review - B*, 68(20):205102, November 2003.

[65] O. Toader, T.Y.M. Chan, and S. John. Photonic band gap architectures for holographic lithography. *Phys. Rev. Lett.*, 92, 2004.

[66] M. Wohlgemuth, N. Yufa, J. Hoffman, and E.L. Thomas. Triply periodic bicontinuous cubic microdomain morphologies by symmetries. *Macromolecules*, 34:6083–6089, 2001.

[67] A. Chelnokov, S. Rowson, J.M. Lourtioz, V. Berger, and J.Y. Courtois. An optical drill for the fabrication of photonic crystals. *J. Opt. A-Pure Appl. Opt.*, 1:L3–L6, 1999.

[68] M. Maldovan, C.K. Ullal, W.C. Carter, and E.L. Thomas. Exploring for 3d photonic band gap structures in the 11 fcc space groups. *Nature Materials*, 2(10), 2003.

[69] C.M. Soukoulis, editor. *Photonic Band Gap Materials.* Plenum, New York, 1996.

[70] J.D. Joannopoulos, R.D. Meade, and J.N.Winn. *Photonic Crystals: Molding the Flow of Light.* Princeton University Press, 1995.

[71] H.S. Sozuer, J.W. Haus, and Inguva R. Photonic bands: Convergence problems with the plane-wave method. *Physical Review B*, 45(24), 1992.

[72] K.M. Ho, C.T. Chan, and C.M. Soukoulis. Existence of a photonic gap in periodic dielectric structures. *Physical Review Letters*, 65:3152–3155, 1990.

[73] E. Yablonovitch, T.J. Gmitter, and K.M. Leung. Photonic band-structure - the face-centered-cubic case employing nonspherical atoms. *Physical Review Letters*, 67:2295–2298, 1991.

[74] H.S. Sozuer and J.W. Haus. Photonic bands - simple-cubic lattice. *Journal of the Optical Society of America B - Optical Physics*, 10:296–302, 1993.

[75] R. Biswas, M.M. Sigalas, K.M. Ho, and S.Y. Lin. Three-dimensional photonic band gaps in modified simple cubic lattices. *Physical Review B*, 65(20):205121, May 2002.

[76] O. Toader and S. John. Proposed square spiral microfabrication architecture for large three-dimensional photonic band gap crystals. *Science*, 292:1133–1135, 2001.

[77] C.T. Chan, S. Datta, K.M. Ho, and C.M. Soukoulis. A7 structure - a family of photonic crystals. *Physical Review B*, 50:1988–1991, 1994.

[78] S.H. Fan, P.R. Villeneuve, R.D. Meade, and J.D. Joannopoulos. Design of 3-dimensional photonic crystals at submicron length scales. *Applied Physics Letters*, 65:1466–1468, 1994.

[79] S.G. Johnson and J.D. Joannopoulos. Three-dimensionally periodic dielectric layered structure with omnidirectional photonic band gap. *Applied Physics Letters*, 77:3490–3492, 2000.

[80] M. Maldovan, A.M. Urbas, N. Yufa, W.C. Carter, and E.L. Thomas. Photonic properties of bicontinuous cubic microphases. *Physical Review B*, 65, 2002.

[81] C.T. Chan, K.M. Ho, and C.M. Soukoulis. Photonic band-gaps in experimentally realizable periodic dielectric structure. *EuroPhysics Letters*, 16(6):563–568, 1991.

[82] M. Maldovan and E.L. Thomas. Diamond-structured photonic crystals. *Nature Materials*, 3:593–600, September 2004.

[83] K.M. Ho, C.T. Chan, C.M. Soukoulis, R. Biswas, and M. Sigalas. Photonic band-gaps in 3-dimensions - new layer-by-layer periodic structures. *Solid State Communications*, 89:413–416, 1994.

[84] M. Maldovan, E.L. Thomas, and C.W. Carter. Layer-by-layer diamond-like woodpile structure with a large photonic band gap. *Applied Physics Letters*, 84(3):362–364, January 2004.

[85] C.K. Ullal, M. Maldovan, G. Chen, Y.-J. Han, S. Yang, and E.L. Thomas. Photonic crystals through holographic lithography: Simple cubic, diamond-like, and gyroid-like structures. *Applied Physics Letters*, 84(26):5435, June 2004.

[86] W. Lee, S.A. Pruzinsky, and P.V. Braun. Multiphoton polymerization of waveguide structures within three-dimensional photonic crystals. *Advanced Materials*, 14(4970):271–274, February 2002.

[87] T. Gorishnyy, C.K. Ullal, M. Maldovan, G. Fytas, and E.L. Thomas. Hypersonic phononic crystals. *Physical Review Letters*, Submitted October 2004.

[88] M. Kafesaki, M.M. Sigalas, and E.N. Economou. Elastic wave band-gaps in 3-d periodic polymer matrix composites. *Solid State Communications*, 96(285), 1996.

[89] Z. Liu, X. Zhang, Y. Mao, Y.Y. Zhu, Z. Yang, C.T. Chan, and P. Sheng. Locally resonant sonic materials. *Science*, 289(1734), 2000.

[90] R. Martinez-Sala, J. Sancho, J.V. Sanchez, V. Gomez, and J. Linares. Sound-attenuation by sculpture. *Nature*, 378(6554), 1995.

[91] S. Yang, J.H. Page, Z. Liu, M.L. Cowan, C.T. Chan, and P. Sheng. Ultasound tunelling through 3d phononic crystals. *Physical Review Letters*, 88(104301), 2002.

[92] A.N. Cleland, D.R. Schmidt, and C.S. Yung. Thermal conductance of nanostructured phononic crystals. *Physical Review B*, 64(17):172301, 2001.

[93] A.M Urbas. *Block copolymer photonic crystals.* PhD thesis, Massachusetts Institute of Technology, 2003.

[94] E. Reed, M. Soljacic, and J.D. Joannopoulos. Color of shock waves in photonic crystals. *Physical Review Letters*, 90(20):203904, May 2003.

[95] R.S. Pencui, H. Kriegs, G. Petekidis, G. Fytas, and E.N. Economou. phonons in colloidal systems. *Journal of Chemical Physics*, 118(11):5224 – 5240, march 2003.

[96] A.M Urbas, E.L. Thomas, H. Kriegs, G. Fytas, R.S. Penciu, and E.N. Economou. Acoustic excitations in a self-assembled block copolymer photonic crystal. *Physical Review Letters*, 90(10):108302, 2003.

[97] G. Tommaseo, R.S. Penciu, G. Fytas, E.N. Economou, T. Hashimoto, and N. Hadjichristidis. Phonon propagation in ordered diblock copolymer solutions. *Macromolecules*, 37(5006), 2004.

[98] R. Hartschuh, Y. Ding, J.H. Roh, A. Kisliuk, A.P. Sokolov, C.L. Soles, R.L. Jones, T.J. Hu, W.L. Wu, and A.P. Mahorowala. Brillouin scattering studies of polymeric nanostructures. *Journal of Polymer Science B - Polymer Physics*, 42(6):1106 1113, 2004.

[99] C. Mias, J.P. Webb, and R.L. Ferrari. Finite element modelling of electromagnetic waves in doubly and triply periodic structures. *IEEE Proceedings of Optoelectronics*, 146(2):111–118, 1999.

[100] S. Guenneau and A.B. Movchan. analysis for elastic band structures for oblique incidence. *Archive for Rational Mechanics and Analysis*, 171(1):129–150, January 2004.

[101] L.D. Landau and E.M. Lifshitz. *Electrodynamics of continuous media.* Pergamon Press, New York, 1984.

[102] M.C. Hutley. Optical techniques for the generation of microlens arrays. *Journal of Modern Optics*, 37(2):253–265, 1990.

[103] J.A. Aizenberg, A. Tkachenko, S. Weiner, L. Addadi, and G. Hendler. calcitic microlenses and part of the photoreceptor system in brittlestars. *Nature*, 412(6849):819 – 822, August 2001.

[104] S. Yang, M. Megens, G. Chen, C.K. Ullal, Y.-J. Han, R. Rapaport, E.L. Thomas, and J Aizenberg. Functional biomimetic microlens arrays with integrated pores. *Advanced Materials*, Accepted October 2004.

[105] A.R. Parker. 515 million years of structural colour. *Journal of Optics A - Pure and Applied Optics*, 2(6):R15–R28, 2000.

[106] A.R. Parker, V.L. Welch, D. Driver, and N. Martini. structural colour - opal analogue discovered in a weevil. *Nature*, 426(6968):786–787, 2003.

[107] M.F. Land and D.-E. Nilsson. *Animal Eyes.* Oxford University Press, New York, 2002.

[108] V. Sundar, A.D. Yablon, J.L. Grazul, M. Ilan, and J.A. Aizenberg. Fibre-optical features of a glass sponge - some superior technologicla secrets have come to light from a deep-sea organism. *Nature*, 424(899), 2003.

[109] P. Vukusic, J.R. Sambles, and C.R. Lawrence. Structural colour - colour mixing in wing scales of a butterfly. *Nature*, 404(6777):457, 2000.

[110] P. Vukusic, R.J. Wootton, and J.R. Sambles. Remarkable iridescence in the hindwings of the damselfly neurobasis chinensis chinensis (linnaeus) (zygoptera : Calopterygidae). *Proceedings of the Royal Society of London Series B - Bio. Sci.*, 271(1539):595–601, March 2004.

[111] G. Hendler and M. Byrne. Fine-structure of the dorsal arm plate of ophiocoma-wendti - evidence for a photoreceptor system (echinodermata, ophiuroidea). *Zoomorphology*, 107(5):261–272, 1987.

[112] S. Biehl, R. Danzebrink, P. Oliviera, and M.A. Aegerter. refractive microlens fabrication by ink-jet process. *Journal of Sol-Gel Science and Technology*, 13(1-3):177–182, 1998.

[113] S. Haselbeck, H. Schreiber, Schwider, and N. Streibl. Microlenses fabricated by melting a photoresist on a base layer. *Optical Engineering*, 32(6):1322–1324, 1993.

[114] P. Savander. Microlens arrays etched into glass and silicon. *Optics and Lasers in Engineering*, 20(2):97–107, 1994.

[115] M.H. Wu, C. Park, and G.M. Whitesides. Fabrication of arrays of microlenses with controlled profiles using gray-scale microlens projection photolithography. *Langmuir*, 18(24):9312–9318, November 2002.

[116] Y. Lu, Y.D. Yin, and Y.N. Xia. A self-assembly approach to the fabrication of patterned, two-dimensional arrays of microlenses of organic polymers. *Advanced Materials*, 13(1):34, January 2001.

[117] X.Y. Ao and S.L. He. Three-dimensional photonic crystal of negative refraction achieved by interference lithography. *Optics Letters*, 29(21):2542–2544, November 2004.

[118] M.P. MacDonald, G.C. Spalding, and K. Dholakia. Microfluidic sorting in an optical lattice. *Nature*, 426:421–424, 2003.

[119] S. Jeon, J.U. Park, R. Cirelli, S. Yang, C.E. Heitzman, P.V. Braun, P.J.A. Kenis, and J.A. Rogers. Fabricating complex three-dimensional nanostructures with high-resolution conformable phase masks. *Proceedings of the National Academy of Sciences of the United States of America*, 101(34):12428–12433, 2004.